

## Versatile shaping of optical frequency combs and applications

Présentée le 25 janvier 2021

Faculté des sciences et techniques de l'ingénieur  
Laboratoire de systèmes photoniques  
Programme doctoral en photonique

pour l'obtention du grade de Docteur ès Sciences

par

**Jianqi HU**

Acceptée sur proposition du jury

Prof. C. Moser, président du jury  
Prof. C. S. Brès, directrice de thèse  
Prof. J. Azana, rapporteur  
Prof. C.-B. Huang, rapporteur  
Prof. T. J. Kippenberg, rapporteur



To my family.

# Acknowledgements

First and foremost, I would like to express my deepest gratitude to my thesis supervisor, Prof. Camille-Sophie Brès. Four years ago, she encouraged me to pursue a direct PhD at EPFL. Since then, she always gave me great freedom to explore various fields of photonics, while being supportive along the way. Her superior guidance and full trust really have made my PhD an enjoyable journey.

Then I would like to thank Prof. Chen-Bin (Robin) Huang for hosting my visit at National Tsing Hua University. He unselfishly shared with me his expertise in shaping of light pulse and orbital angular momentum, which greatly extended my research scope.

My sincere thank goes to Prof. Tobias J. Kippenberg for providing the wonderful collaboration opportunity. I thank the K-lab comb team, especially Dr. Jijun He for the help in the experiments and Dr. Junqiu Liu for fabricating the samples. The results we got are fruitful.

I am deeply grateful to the jury president Prof. Christophe Moser, and jury members Prof. José Azaña, Prof. Chen-Bin Huang, and Prof. Tobias J. Kippenberg for reviewing and commenting my thesis work.

I appreciate spending the past four years with all of the colleagues at PHOSL, both inside and outside the lab (listed in order of appearance to me): Dr. Simon Fabbri, Dr. Sida Xing, Dr. Svyatoslav Kharitonov, Dr. Davide Grassani, Dr. Adrien Billat, Dr. Can Yao, Ivan Cardea, Eirini Tagkoudi, Dr. Edgars Nitiss, Dr. Florent Mazeas, Arman Ayan, Ozan Yakar, Boris Zabelich, Dr. Ezgi Sahin, Moritz Bartnick. Especially, I would like to thank Simon for the guidance and help at the beginning of my PhD, Sida for both scientific and daily life conversations, and Edgars for the collaboration on the optical poling of the silicon nitride microresonators. I am also indebted to Françoise Behn, the lab secretary, for preparing the paper works.

Lastly, I owe my parents Xing Hu and Xiangyun Zhu for their unconditional love and support.

*Lausanne, Oct. 22, 2020*

*Jianqi Hu*





# Abstract

Optical frequency combs are a series of phase-locked and equidistant laser lines in the spectral domain. In the time domain, they correspond to periodic pulse trains by the Fourier relation. The ability to shape optical combs and pulse trains is pivotal to many applications in optical communications and microwave photonics. For communication purposes, the information can be multiplexed in either time or frequency, by associating the data symbols to the comb lines or optical pulses. In particular, shaping optical pulses into sinc profile is of special interest, as it achieves high spectral efficiency when multiplexed. In regards to microwave photonics, frequency combs also have emerged as useful tools for processing radiofrequency (RF) signals in parallel. Comb-based RF photonic filter is one of the examples. Optical combs combined with dispersive propagation could construct filtering functions in the RF domain. Additionally, the shaping of comb spectra enables reconfiguration of the synthesized RF photonic filters.

The thesis presents results on various shaping techniques for the generation and applications of optical frequency combs. Both electro-optic combs and integrated microcombs are explored in the study, while their pulse shaping takes place either in the generation stage or externally. The first part of the thesis deals with optical sinc pulse shaping. A simple and flexible sinc pulse generator is demonstrated based on a single electro-optic modulator. Rectangular spectra of optical sinc pulses are harnessed to shape RF filters with sinc responses. Moreover, the method of sinc pulse shaping can fulfill the add-drop functionalities for superchannels multiplexed from sinc pulses.

In the second part, temporal Talbot shaping of frequency combs is addressed. The temporal Talbot effect multiplies the repetition-rates of optical pulse trains in time. A novel temporal Talbot multiplier is demonstrated in a conventional optical tapped delay line structure. Furthermore, such shaping concept is extended for the demonstration of azimuthal Talbot effect. When the orbital angular momentum modes are superimposed with Talbot phases, the light petal is self-imaged in the azimuthal angle.

Lastly, the third part exploits the internal shaping of soliton microcombs for the use in RF photonic filters. Versatile soliton states and thereby various microcomb spectra, are generated in a microresonator on demand. Such optical spectra could reconfigure their corresponding RF filters. Among others, perfect soliton crystals and two-soliton states are utilized, which

## Abstract

---

respectively divide and translate their filter passband frequencies.

Key words:

- Optical frequency comb
- Optical orbital angular momentum
- Optical sinc pulse
- Soliton microcomb
- Talbot effect
- RF photonic filter

# Résumé

Un peigne de fréquences optiques est une série de modes optiques régulièrement espacés en fréquence et cohérents en phase entre eux. Par transformée de Fourier, dans le domaine temporel cela correspond à des trains d'impulsions successives et régulières. La possibilité de pouvoir contrôler la forme spectrale du peigne optique et les impulsions correspondantes est essentielle pour de nombreuses applications de télécommunications optiques et de photonique appliquée aux micro-ondes. Dans le cas des télécommunications, les données peuvent être multiplexées indifféremment dans le domaine temporel ou fréquentiel en attribuant un canal de données à une série d'impulsions ou à un mode du peigne optique. Un cas spécial, avec des impulsions optiques façonnées pour s'approcher de la fonction sinus cardinal, est particulièrement intéressant car il permet d'obtenir une efficacité spectrale élevée quand plusieurs canaux optiques sont multiplexés ensemble. Pour la photonique appliquée aux micro-ondes, les peignes optiques sont apparus comme des outils indispensables afin de traiter plusieurs signaux micro-ondes en parallèle. Les filtres photoniques pour ondes radiofréquences basé sur un peigne optique en sont un exemple. Un signal radiofréquence peut être filtré par une astucieuse association d'un peigne optique avec un milieu dispersif. De plus, le control de la forme spectrale du peigne optique permet la reconfiguration du filtre micro-onde.

La présente thèse rapporte les résultats du développement de plusieurs techniques de génération de peigne de fréquences optiques ainsi que les résultats de multiples expériences résultant de leurs utilisations. Des peignes optiques ont ainsi été généré avec des modulateurs électro-optiques ainsi qu'en utilisant des micro-résonateurs optiques, avec le contrôle des impulsions optiques durant la génération des modes ou a posteriori.

La première partie la thèse présente la génération d'un train d'impulsion optique approchant la forme de la fonction sinus cardinal. Une source minimaliste et flexible n'utilisant qu'un seul modulateur électro-optique est décrite. Grâce à une forme spectral rectangulaire du peigne optique, un filtre radiofréquence ayant la forme du sinus cardinal a été obtenu. De plus, le control précis des impulsions optiques permet une fonction d'ajout/retrait pour des supercanaux de télécommunications optiques basés sur le multiplexage de trains d'impulsions.

Dans seconde partie le contrôle du peigne optique par effet Talbot est étudié. L'effet Talbot temporel peut démultiplier le taux de répétition des trains d'impulsions optiques. Un multipli-

## Résumé

---

cateur temporel utilisant l'effet Talbot est démontré en utilisant seulement une matrice  $1 \times N$ , avec différents retards et avec des contrôles de phase indépendants, suivi d'un recombinaison. De plus, le concept est étendu avec la démonstration de l'effet Talbot azimutal. En effet, quand les modes de moment angulaire orbital sont surimposés en suivant les phases Talbotiennes, les pétales lumineux sont distribués suivant l'angle azimutal.

La troisième partie rapporte comment le contrôle de solitons générés dans des micro-résonateurs photoniques permet l'utilisation de ces sources de peignes optiques pour obtenir des filtres radiofréquences. Plusieurs états solitoniques étant atteignables dans le micro-résonateur, une source de peigne optique polyvalente est démontrée. Ainsi, des filtres radiofréquences reconfigurables peuvent être obtenus. En particulier, des cristaux parfaits de solitons et des états à double solitons ont été utilisés pour démontrer des scissions du filtre passe-bande ainsi que des translations en fréquence.

Mots clefs :

- Peigne de fréquences optiques
- Impulsion optique sinus cardinal
- Effet Talbot
- Moment angulaire orbital optique
- Micropeigne à solitons
- Filtre photonique radiofréquence

# Contents

<b>Acknowledgements</b>	<b>i</b>
<b>Abstract (English/Français)</b>	<b>iii</b>
<b>List of figures</b>	<b>ix</b>
<b>List of tables</b>	<b>xix</b>
<b>Acronyms</b>	<b>xxi</b>
<b>1 Introduction</b>	<b>1</b>
1.1 Overview of optical frequency combs . . . . .	1
1.2 Thesis motivation . . . . .	4
1.3 Thesis goal and contribution . . . . .	5
1.4 Thesis structure . . . . .	7
<b>2 General principles</b>	<b>9</b>
2.1 Electro-optic modulator . . . . .	9
2.2 Spatial light modulator . . . . .	14
2.3 The Talbot effect . . . . .	18
2.4 Optical microresonator . . . . .	21
2.5 Conclusions . . . . .	27
<b>3 Generation and applications of optical sinc pulses</b>	<b>29</b>
3.1 Introduction . . . . .	29
3.2 Properties of sinc pulses . . . . .	30
3.3 Flexible optical sinc pulse generator . . . . .	33
3.4 RF photonic filters of sinc responses . . . . .	37
3.5 Add-drop multiplexer for Nyquist OTDM system . . . . .	41
3.6 Conclusions . . . . .	48
<b>4 Temporal and azimuthal Talbot effects</b>	<b>49</b>
4.1 Introduction . . . . .	49
4.2 Properties of Talbot phases . . . . .	50
4.3 Temporal Talbot multiplier based on an optical tapped delay line . . . . .	53

## Contents

---

4.4	Azimuthal Talbot effect based on orbital angular momentum beams . . . . .	60
4.5	Conclusions . . . . .	68
<b>5</b>	<b>Soliton microcomb based RF photonic filters</b>	<b>69</b>
5.1	Introduction . . . . .	69
5.2	Principle of operation . . . . .	70
5.3	Versatile soliton microcomb generation . . . . .	75
5.4	Reconfigurable soliton-based RF filter . . . . .	78
5.5	Performance of soliton-based RF filter . . . . .	85
5.6	Conclusions . . . . .	88
<b>6</b>	<b>Conclusions and perspectives</b>	<b>89</b>
	<b>Bibliography</b>	<b>102</b>
	<b>Curriculum Vitae</b>	<b>103</b>

# List of Figures

1.1	Time and frequency representations of optical frequency combs. In the time domain, frequency combs correspond to periodic optical pulse trains with period $T = 1/f_{\text{rep}}$ . $\Delta\phi$ is the carrier-envelope phase offset. In the frequency domain, combs are a series of discrete laser lines equally spaced by the comb repetition-rate $f_{\text{rep}}$ . The absolute frequency of $n$ -th comb line is given by $f_n = nf_{\text{rep}} + f_0$ , where $f_0$ is the carrier-envelope offset frequency that relates to $\Delta\phi$ as $2\pi f_0 = \Delta\phi f_{\text{rep}}$ . Adapted from [6]. . . . .	2
2.1	Schematics of various types of Electro-optical modulators (EOMs). (a) PM (phase modulator); (b) MZM (Mach-Zehnder modulator); (c) DP-MZM (dual-parallel Mach-Zehnder modulator). The black rectangle represents the electro-optic modulation region, where RF and DC signals are applied. . . . .	10
2.2	Examples of the waveforms and spectra based on EOMs driven by a single RF frequency. (a) PM; (b) MZM; (c) DP-MZM. The operation parameters of the DP-MZM are retrieved from [89]. $T = 2\pi/\omega_m$ is the repetition period, the mode indices are indexed with respect to the optical carrier, and the phases of central comb modes are labeled. MZM and DP-MZM can generate sinc pulses with 3 and 5 comb lines, but not PM. . . . .	11
2.3	Simulation of the complex amplitude modulation through double-phase hologram (DPH) encoding. (a) Schematic of the complementary checkerboards (gray: modulated, black: unmodulated). The SLM is divided into two checkerboards for the modulation of the two holograms separately. (b) Simulation verification of the DPH encoding scheme. Retrieved amplitude and phase images are in good agreement with the target amplitude and phase images. (c) The phase hologram encoded to the SLM. (d) Normalized power of the Fourier transform of the complex field. Red circle indicates the low-pass filter. . . . .	15
2.4	Schematic setups of Fourier domain pulse shaping. (a) Classical $4 - f$ pulse shaper with gratings at the input and output planes, and spatial light modulator at the Fourier plane. Adapted from [106]. (b) Reflective-type pulse shaper with folded $4 - f$ configuration. LCoS: liquid crystal on silicon. Adapted from Finisar Waveshaper product brochure. . . . .	17



## List of figures

---

2.5	Illustration of spatial Talbot effect. When a plane wave illuminates a periodic grating, the transmitted optical field is diffracted, and repetitively resembles itself along the propagation. The interference pattern is also known as the Talbot carpet. $z_T$ is the Talbot length between the grating plane and the secondary Talbot image. Adapted from [107]. . . . .	18
2.6	Illustrations of temporal and spectral Talbot effects. (a) Temporal self-imaging is achieved by second-order chromatic dispersion of optical frequency combs. (b) Spectral self-imaging is achieved by quadratic phase modulation of optical pulses. $t_r$ is the pulse period, $\nu_r$ is the comb FSR, and $q = 3$ is shown. The phases of optical pulses after temporal self-imaging, and the phases of frequency combs after spectral self-imaging, comply with the generalized Talbot relation. Adapted from [111]. . . . .	19
2.7	Layout of the optical microresonator. The light is coupled from the bus waveguide to the ring resonator and collected at the bus waveguide. $i\sqrt{\theta_{ex}}$ : cross coupling coefficient; $L_R$ : roundtrip length; $\alpha$ : loss per unit length; $\phi_R$ : phase accumulated per roundtrip. . . . .	21
2.8	Amplitude and phase responses of optical microresonator under three different regimes. Under-coupled regime: $\theta_{ex} = 0.1$ (blue) ; critical-coupled regime: $\theta_{ex} = 0.19$ (orange); over-coupled regime: $\theta_{ex} = 0.3$ (yellow). The intrinsic loss term is $\exp(-\alpha L/2) = 0.9$ for all cases. For critical- (under-, over-) coupling, the cross coupling $\theta_{ex}$ is equal (smaller, larger) than the loss per roundtrip $1 - \exp(-\alpha L)$ , or equivalently $\kappa_0 = (>, <)\kappa_{ex}$ . . . . .	22
2.9	Examples of microcomb generation in the anomalous and normal dispersion regimes. The insets show the temporal waveforms of the microcombs. (a) Dissipative Kerr soliton generation in anomalous dispersion regime, with solitons seated at the CW background. (b) Dark pulse generation in anomalous dispersion regime, with dark pulses formed in the time domain. Adapted from [16] with (a) originally from [124] and (b) originally from [134]. . . . .	26
3.1	Frequency and time representations of periodic sinc pulses. (a) In the frequency domain, sinc pulses correspond to a series of equal amplitudes, linear phases frequency comb lines. $\Delta f$ : comb FSR; $N$ : number of comb lines. (b) In the time domain, the intensity of sinc pulses is shown. $T$ : pulse period; $T_s$ : the symbol period, or equivalently half of the zero-crossings between the main peak. Adapted from [65]. . . . .	32
3.2	Schematic setup of flexible sinc pulse generator. A CW laser is injected to the MZM driven by a number of synchronized RF sinusoidal waves. OSO: optical sampling oscilloscope; OSA: optical spectrum analyzer; $\varphi$ : tunable phase shifter; Amp: electrical amplifier. The MZM output is directed to the OSO and OSA for measurement, where the intensity waveform and spectrum of sinc pulses with 9 comb lines are shown. . . . .	34

3.3	Waveforms and spectra of optical sinc pulses. (a) Optical sinc pulses with 5, 7, and 9 comb lines when the MZM is driven by 10, 20, 30, 40 GHz. (b) Optical sinc pulses with 4, 6, and 8 comb lines when the MZM is driven by 5, 15, 25, 35 GHz. Blue: experiment; Orange: simulation. . . . .	35
3.4	Optical sinc pulses of 9 comb lines under different RF power levels. (a) The measured pulse widths of sinc pulses (blue) and SMSR of the comb spectra (orange) versus the RF power input to the MZM. Blue dashed line corresponds to the ideal FWHM of sinc pulse with 9 comb lines. (b) The temporal waveform of the sinc pulses under 4.2 dBm (top) and 11.9 dBm (bottom), respectively. Blue: experiment; Orange: simulation. . . . .	36
3.5	Experimental setup of sinc-shaped RF filters based on rectangular optical combs. EDFA: erbium-doped fiber amplifier; PC: polarization controller; DCF: dispersion compensating fiber; PD: photodetector; OSA: optical spectrum analyzer; VNA: vector network analyzer. The rectangular optical combs are generated using two MZMs driven by two RF frequencies $f_1$ and $f_2$ separately. The RF signal from the VNA is upconverted to the optical domain in a DP-MZM via the electrical $90^\circ$ hybrid. Then the frequency comb lines carrying the information of the RF signals acquire differential delays through propagation in a spool of DCF. After being detected by the PD, the RF signal is retrieved and send back to the VNA for the filter response measurement. The images of OSA and VNA show the target rectangular optical comb spectrum and sinc-shaped RF response, respectively. . . . .	38
3.6	RF photonic filters with sinc responses based on optical combs with rectangular shapes. (a) Optical rectangular combs generated based on cascaded MZMs with 6, 9, 12 spectral lines at 20GHz comb FSRs. (b) Corresponding sinc-shaped RF photonic filters based on rectangular combs in (a). The 3 dB bandwidth of the RF filters are indicated. Blue: experiment; Orange: simulation (ideal sinc). . . .	40
3.7	Phase response of the RF photonic filter based on the rectangular combs with 9 spectral lines. Blue: measured phase response; Orange: unwrapped phase response; Yellow: simulated phase response; Purple: measured power response. The RF filter shows $\pi$ phase jumps at the nulls of the sinc function. . . . .	41
3.8	Layout of $2 \times 2$ MZM with the flow of optical fields. As an example, the optical modulation function is calculated when a unit optical field is injected to the input port 1 of the $2 \times 2$ MZM. The modulation function for the bar coupling and cross coupling are respectively $i \sin \theta$ and $i \cos \theta$ , where $\theta$ denotes the total phase shift per arm. . . . .	42

- 3.9 Bar and cross pulse carvers in comparison with ideal bright and dark sinc functions. The  $2 \times 2$  MZM is driven by two RF frequencies at 10 GHz and 20 GHz. (a) When the RF modulation is weak, the bar function is close to the ideal sinc shape and its rectangular spectrum shows high SMSR. However, the cross function could not achieve the complete notch in time. The simulation is obtained by  $\psi = 0.152$ ,  $\beta_1 = 0.3$ , and  $\beta_2 = 0.3$ . (b) When the RF modulation is large, the bar function deviates from the ideal sinc shape and its rectangular spectrum shows poor SMSR. The cross function does achieve almost complete notch in time, and shows nearly no loss at the other ISI points. The simulation is obtained by  $\psi = 0.323$ ,  $\beta_1 = 0.635$ , and  $\beta_2 = 0.605$ . . . . . 43
- 3.10 Schematic diagrams of add-drop multiplexers based on  $2 \times 2$  MZM operated as simultaneous bright and dark sinc carvers. (a) The original multiplexed Nyquist OTDM channels (ch1, ..., ch5) and the new channel ch3' are directed to the two input ports of the  $2 \times 2$  MZM. One of the output of the MZM after temporal gating corresponds to the dropped ch3. The other port directly outputs the Nyquist OTDM signals with ch3 being replaced by the new ch3'. (b) Only the original multiplexed Nyquist OTDM channels are injected to the MZM. The two outputs of MZM correspond to the dropped ch3 and the Nyquist OTDM signals with ch3 being notched, respectively. The new channel ch3' is then combined with the notched Nyquist OTDM signals in an optical coupler, thereby forming the new Nyquist OTDM signals with ch3' instead of ch3. . . . . 44
- 3.11 Simulation setups for the assessment of Nyquist OTDM ADMs. (a) Nyquist OTDM transmitter consists of 5 streams of time-multiplexed 10 Gb/s modulated sinc pulse trains. (b) The proposed ADM based on both input ports of the  $2 \times 2$  MZM as well as its detection setup. (c) The proposed ADM based on only one input port of the  $2 \times 2$  MZM as well as its detection setup. (i)-(vi) are eye diagrams at different locations specified in the setups (a)-(c). (i) original Nyquist OTDM signals; (ii) dropped signal ch3 in (b); (iii) new Nyquist OTDM signals with ch3' replacing ch3 in (b); (iv) dropped signal ch3 in (c); (v) notched Nyquist OTDM signals (without ch3); (vi) new Nyquist OTDM signals with ch3' replacing ch3 in (c). . . . . 46
- 3.12 BER performances of proposed ADMs based on  $2 \times 2$  MZM. (a) BER curves of add, drop, and other subchannels when the ADM uses both of the input ports of  $2 \times 2$  MZM. (b) BER curves of add, drop, and other subchannels when the ADM uses only one of the input ports of  $2 \times 2$  MZM. FEC: 7% hard-decision forward error correction FEC threshold ( $\text{BER} = 3.8 \times 10^{-3}$ ); Ideal: back-to-back matched sampling. . . . . 47

4.1	The Talbot carpet. $p/q = 1/4$ and $1/2$ are indicated with the solid boxes, while $1/3$ and $2/3$ are indicated with the dashed boxes. It can be seen that 3-times self-images at $1/3$ shows a period shift compared to the initial images, while not for $1/4$ , $1/2$ , and $2/3$ . This may account for the definition of Talbot phases in [118]. Adapted from [58]. . . . .	51
4.2	Schematic diagram of the optical tapped delay line (TDL) structure. It is composed of $N$ parallel arms with incremental delays and phase tuning elements. $T_0$ is the unit delay time, and $\varphi_n$ ( $n = 0, 1, 2, \dots, N-1$ ) are the phases applied to phase shifters. . . . .	54
4.3	Spectral amplitude filtering operation of the TDL structure for $N$ -times repetition-rate multiplication (RRM). The phase tuning elements of the TDL are configured all in-phase, i.e. $(0, 0, 0, 0, 0, 0, 0, 0)$ . (a) Power (top) and phase (bottom) response of the TDL structure. (b) Optical spectra (top) and temporal waveforms (bottom) at the input and output the TDL filter. In simulation, $N = 8$ is used and the FWHM of the input pulse is set to $1/25$ of its period. $f_{FSR} = 1/T_0$ is the free spectral range of the device. . . . .	55
4.4	Spectral phase-only filtering (temporal Talbot) operation of the TDL structure for $N$ -times RRM. The phase tuning elements of the TDL are configured with Talbot phases of $N = 8$ , i.e. $(0, \pi/8, \pi/2, 9\pi/8, 0, 9\pi/8, \pi/2, \pi/8)$ . (a) Power (top) and phase (bottom) response of the TDL structure. (b) Optical spectra (top) and temporal waveforms (bottom) at the input and output the TDL filter. . . . .	56
4.5	Combined amplitude and phase filtering operation of the TDL structure for $N$ -times RRM. (a) Power (top) and phase (bottom) response of the TDL and the spectrum (top) and temporal waveform (bottom) at the output of TDL filter, when the phase tuning elements of the TDL are configured with repeated Talbot phases of $N = 4$ , i.e. $(0, \pi/4, \pi, \pi/4, 0, \pi/4, \pi, \pi/4)$ . 8-times RRM is achieved by 2-times spectral amplitude filtering and 4-times Talbot effect. (b) Power (top) and phase (bottom) response of the TDL and the spectrum (top) and temporal waveform (bottom) at the output of TDL filter, when the phase tuning elements of the TDL are configured with Talbot phases of $N = 2$ . 8-times RRM is achieved by 4-times spectral amplitude filtering and 2-times Talbot effect. . . . .	57
4.6	Proof-of-concept verification of the proposed structure ( $N = 2$ ) using a delay line interferometer (DLI). (a) Experimental setup. MZM: Mach-Zehnder modulator; EDFA: erbium-doped fiber amplifier; OSA: optical spectrum analyzer; OSO: optical sampling oscilloscope. Input pulse trains with 5 GHz repetition-rate and 21 comb lines are synthesized based on cascade modulators. The spectra and waveforms of the output pulse trains from the DLI are measured with OSA and OSO. (b) The principle of temporal Talbot operation based on DLI. The orange dashed lines corresponds to the DLI's transfer function, where the blue circles show equal transmission meanwhile periodic $(0, \pi/2)$ phase response. (c) Optical spectra (top) and temporal waveforms (bottom) measured at the input and two output ports of the DLI. . . . .	58

## List of figures

---

- 4.7 Schematics of orbital angular momentum (OAM) modes of light. Helical phase fronts (top) and phase profiles at the cross-sections (bottom) of OAM modes are shown, with topological charges from  $l = -2$  to  $2$ . Note that  $l = 0$  corresponds to the plane wave of a Gaussian beam. The phase fronts are adapted from Wikipedia. . . . . 61
- 4.8 Concept of azimuthal Talbot effect. When the OAM modes are superimposed with Talbot phases, intensity self-images occur in the azimuthal angle. The last column shows the intensity profile corresponding to the summation of all the OAM modes in each row (topological charges from  $-10$  to  $10$  are used in the simulation while only  $-2$  to  $2$  are shown). Ordinary (Ord.) and inverted (Inv.) with integer ( $\times 1$ ) and fractional ( $\times 2$  and  $\times 3$ ) Talbot effects are illustrated. . . . 62
- 4.9 Experimental setup for the demonstration of azimuthal Talbot effect. ATT: attenuator; PC: polarization controller; COL: collimator; SLM: spatial light modulator; L: lens; CAM: camera;  $f$ : focal length. The setup consists of an optical  $4 - f$  system to encode superposition of OAM modes, with a SLM in its input plane, an iris in its Fourier plane, and a camera in its output plane. The SLM is loaded with target phase pattern (the image corresponds to the 2-times azimuthal Talbot effect), and is illuminated by a collimated laser beam. . . . . 63
- 4.10 Experiment and simulation images of azimuthal Talbot effect. The OAM modes used in the experiment and simulation are ordered from  $-10$  to  $10$  of equal amplitudes. Ordinary (a) integer Talbot ( $\times 1$ ): OAM modes all in-phase; (b) fractional Talbot ( $\times 2$ ): OAM modes with periodic  $(0, \pi/2)$  phases; (c) fractional Talbot ( $\times 3$ ): OAM modes with periodic  $(0, 2\pi/3, 2\pi/3)$  phases. Inverted (d) integer Talbot ( $\times 1$ ): OAM modes with periodic  $(0, \pi)$  phases; (e) fractional Talbot ( $\times 2$ ): OAM modes with periodic  $(0, 3\pi/2)$  phases; (f) fractional Talbot ( $\times 3$ ): OAM modes with periodic  $(0, 5\pi/3, 2\pi/3, \pi, 2\pi/3, 5\pi/3)$  phases. . . . . 64
- 4.11 Extracted azimuthal intensity profiles of inverted Talbot images. From top to bottom: original (integer Talbot), 2-times azimuthal Talbot, and 2-times azimuthal Talbot. Orange: experiment; dashed black: simulation. . . . . 65
- 4.12 Experiment and simulation images of azimuthal Talbot effect with Gaussian-apodized OAM spectrum. OAM modes ordered from  $-10$  to  $10$  with Gaussian apodization for (a) integer Talbot ( $\times 1$ ) (b) fractional Talbot ( $\times 2$ ) (c) fractional Talbot ( $\times 3$ ) in the azimuthal angle. OAM modes ordered from  $-10$  to  $10$  with Gaussian apodization for (d) fractional Talbot ( $\times 10$ ) (e) fractional Talbot ( $\times 11$ ) (f) fractional Talbot ( $\times 12$ ) in the azimuthal angle. . . . . 66
- 4.13 Experiment and simulation images of azimuthal Talbot effect of Laguerre-Gaussian (LG) modes. LG modes with radial index of  $0$  and azimuthal indices ordered from  $-10$  to  $10$  for (a) integer Talbot ( $\times 1$ ) (b) fractional Talbot ( $\times 2$ ) (c) fractional Talbot ( $\times 3$ ) in the azimuthal angle. LG modes with radial index of  $1$  and azimuthal indices ordered from  $-10$  to  $10$  for (d) integer Talbot ( $\times 1$ ) (e) fractional Talbot ( $\times 2$ ) (f) fractional Talbot ( $\times 3$ ) in the azimuthal angle. . . . . 67

- 5.1 Schematic diagram of versatile soliton-based RF photonic filters. The conceptual setup consists of four parts: microcomb generation, RF signal upconversion, dispersive propagation, and photodetection. MZM: Mach-Zehnder modulator; SMF: single-mode fiber; PD: photodiode; VNA: vector network analyzer. Reconfigurable RF filters are synthesized based on versatile soliton microcombs. (a) Single-soliton RF filter with passband centered at  $f_{\text{FSR}}$  (blue). (b)  $N$ - perfect soliton crystals (PSC) RF filters with passband centered at  $f_{\text{FSR}}/N$  (green,  $N = 4$  is shown); (c) Two-soliton microcomb (TSM) RF filters with passband centered at  $f_{\text{FSR}}\alpha/360^\circ$  (orange), where  $\alpha$  is the relative azimuthal angle between two solitons ( $\alpha = 90^\circ$  is shown). . . . . 71
- 5.2 Visualization of RF filter response using different microcomb FSR. Simulated RF filter responses (solid lines) based on various microcomb FSRs  $\Delta f$  from 10 GHz, 20 GHz, 50 GHz to 104 GHz (FSR used in this study) are shown. The dispersion-induced fading envelopes (dashed lines) are also sketched. Soliton pulse width  $T_s = 100$  fs is considered for all the cases in the simulation, while the accumulated dispersion  $\Theta_2$  is adapted so that all these RF filters coincide at the same frequency. . . . . 74
- 5.3  $\text{Si}_3\text{N}_4$  microresonator characterization. (a) Optical image of the  $\text{Si}_3\text{N}_4$  microresonator chips. (b) Total linewidth, coupling strength, and intrinsic linewidth of each resonance in the  $\text{TE}_{00}$  mode family. The shaded area corresponds to the resonances pumped in the experiment. (c) Top: measured integrated group velocity dispersion (GVD) ( $D_{\text{int}}/2\pi$ ) of the  $\text{TE}_{00}$  mode family with respect to the resonance of 1555.1 nm; Bottom: zoom-in of integrated GVD region between 1540 nm and 1580 nm. Dominant avoided mode crossing (AMX) is observed around wavelength region of 1565 nm. . . . . 75
- 5.4 Excitation of versatile soliton states. (a) Simulated stability diagram for versatile soliton microcomb generation. Four different stability regions are listed: modulation instability (MI, blue), breathers (red), spatio-temporal and transient chaos (chaos, yellow), and stable dissipative Kerr soliton (DKS, green). Excitation routes for (1) single-soliton, (2) PSC, and (3) TSM generation are depicted. (b) Examples of experimentally generated spectra at resonance of 1555.1 nm: (1) single-soliton, (2) PSC ( $N = 4$ ), and (3) TSM ( $\alpha = 132.7^\circ$ ). The pump power is also indicated for each microcomb generation. (c) Typical soliton steps for PSC and TSM formations, which are respectively denoted by the shaded areas. Transmission curves are obtained by scanning a laser across the resonance below (left) and above (right) the threshold pump power, at resonance of 1555.1 nm. . . . 77

- 5.5 Single-soliton/PSC spectra and their corresponding RF photonic filters. Through deterministic accessing PSC states of different resonances, the RF filter pass-bands can be divided correspondingly. Left column: microcomb spectra (blue: experiment, red:  $\text{sech}^2$  fitting). The insets of left column illustrate soliton distribution inside the microresonator: single-soliton and PSCs with adjacent soliton angles of  $180^\circ$ ,  $120^\circ$ , and  $90^\circ$ , respectively ( $360^\circ/N$ ,  $N = 2, 3, 4$ ). Right column: corresponding normalized RF filter responses (blue: experiment, red: simulation). From top to bottom: RF filters centered at 16.24 GHz, 8.12 GHz, 5.42 GHz, and 4.06 GHz based on single-soliton and  $N$ -PSC ( $N = 2, 3, 4$ ), generated at resonances of 1556.0 nm, 1556.0 nm, 1554.3 nm, 1555.1 nm, respectively. . . . 78
- 5.6 TSM spectra and their corresponding RF photonic filters. By accessing different two-soliton states, the RF filters can be all-optically reconfigured. Left column: TSM spectra obtained from the resonance of 1556.0 nm (blue: experiment, red: envelope fitting). The insets illustrate two soliton distribution inside the microresonator: the angles between them are  $19.7^\circ$ ,  $43.0^\circ$ ,  $68.1^\circ$ ,  $94.6^\circ$ ,  $117.0^\circ$ ,  $142.5^\circ$ , and  $169.2^\circ$ , respectively. Right column: corresponding normalized RF filter responses (blue: experiment, red: simulation). From top to bottom: RF filters centered at 0.85 GHz, 1.96 GHz, 3.05 GHz, 4.24 GHz, 5.26 GHz, 6.40 GHz, and 7.51 GHz. . . . . 80
- 5.7 Simulation of TSM states. The intracavity waveform evolutions of all the possible excitations of two-soliton states are shown. In total seven distinct steady states are observed, where the angle in each plot indicates the relative angle between the two solitons. The simulation is implemented based on the perturbed Lugiato–Lefever equation (LLE). . . . . 81
- 5.8 Analysis of relative angles between two solitons. (a) One example of the simulated TSM intracavity intensity profile (blue), where AMX-induced background modulation is observed. The red and green lines respectively indicate the measured and simulated possible azimuthal angles between two solitons. (b) Simulation of the intracavity waveform evolution of TSM for robustness test. First, TSM state with relative angle of  $168.0^\circ$  is excited by scanning the pump over the resonance. Once the TSM becomes stable, a  $10.0^\circ$  perturbation is introduced to one of the solitons at white dashed line. The relative angle will re-stabilize to the original angle of  $168.0^\circ$  after a period of free running. . . . . 82
- 5.9 TSM-based RF filters from multiple resonances. (a) Left: RF filters centered at 1.83 GHz, 2.83 GHz, 3.94 GHz, 4.95 GHz, 6.00 GHz, and 7.06 GHz are obtained at resonance of 1555.1 nm. Right: RF filters centered at 0.90 GHz, 2.07 GHz, 3.23 GHz, 4.52 GHz, 5.55 GHz, and 6.90 GHz are obtained at resonance of 1556.8 nm. (b) Left: experimentally retrieved (solid lines, top) and simulated (dashed lines, bottom) two-soliton angles at resonances of 1555.1 nm, 1556.0 nm, and 1556.8 nm. Right: the synthesized RF filter frequencies versus their underlying two-soliton angles retrieved from TSM spectra. The dashed line denotes the linear dependence between them. . . . . 83

5.10 Proof-of-concept filter reconfiguration experiment using TSM-based RF filters. Two phase-shift keying (PSK) signals with 40 Mb/s modulation at 1.96 GHz and 20 Mb/s modulation at 3.05 GHz, are filtered by the TSM-based RF filters configured at 1.96 GHz and 3.05 GHz, respectively. (a) From top to bottom: electrical spectra of original RF signal, signal after 1.96 GHz filter, and signal after 3.05 GHz filter. (b) Waveform after 1.96 GHz filter (top) and waveform after 3.05 GHz filter (bottom). . . . .	84
5.11 Link performance optimization of the RF filter. Gain and noise figure (NF) of the RF filter based on 4-PSC versus the bias of MZM (a) without EDFA at the MZM output (b) with EDFA at the MZM output. Quad: quadrature; MITP: minimum transmission point. . . . .	85







## List of Tables

5.1	Comparison of RF photonic filters based on multi-wavelength sources. . . . .	87
-----	--	----



# Acronyms

<b>ADM</b>	Add-drop multiplexing	<b>LIDAR</b>	Light detection and ranging
<b>AMX</b>	Avoided mode crossing	<b>LLE</b>	Lugiato-Lefever equation
<b>ASE</b>	Amplified spontaneous emission	<b>MI</b>	Modulational instability
<b>AWG</b>	Arbitrary waveform generator	<b>MATP</b>	Maximum transmission point
<b>BER</b>	Bit error rate	<b>MITP</b>	Minimum transmission point
<b>CW</b>	Continuous-wave	<b>MLL</b>	Mode-locked laser
<b>DC</b>	Direct current	<b>MMI</b>	Multimode interference
<b>DCF</b>	Dispersion compensating fiber	<b>MZI</b>	Mach-Zehnder interferometer
<b>DLI</b>	Delay line interferometer	<b>MZM</b>	Mach-Zehnder modulator
<b>DMD</b>	Digital micromirror device	<b>NLSE</b>	Nonlinear Schrödinger equation
<b>DPH</b>	Double-phase hologram	<b>OAM</b>	Orbital angular momentum
<b>DP-MZM</b>	Dual-parallel Mach-Zehnder modulator	<b>OFDM</b>	Orthogonal frequency-division multiplexing
<b>DPSK</b>	Differential-phase-shift-keying	<b>OSA</b>	Optical spectrum analyzer
<b>DSB</b>	Double-sideband	<b>OSNR</b>	Optical signal-to-noise ratio
<b>EAM</b>	Electro-absorption modulator	<b>OSO</b>	Optical sampling oscilloscope
<b>EDFA</b>	Erbium-doped fiber amplifier	<b>OTDM</b>	Orthogonal time-division multiplexing
<b>EO</b>	Electro-optic	<b>OTDR</b>	Optical time-domain reflectometer
<b>EOM</b>	Electro-optic modulator	<b>PC</b>	Polarization controller
<b>ESA</b>	Electrical spectrum analyzer	<b>PD</b>	Photodetector
<b>FEC</b>	Forward error correction	<b>PM</b>	Phase modulator
<b>FIR</b>	Finite impulse response	<b>PSC</b>	Perfect soliton crystals
<b>FSR</b>	Free spectral range	<b>PSK</b>	Phase-shift keying
<b>FWHM</b>	Full-width-half-maximum	<b>QAM</b>	Quadrature amplitude modulation
<b>GCD</b>	Greatest common divisor	<b>QCL</b>	Quantum cascade laser
<b>GVD</b>	Group velocity dispersion	<b>RF</b>	Radiofrequency
<b>ISI</b>	Inter-symbol interference	<b>RoF</b>	Radio-over-fiber
<b>LCFBG</b>	Linearly chirped fiber Bragg grating	<b>RRM</b>	Repetition-rate multiplication
<b>LCM</b>	liquid crystal modulator	<b>SAM</b>	Spin angular momentum
<b>LCoS</b>	liquid crystal on silicon	<b>SDM</b>	Space-division multiplexing
<b>LG</b>	Laguerre-Gaussian	<b>SLM</b>	Spatial light modulator
		<b>SMF</b>	Single-mode fiber

## Acronyms

---

**SMSR** Side mode suppression ratio

**SPM** Self-phase modulation

**SSB** Single-sideband

**TDL** Tapped delay line

**TDM** Time-division multiplexing

**TSM** Two-soliton microcomb

**VNA** Vector network analyzer

**WDM** Wavelength-division multiplexing

**WSS** Wavelength selective switch

# 1 Introduction

## 1.1 Overview of optical frequency combs

Optical frequency combs, as their name implies, are a series of phase-locked, equidistant laser lines in the frequency domain [1–7]. The time and frequency pictures of the optical frequency combs are depicted in Figure 1.1. In the frequency domain, the comb lines are equally spaced by the comb free spectral range (FSR), or equivalently the repetition-rate  $f_{\text{rep}}$ , similar to hair combs. The absolute frequency of each comb component can be indexed as  $f_n = n f_{\text{rep}} + f_o$ , with  $f_o$  being the residual carrier-envelope offset frequency, and  $n \in \mathbb{N}_+$  being typically large number. The temporal waveform of the combs is linked to their spectra by Fourier-transform, which is repetitive and the period is the inverse of the frequency grid, i.e.  $T = 1/f_{\text{rep}}$ . Frequency combs were traditionally generated from mode-locked lasers (MLLs), whose comb lines are all in-phase so as to produce ultrashort pulses in the time domain. For such combs with in-phase/linear-phase relation among the comb lines, the temporal pulse is transform-limited and the pulse width is inversely proportional to the comb bandwidth. The carrier-envelope offset frequency  $f_o$  is resulted from the carrier-envelope phase offset  $\Delta\phi$  between adjacent pulses, related by  $2\pi f_o = \Delta\phi f_{\text{rep}}$ .

There are many types of MLLs. In essence, their working principle are similar, all require phase locking of the cavity modes within the gain profile [8]. The mode-locking can be either achieved actively, for example using external amplitude or phase modulation, or passively by saturable absorber or Kerr-lens. Regarding their actual implementations, MLLs can be quite different from dye lasers in the early days, to solid-state lasers [9], fiber lasers [10], and semiconductor lasers [11]. They have evolved significantly in terms of size, and cost, stability, and performance since their first demonstration. Overall, the typical repetition-rates  $f_{\text{rep}}$  of passive MLLs fall in the order of MHz to several GHz, which are in general inversely related to their cavity lengths.

Apart from mode-locked lasers, there are also other frequency comb sources. Electro-optic (EO) combs are obtained by external modulation of continuous-wave (CW) lasers in electro-optic modulators (EOMs) [12, 13]. Their repetition-rates are determined by the fundamental

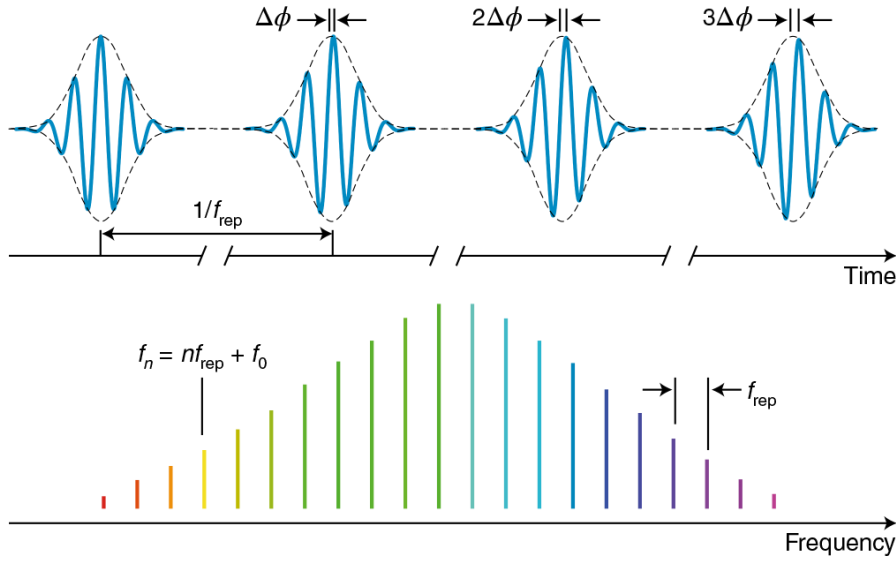


Figure 1.1 – Time and frequency representations of optical frequency combs. In the time domain, frequency combs correspond to periodic optical pulse trains with period  $T = 1/f_{\text{rep}}$ .  $\Delta\phi$  is the carrier-envelope phase offset. In the frequency domain, combs are a series of discrete laser lines equally spaced by the comb repetition-rate  $f_{\text{rep}}$ . The absolute frequency of  $n$ -th comb line is given by  $f_n = n f_{\text{rep}} + f_0$ , where  $f_0$  is the carrier-envelope offset frequency that relates to  $\Delta\phi$  as  $2\pi f_0 = \Delta\phi f_{\text{rep}}$ . Adapted from [6].

frequencies of the driving radiofrequency (RF) signals, thus being fully flexible and simultaneously well-defined. Owing to the large bandwidths of EOMs, the EO comb repetition-rates can be operated at the range up to tens of GHz. Noticeably, this is generally higher than the repetition-rates of MLLs. Also unlike the MLLs, the repetition-rates of EO combs can be freely tuned due to their cavity-less operation.

Recently, optical combs based on microresonators have become as emerging compact and broadband comb sources [14–16]. They are often termed as Kerr combs or microcombs. The typical repetition-rates of microcombs are even higher than EO combs, which are in the range between tens of GHz to several THz due to their miniaturized cavities. The comb lines are initiated via cascaded four-wave mixing process, then entering into mode-locked states with the formation of localized temporal structures. The ever-maturing on-chip integration of microresonators has facilitated dispersion engineering for microcomb generation, and possesses the potential for mass production [17].

Frequency combs based on quantum cascade lasers (QCLs) with direct electrical pumping have made mid-infrared and THz electromagnetic radiation within reach [18, 19]. QCL-combs are based on the intersubband transitions in sandwiched quantum-well heterostructures. Unlike the common interband semiconductor lasers, the mode-locking of QCL-combs are achieved by the active RF frequency modulation instead of producing short pulses.

Optical frequency combs are central to enormous applications listed below [4, 5, 7]:

**Optical clockworks and metrology.** The precision of time counting scales with the clock frequency in the time-keeping roadmap [4]. While the current definition of second is given by the Cesium microwave frequency standards, optical frequency combs hold a promise for next-generation atomic clocks. Indeed, the fractional uncertainty of the state-of-the-art optical synthesizer is down to  $1 \times 10^{-19}$  level [20]. Optical frequency combs provide direct phase-coherent chain between the RF and the optical domains, therefore being called clockworks or gearbox. This would generally require frequency combs with octave spanning to be able to retrieve and stabilize the carrier-envelope offset frequencies  $f_o$ , through the frequency-doubling the red part of the spectra and heterodyning with the blue part. When self-referenced, they can be referenced at the RF to form the optical synthesizers. Or reversibly, frequency combs can be locked to some ultra-stable optical transitions of ions and atoms, and then converting the references back to the RF domain.

**Molecular spectroscopy.** Optical frequency combs with fine-tooth spacing and broad coverage are suitable for molecular spectroscopy. Most of the molecule-fingerprints are at the mid-infrared (2-20  $\mu\text{m}$ ) and ultra-violet ( $< 400 \text{ nm}$ ) wavelength regions [6]. Both direct-comb spectroscopy and dual-comb spectroscopy (two phase-locked frequency combs with slightly offsetted repetition-rates) [21] have been used for this purpose.

**Ranging.** Light detection and ranging (LIDAR) with optical frequency combs empowers rapid and high-precision distance measurements [22]. The most straightforward implementation of LIDAR is based on the time-of-flight measurement, with resolution ultimately limited by the optical pulse width but in real world by the response time of photodetector (PD). Linear optical sampling approach could circumvent this limit by employing dual combs to achieve sub-wavelength resolution and wide unambiguity range [23].

**Spectrograph calibration.** High-resolution spectrographs are key instruments in astrophysics for the discovery and characterization of exoplanets. Frequency combs of high repetition-rates (tens of GHz) could enable precise calibration of such astronomical spectrographs [24]. In this sense, EO combs [25] and microcombs [26] are favored for their large comb line spacing.

**Optical communications.** In order to take advantages of the ample bandwidth resources at optical carrier frequency, wavelength-division multiplexing (WDM) is widely adopted in optical communication systems to increase the data rate. Optical frequency combs can be employed as independent optical channels in place of the current large laser bank [27, 28]. Moreover, the mutual coherence of individual comb lines brings additional advantages in simplifying the receiver scheme with joint signal processing [29]. The time domain equivalence of WDM system is the optical time-division multiplexing (TDM) [30, 31]. Since the TDM systems are densely multiplexed in time, they require short optical pulses to encode the information. As mentioned before, optical pulse sources essentially correspond to frequency combs.

**Microwave photonics.** Using photonic approaches to generate, process, and distribute microwave signals provides added benefits, unparalleled by the microwave engineering tech-



niques alone [32, 33]. Optical frequency combs intrinsically combine the two worlds. One natural application is generating ultra-low phase noise microwave via optical frequency division [34, 35]. Such optical-to-microwave translation preserves the fractional frequency instability. With fully stabilized combs being locked to optical reference, the division process could greatly reduce the phase fluctuations of the generated microwave frequency.

In addition to microwave synthesis, line-by-line shaping of the comb spectra enables arbitrary microwave waveform generation [36]. Also for microwave signal processing, finite impulse response (FIR) microwave photonic filters can be constructed based on frequency combs and dispersive propagation [37]. There are other applications using combs for true-time delay beamforming and RF channelized receiver [38].

## 1.2 Thesis motivation

The ability to control and shape optical frequency combs are crucial to many applications mentioned in Section 1.1, particularly for optical communications and microwave photonics [39]. Perhaps the most well-established comb shaping device is the Fourier transform pulse shaper, where each frequency component is dispersed by a grating and mapped to different spatial location, addressed with a spatial light modulator (SLM) and then recombined [40, 41]. The typical spectral resolution of such device is around 10 GHz, like the commercially available products - WaveShaper series from Finisar, but can also be as fine as 1 GHz at the cost of bandwidth and loss [42]. This opens up line-by-line shaping regime of EO combs [43] and microcombs [44] for the generation and measurement of optical waveforms and spectra. To minimize the size of such free-space shaping devices, there have been prototypes that build the shapers fully on-chip based on arrayed waveguide gratings and tuning elements [45, 46]. Apart from spectral domain shaping, frequency combs can also be shaped in the time domain. In this case, the temporal pulses are split into multiple copies, each being delayed incrementally and adjusted in amplitudes and phases, and then recombined [47, 48]. Such time-domain pulse shaping devices could easily process small FSR combs, but are not energy-preserving due to their interferometric configurations. Recently, a novel shaper design with MHz spectral resolution was demonstrated based on time-to-frequency mapping in a recirculating frequency shifting loop [49].

Besides the full amplitude and phase control of optical frequency combs, a lot of applications require specifically the adjustment of the comb FSR and the pulse repetition-rate. To increase the comb FSR, pulse shapers can be simply programmed to transmit one out of several lines periodically while attenuating all the other frequency components. This is attractive, for example, in the photonic synthesis of wireless link towards THz carrier frequency [50]. On the other hand, reducing the comb FSR is generally realized via pulse picking technique, where the initial high repetition-rate pulse train is down-sampled by temporal gating. The FSR-reduced combs would provide finer resolution for spectroscopy, and lead to increased pulse energy after amplification favored by optical nonlinear processes [51]. Overall, the above-mentioned

approaches to increase or decrease the comb FSRs discard part of the energy either in the frequency or time domain.

On the contrary, temporal Talbot effect [52] and spectral Talbot effect [53] are in principle lossless ways to increase the pulse repetition-rate and reduce the comb line spacing, respectively. Temporal self-imaging appears when the frequency combs undergo specific amount of second-order dispersion. This can be realized by propagation through optical fiber [54], linearly chirped fiber Bragg grating (LCFBG) [55], or in a pulse shaper programmed with certain quadratic phase sequence (Talbot phases) just as if the combs propagate [56]. Spectral Talbot effect is the frequency domain counterpart of the temporal self-imaging phenomenon. Instead of gating the pulses, the multi-level phase (Talbot phase) modulation of the pulses would insert new comb lines between the original comb intervals [57]. Moreover, recent studies show that the temporal and spectral Talbot effects are inherently connected, which can losslessly transfer the optical pulse trains from one comb FSR to another [58, 59].

All of the shaping techniques described above are external, which control the optical frequency combs that have already been generated. Alternatively, they may be shaped internally at the generation stage. For instance, parabolic phase modulation maps the flat-top pulse shape to equalized comb spectra [60], and then can be further compressed to near transform-limited pulses by a spool of single-mode fiber (SMF) [61]. Such time-to-frequency mapping approach alleviates the use of programmable shaper for short pulse formation. In regards to microcombs, perfect soliton crystals (PSC) are equally-spaced solitons formed under low pump power [62]. Interestingly, the number of solitons varies with pumped resonances. As a result, the comb FSR can be internally controlled by pumping different resonances without additional efforts. Given the variety and impact of optical frequency combs are now taking, the investigation of new shaping concepts is timely.

### 1.3 Thesis goal and contribution

The thesis explores novel generation and shaping techniques of optical frequency combs, mainly for the applications in microwave photonics and optical communications. Two types of comb sources - EO combs and integrated microcombs are studied throughout the thesis. Overall, the thesis is divided into three parts: shaping and applications of optical sinc pulses, temporal and azimuthal Talbot shaping, and shaping of soliton microcombs for RF photonic filters.

The first part of the thesis is about a special type of frequency comb sources when all the comb lines are of equal amplitudes and linear phase relation. In the time domain, this translates into a periodic optical sinc pulse train [63]. Compared to Gaussian pulses, such sinc pulses can be more densely packed in time, overlapping with each other while still maintaining orthogonality. In this manner, Nyquist orthogonal time-division multiplexing (OTDM) superchannels are formed, achieving higher spectral efficiency than the conventional TDM systems [64]. Indeed, Nyquist OTDM is nothing else but the time domain equivalence of the orthogonal frequency-

division multiplexing (OFDM) systems (likewise OFDM achieves higher spectral efficiency than conventional WDM systems) [65]. The generation of high-quality optical sinc pulses is the first step towards building Nyquist OTDM transmitter, and is preferably without the aid of programmable shaper. There are indeed several demonstrations of direct synthesis of optical sinc pulses, but either with limited flexibility for the number of subchannels [63, 66] or with non-zero roll-offs [67]. Flexible optical sinc pulse generators remain elusive. At the receiver side, Nyquist OTDM signals are generally demultiplexed via optical sampling [68, 69]. Additional functionality comes from the add-drop multiplexing (ADM), which not only extracts the target subchannel but replaces it with a new data stream. However, till now, there is no viable ADM architecture for Nyquist OTDM similar to what has been demonstrated for OFDM system [70]. Also, it will be interesting to look for new applications of sinc pulses. In the first part, a flexible synthesis of optical sinc pulses is provided, and is then used for add-drop multiplexing of Nyquist OTDM systems and RF photonic filters.

Then the second part of the thesis is outreached to a more general case, when the phases between the comb lines no longer satisfy linear relation but complex phase pattern. As mentioned earlier, temporal Talbot effect occurs when the comb lines pick up Talbot phases. In this scenario, the initial optical pulses redistribute their energy to self-imaged pulses, multiplying the pulse repetition-rate without changing the comb FSR. Temporal Talbot effect has been applied to synthesize radio-over-fiber (RoF) link [50], to generate high power THz frequency [71], and to mitigate nonlinear distortion of ultra-short pulse delivery [72]. It is highly desired to integrate this shaping function to photonic chips, and not until recently is the demonstration of on-chip temporal Talbot multiplier [73]. However, such design is not tunable in wavelength and has limited processing bandwidth. Therefore, more flexible schemes compatible with photonic integration are needed. Additionally, it is interesting to extend the self-imaging concept to a new degree of freedom - the orbital angular momentum (OAM) mode of light, which shares similar mathematical foundation as the frequency comb mode [74, 75]. Indeed, some relevant studies have shown agreement of this duality [76, 77]. In the second part, a novel temporal Talbot shaping approach amenable to photonic integration is proposed, and also the azimuthal Talbot effect is demonstrated.

The third part of the thesis is related to tailoring microcombs for microwave photonic purposes. Compared to traditional comb sources, microcombs not only reduce the size and cost of the systems, but could bring unique advantages and unlock new RF photonic applications thanks to their broad bandwidths and large comb FSRs [38, 78]. Specifically, the thesis is focused on the integrated microcomb-based RF photonic filters. For this type of RF filters, the filter functions are defined by the optical comb spectra, where each comb line corresponds to the tap of the FIR filters [79, 80]. Adapting microcombs for comb-based RF filters enhances the filters with broader spur-free range, lower latency, less dispersion induced fading, and increased number count of filter taps [81–83]. However, all these demonstrations are based on the microcombs that do not directly translate into the desired filter functions. Additional programmable pulse shapers are required to trim the comb spectra, in order to achieve proper suppression ratio and reconfigurability. Undoubtedly, this comprises the benefits of using

microcombs while bulky equipment is parasitic. On the other hand, it is well-known that a single microresonator device could actually produce versatile soliton formats thereby various comb spectral patterns. As such, the third part of the thesis explores the internal control of soliton configurations of microresonators, so as to achieve RF photonic filtering without external shaping.

## 1.4 Thesis structure

**Chapter 2** describes the general principles involved in this study. It includes the basis of various EOM structures and optical microresonators for EO comb and microcomb generation, respectively. In addition, the techniques of spatial and temporal light shaping are also discussed, with a particular interest of Talbot self-imaging in diverse representations.

**Chapter 3** deals with a special type of optical combs that are of periodic sinc shape in time. First, such optical pulses are generated in a simple yet fully flexible approach, which is based on EOM driven by synchronized multi-harmonic RF signals. Then the rectangular shape of the sinc pulse spectrum is utilized, for the shaping of near-perfect sinc filter response in RF domain. Also exploiting the temporal shaping capability of EOM, a viable ADM architecture is envisioned for optical communication system that uses sinc pulse as information carrier.

**Chapter 4** describes the Talbot phenomena in time and azimuthal angle. The temporal Talbot effect shapes frequency combs with Talbot phases, leading to the repetition-rate multiplication (RRM) of corresponding pulse trains in time. Here a novel temporal Talbot multiplier is implemented based on the interference in a simple optical tapped delay line (TDL) structure, which is well-known for RRM shaping but via the spectral amplitude filtering. Moreover, the self-imaging concept is reached out to the shaping of light intensity petals in azimuthal angle, based on the interference of multiple OAM modes with Talbot initial phases.

**Chapter 5** explores the internal microcomb shaping in optical microresonators for the use in RF photonic filters. The smooth spectra of soliton microcombs guarantee the RF filters with descent passband suppression ratio, while the possible direct generation of various soliton states enables the RF filters with wide reconfigurability. Specifically, the PSC states and the two-soliton states with versatile relative angles between them are harnessed. The performances of soliton-based RF filters are characterized and compared to other RF photonic filters of the same category.

**Chapter 6** concludes the studies presented in this thesis and suggests future research opportunities based on the current work.



## 2 General principles

In this chapter, I will briefly introduce the general background involved in the study of the thesis. Since it mainly deals with the generation, shaping, and applications of EO combs and microcombs, the working principles of modulators and microresonators are described. Various types of lithium niobate ( $\text{LiNbO}_3$ ) EOMs and liquid crystal based SLMs are visited, in the perspectives of comb generation and light field shaping, respectively. I will then give a short introduction to the concept of Talbot effect. Lastly, I will discuss the basis of microcomb generation based on silicon nitride ( $\text{Si}_3\text{N}_4$ ) microresonators.

### 2.1 Electro-optic modulator

EOMs are indispensable electro-optical components that have been used in almost all photonic-related applications, ranging from fiber-optic communications, microwave photonics, distributed fiber sensing [84], to quantum optics [85]. Basically, EOMs transfer electrical signals into the optical domain, where some unique advantages of optics can be harnessed, such as the extreme low loss of optical fibers ( $\sim \text{dB/km}$ ) for signal transmission, and massive bandwidth for data stream parallelization (e.g. WDM). Most commonly used EOMs are based on  $\text{LiNbO}_3$ . They typically have electrical bandwidths in the tens of GHz, while some customized options could go beyond 100 GHz. Also, EOMs working at different spectral regions are now commercially available from visible band to wavelength beyond  $2 \mu\text{m}$ . The half-wave voltage (the voltage required to induce a  $\pi$  phase shift,  $V_\pi$ ) of the EOMs are wavelength dependent. In the telecom-band around 1550 nm, which is also the wavelength we are working with, the  $V_\pi$  of commercial EOMs generally range from 3 V to 10 V. However, it is noted that with the recent integrated thin-film  $\text{LiNbO}_3$  technology, EOMs of  $V_\pi$  as low as 1.4 V have been demonstrated thanks to the much reduced gap between the electrodes [86]. This ultra-high RF-optical transduction is highly desired in data communication, as it could be directly driven by CMOS-compatible voltage [86], and also in RF photonics to boost the link gain [87].

The EO effect of  $\text{LiNbO}_3$  modulator is also known as the Pockels effect. It is a second-order  $\chi^{(2)}$  process only naturally arising in non-centrosymmetric materials [88]. Due to the Pockels effect,

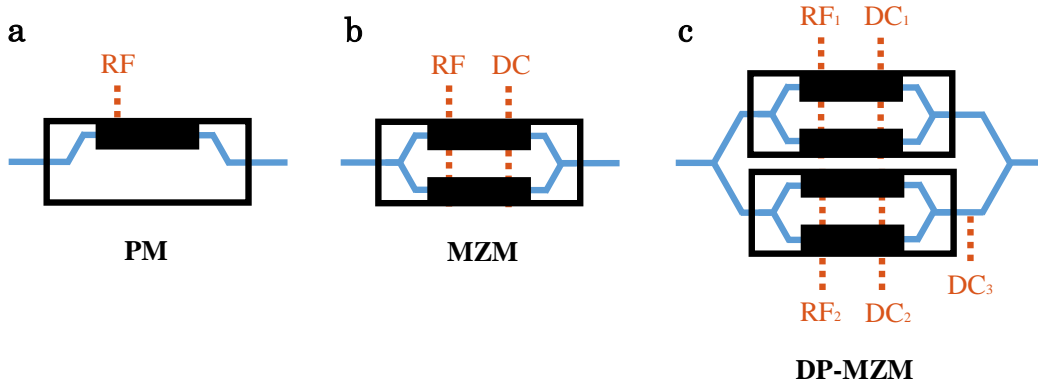


Figure 2.1 – Schematics of various types of Electro-optical modulators (EOMs). (a) PM (phase modulator); (b) MZM (Mach-Zehnder modulator); (c) DP-MZM (dual-parallel Mach-Zehnder modulator). The black rectangle represents the electro-optic modulation region, where RF and DC signals are applied.

the refractive index of LiNbO<sub>3</sub> changes under the external applied voltage. The refractive index change would induce the phase change of the incoming optical wave, thereby achieving phase modulation. EOMs used throughout the thesis are mainly phase modulator (PM), Mach-Zehnder modulator (MZM), and dual-parallel Mach-Zehnder modulator (DP-MZM), which are depicted in Figure 2.1. Their properties and working principles are provided below, serving as guidelines for EO comb generation and optimal modulation schemes used in this thesis.

**Phase modulator.** To illustrate the phase modulation, here we consider that a CW laser with amplitude  $E_0$  at optical frequency  $\omega_0$  is sent to the PM. When an electrical voltage  $V(t) = V_{RF} \sin(\omega_m t)$  is applied to the PM with  $V_{RF}$  the amplitude and  $\omega_m$  the modulation frequency, the output optical field is thus modulated and given by:

$$E = E_0 \exp\left(i\omega_0 t + i \frac{\pi V_{RF}}{V_{\pi, RF}} \sin(\omega_m t)\right) \quad (2.1)$$

where  $V_{\pi, RF}$  is the half-wave voltage at RF frequency. Note that without loss of generality, the trivial static phase resulted from optical propagation is omitted above. We also denote  $\beta = \pi V_{RF} / V_{\pi, RF}$  as the modulation index for simplicity. Using Jacobi–Anger expansion, Eq. (2.1) rewrites:

$$E = E_0 \exp(i\omega_0 t) \left\{ \sum_{n=-\infty}^{\infty} J_n(\beta) \exp(in\omega_m t) \right\} \quad (2.2)$$

where  $J_n(\beta)$  ( $n \in \mathbb{Z}$ ) is the Bessel function of the first kind. It can be seen that new sidebands at frequencies  $\omega_0 + n\omega_m$  are generated through phase modulation, with amplitudes  $J_n(\beta)$  set by the modulation index and mode number. This lays the foundation of EO comb generation. The intrinsic property of the Bessel function  $J_{-n}(\beta) = (-1)^n J_n(\beta)$  tells that the sideband pairs generated by phase modulation are always out-of-phase. When the modulation index is

relatively small, not so many sidebands are excited. It is noted that, no matter how small the modulation index is (consider the modest 3 modes,  $\omega_0 - \omega_m$ ,  $\omega_0$ , and  $\omega_0 + \omega_m$  in Figure 2.2 a), these modes cannot follow the linear phase relation (the relative phases will be  $\pi, 0, 0$ ), while linear phase is desired for pulse generation. When being detected at the photodetector (PD), the beating signals from the sidebands and optical carrier will be canceled out. This is quite obvious from the time domain, as the phase modulation does not change the light intensity. That is to say, although sideband combs are created, there is no optical pulse formation (Figure 2.2 a).

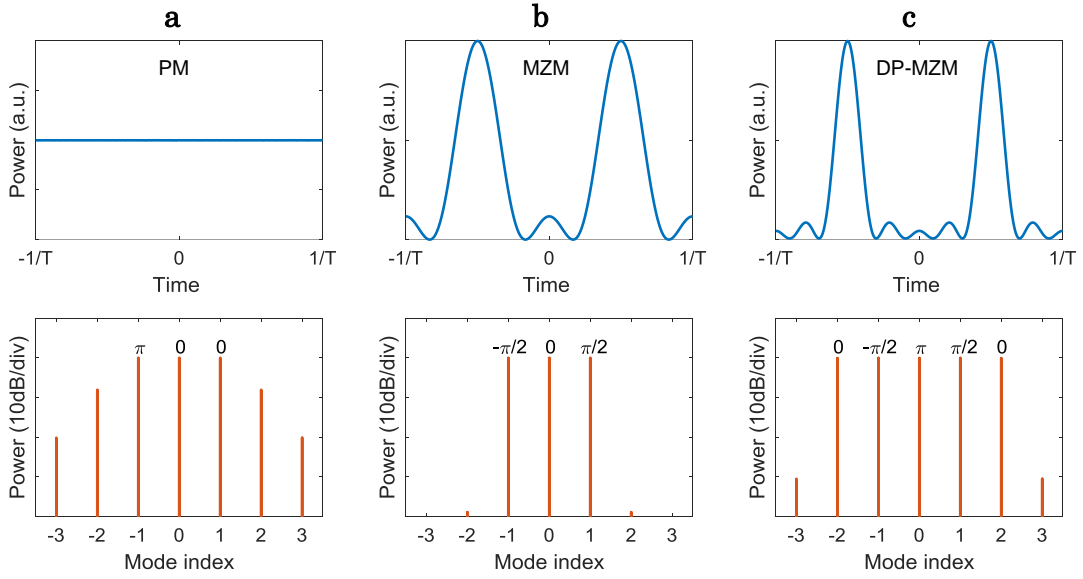


Figure 2.2 – Examples of the waveforms and spectra based on EOMs driven by a single RF frequency. (a) PM; (b) MZM; (c) DP-MZM. The operation parameters of the DP-MZM are retrieved from [89].  $T = 2\pi/\omega_m$  is the repetition period, the mode indices are indexed with respect to the optical carrier, and the phases of central comb modes are labeled. MZM and DP-MZM can generate sinc pulses with 3 and 5 comb lines, but not PM.

**Mach-Zehnder modulator.** A MZM is constructed by putting the phase modulators in a Mach-Zehnder interferometer (MZI), as depicted in Figure 2.1 b. Through interference between the two arms, the phase modulation is converted to intensity modulation. Therefore, sometimes the MZM is also known as intensity modulator or amplitude modulator. There are basically two categories of MZMs depending on the way they are driven, being either push-pull (the electrical signal applied differentially to both arms) or unbalanced (the electrical signal applied only to one arm). Here we confine our discussion to only the push-pull MZMs, as they are chirp-free (no parasitic phase modulation) and are also more widely used. Apart from the RF uploading port, there is also a direct current (DC) bias port in the MZM to modify the relative static phase between the two arms.

We assume here that the input and output couplers of the MZM equally splits and combines



the optical power with no extra phase shift (the extra phase can be included into the DC bias). Consider a CW laser directed to a MZM driven by a sinusoidal wave, the output optical field becomes:

$$\begin{aligned}
 E &= \frac{E_0}{2} \exp(i\omega_0 t) \left\{ \exp\left(i \frac{\pi V_{RF}}{2V_{\pi,RF}} \sin(\omega_m t) + i \frac{\pi V_{DC}}{2V_{\pi,DC}}\right) + \exp\left(-i \frac{\pi V_{RF}}{2V_{\pi,RF}} \sin(\omega_m t) - i \frac{\pi V_{DC}}{2V_{\pi,DC}}\right) \right\} \\
 &= E_0 \exp(i\omega_0 t) \cos\left(\frac{\pi V_{RF}}{2V_{\pi,RF}} \sin(\omega_m t) + \frac{\pi V_{DC}}{2V_{\pi,DC}}\right)
 \end{aligned} \tag{2.3}$$

where  $V_{DC}$  and  $V_{\pi,DC}$  are the DC bias voltage and the DC half-wave voltage, respectively. Here the optical field experiences an opposite phase shift in the two arms for both the RF signal and DC bias. Also we define  $\beta = \pi V_{RF}/2V_{\pi,RF}$  and  $\psi = \pi V_{DC}/2V_{\pi,DC}$  as the normalized RF power and the normalized DC bias, respectively. By using trigonometric identity and Jacobi-Anger expansion, Eq. (2.3) rewrites:

$$\begin{aligned}
 E &= E_0 \exp(i\omega_0 t) \left\{ \cos(\beta \sin(\omega_m t)) \cos \psi - \sin(\beta \sin(\omega_m t)) \sin \psi \right\} \\
 &= E_0 \exp(i\omega_0 t) \left\{ \cos \psi \left[ J_0(\beta) + \sum_{n=1}^{\infty} J_{2n}(\beta) (\exp(i2n\omega_m t) + \exp(-i2n\omega_m t)) \right] + \dots \right. \\
 &\quad \left. i \sin \psi \left[ \sum_{n=1}^{\infty} J_{2n-1}(\beta) (\exp(i(2n-1)\omega_m t) - \exp(-i(2n-1)\omega_m t)) \right] \right\}
 \end{aligned} \tag{2.4}$$

It can be seen that new comb modes spaced by  $\omega_m$  are also generated. However, unlike for the phase modulation, here the DC bias offers additional control on the odd and even sidebands. For example, when  $\psi = 0$  (or  $\pi/2$ ) all the odd (or even) numbers of the frequency modes are suppressed. Such bias conditions are known as maximum transmission point (MATP,  $\psi = 0$ ), minimum transmission point (MITP,  $\psi = \pi/2$ ), respectively. Both cases would increase the comb FSR by two-times while  $\psi = \pi/2$  suppresses the original optical carrier. We also consider the case when the modulation index is small, and only the first 3 modes ( $\omega_0 - \omega_m$ ,  $\omega_0$ , and  $\omega_0 + \omega_m$ ) are generated. The relative phases between them are  $-\pi/2$ ,  $0$ ,  $+\pi/2$ , which follow the linear phase relation and give rise to optical pulses in time. Adjusting the bias  $\psi$  could balance the power of the carrier and the sidebands for sinc pulse generation (Figure 2.2 b) [63]. While the relative phases for the first 5 modes are  $0$ ,  $-\pi/2$ ,  $0$ ,  $\pi/2$ ,  $0$  that by no means obey the linear phase criterion.

**Dual-parallel Mach-Zehnder modulator.** DP-MZM can be viewed as an optical device consisting of two child MZMs embedded in a parent MZI (Figure 2.1 c). An extra phase shifter (controlled by  $DC_3$ ) is nested in the parent MZI to adjust the relative phase shift between the main upper and lower arms. Such topology allows for the arbitrary amplitude and phase modulation of the optical wave, which is appealing for coherent communications [90] and microwave photonics [91]. In telecommunications, a DP-MZM is also called an IQ modulator, where the in-phase and quadrature parts of complex signals can be separately uploaded via the two MZMs. Especially with the development of coherent detection techniques, quadrature amplitude modulation (QAM) becomes the most important approach to increase the spectral

efficiency. It is also worth to mention that ultra-high QAM constellation has recently been achieved [92]. For microwave photonics, the advanced modulation techniques based on DP-MZM could mitigate the dispersion induced power fading [37, 80] and obtain ultra-high rejection RF notch filter [93].

The governing equation of the DP-MZM can be formulated as:

$$E = \frac{E_0}{2} \exp(i\omega_0 t) \left\{ \cos\left(\frac{\pi \tilde{V}_{RF1}}{2V_{\pi,RF}} + \frac{\pi V_{DC1}}{2V_{\pi,DC}}\right) + \cos\left(\frac{\pi \tilde{V}_{RF2}}{2V_{\pi,RF}} + \frac{\pi V_{DC2}}{2V_{\pi,DC}}\right) \exp\left(i\frac{\pi V_{DC3}}{V_{\pi,DC}}\right) \right\} \quad (2.5)$$

where  $\tilde{V}_{RFk}$  ( $k = 1, 2$ ) denotes the applied RF signal and  $V_{DCk}$  ( $k = 1, 2, 3$ ) denotes the applied DC voltage. Here we have assumed ideal 50/50 couplers and identical half-wave voltages for the embedded modulators. When the DP-MZM is only singly driven ( $\tilde{V}_{RF2} = 0$ ), it could function as sinc pulse generator with 5 comb lines (Figure 2.2 c) [66, 89]. The working principle is straightforward, as the structure is basically a single MZM plus an unmodulated optical carrier. This additional carrier changes the overall carrier to be out-of-phase, making the phase relation between the main 5 modes to be  $0, -\pi/2, \pi, \pi/2, 0$ . The modified phase relation actually obeys the linear phase criterion (the incremental phase is  $-\pi/2$ ). Once the phase relation is met, the amplitude equalization of the 5 comb modes can be simply guaranteed by adjusting the DC bias (Figure 2.2 c).

For most of the applications, both embedded MZMs are driven. As for QAM signaling, the phase shifter is biased at the quadrature ( $\pi V_{DC3}/V_{\pi,DC} = \pi/2$ ). The simple amplitude modulation in the MZMs would give the in-phase and quadrature parts of the signals, and then combine orthogonally at the output of the DP-MZM. In this thesis, we are interested in the modulation scheme of single-sideband (SSB) modulation with the carrier [37, 80], which will be utilized for RF signal upconversion. Since we also want to preserve the phase relation between the SSB and the optical carrier for broad bandwidth, an electrical  $90^\circ$  hybrid is used for RF modulation. Under this condition, we assume  $\tilde{V}_{RF1} = V_{RF} \cos(\omega_m t)$  and  $\tilde{V}_{RF2} = V_{RF} \sin(\omega_m t)$ . We also define as before  $\beta = V_{RF}/2V_{\pi,RF}$  and  $\psi_k = V_{DCk}/2V_{\pi,DC}$  ( $k = 1, 2, 3$ ) for clarity in the expression. Under the small signal approximation, Eq. (2.5) derives:

$$\begin{aligned} E &= \frac{E_0}{2} \exp(i\omega_0 t) \left\{ \cos(\beta \cos(\omega_m t) + \psi_1) + \cos(\beta \sin(\omega_m t) + \psi_2) \exp(i2\psi_3) \right\} \\ &\approx \frac{E_0}{2} \exp(i\omega_0 t) J_0(\beta) (\cos \psi_1 + \cos \psi_2 \exp(i2\psi_3)) + \dots \\ &\quad \frac{E_0}{2} \exp(i(\omega_0 - \omega_m)t) J_1(\beta) (-\sin \psi_1 - i \sin \psi_2 \exp(i2\psi_3)) + \dots \\ &\quad \frac{E_0}{2} \exp(i(\omega_0 + \omega_m)t) J_1(\beta) (-\sin \psi_1 + i \sin \psi_2 \exp(i2\psi_3)) \end{aligned} \quad (2.6)$$

Here the analysis is carried out in the same way as Eq. (2.4), yet being limited to the first-order sidebands under weak RF modulation. It can be seen that, with proper tuning of the three DC bias of the DP-MZM, one of the mode can be suppressed. Moreover, the relative amplitude and phase of the other sideband with regards to the carrier can be arbitrarily set [94]. An

extreme case is the SSB modulation without the optical carrier, indeed DP-MZM is also known as SSB modulator.

## 2.2 Spatial light modulator

Unlike EOMs that modulate the lightwaves in time, SLMs modulate the light beams spatially as the name implies. They are typically used to tailor the wavefront of light, through an array of digitally controlled pixels. Therefore, SLMs have a myriad of use in many forms of imaging systems [95, 96], optical tweezers [97], laser physics [98], optical communications [99], and recently optical computing [100]. Common types of SLMs are liquid crystal modulators (LCMs) and digital micromirror devices (DMDs). In this thesis, LCM is chosen for the light field shaping, and therefore is used interchangeably with the word SLM. Compared to the typical DMDs, LCMs generally offer higher spatial resolution ( $3.74 \mu\text{m}$  for the one we use) and better bit depth (generally 8-bit for SLMs while binary for DMDs). Although the modulation speed of the SLMs ( $\sim 60 \text{ Hz}$ ) are much slower than that of the DMDs ( $\sim 20 \text{ kHz}$ ), there is no issue for the proof-of-concept experiment since no dynamic shaping is involved in this work. The spatial phase modulation of LCM is achieved by applying electrical voltages to the pixels. For each pixel, the embedded liquid crystal molecule changes its orientation according to the magnitude of the voltage applied on it, therefore acquires controllable phase shift [101]. Nonetheless, once the device is well calibrated, it can be easily used by loading computer generated holograms to it, without going to the details of the hardware implementation.

The LCM we use is a liquid crystal on silicon (LCoS) phase-only modulator, working in the reflective manner. It has  $3840 \times 2160$  pixels (4k resolution) and full  $2\pi$  phase range in the telecom-band around  $1550 \text{ nm}$ .

**Spatial shaping.** The main task of using SLM in this work is to implement arbitrary complex amplitude modulation in two-dimensional space. Basically, both amplitude and phase modulation need to be encoded in a phase-only modulator - the most popular LCM available and is also the one we have. This is not trivial, but many approaches have been developed in the past years [101–103]. Although implemented very differently, more or less all these methods rely on diffraction, spatially separating the target field from the rest. Among others, the technique we use is the double-phase hologram (DPH), which also employs an optical  $4 - f$  system with filtering at the Fourier plane [104]. The method is described as follows.

First, an arbitrary field  $U(x, y) = A(x, y) \exp(i\psi(x, y))$  can always be expressed by the summation of two phasors with proper scaling, where  $A(x, y)$  and  $\psi(x, y)$  are the target amplitude and phase distributions. Without loss of generality, we have assumed the maximum value of the amplitude  $A(x, y)$  to be 1 (i.e. the amplitude is normalized). The complex field can be rewritten:

$$U(x, y) = \frac{1}{2} \left\{ \exp(i\psi(x, y) + i \arccos A(x, y)) + \exp(i\psi(x, y) - i \arccos A(x, y)) \right\} \quad (2.7)$$

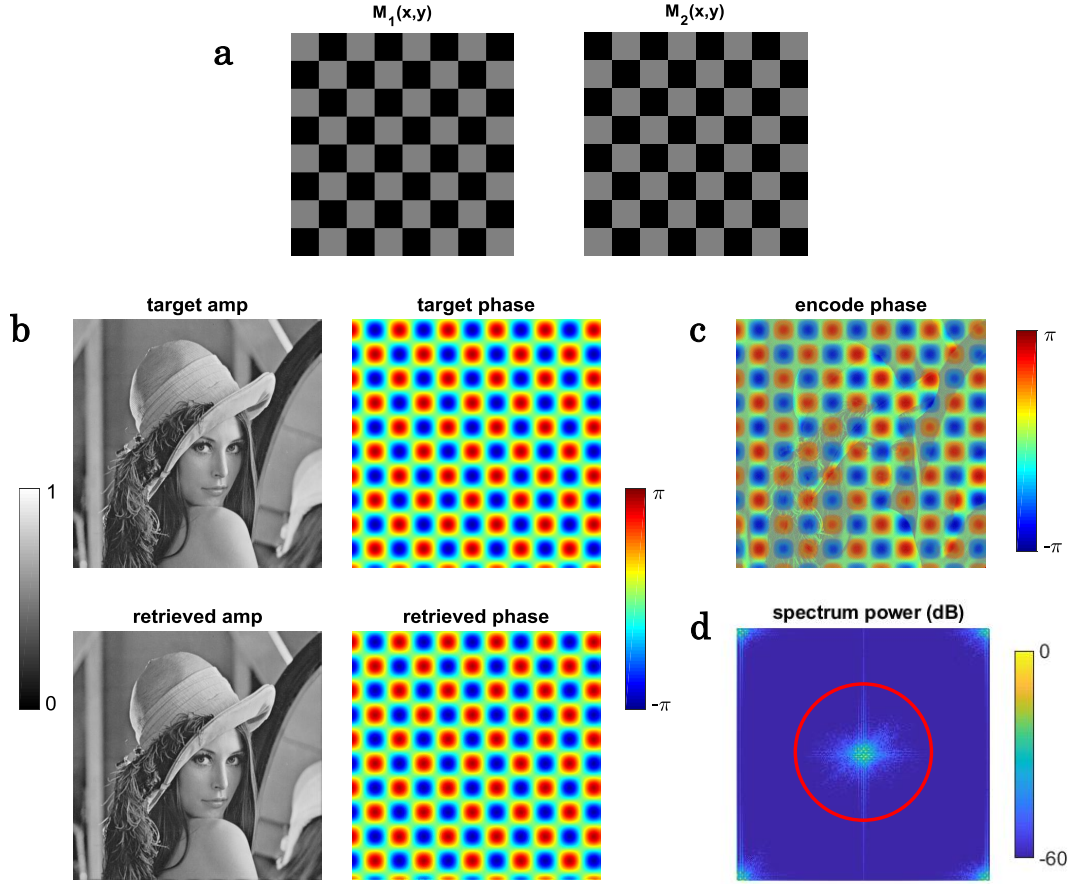


Figure 2.3 – Simulation of the complex amplitude modulation through double-phase hologram (DPH) encoding. (a) Schematic of the complementary checkerboards (gray: modulated, black: unmodulated). The SLM is divided into two checkerboards for the modulation of the two holograms separately. (b) Simulation verification of the DPH encoding scheme. Retrieved amplitude and phase images are in good agreement with the target amplitude and phase images. (c) The phase hologram encoded to the SLM. (d) Normalized power of the Fourier transform of the complex field. Red circle indicates the low-pass filter.

That is, one could construct the complex amplitude function through the summation of two phasor fields. For clarity, we refer them as  $\theta_1(x, y) = \psi(x, y) + \arccos A(x, y)$  and  $\theta_2(x, y) = \psi(x, y) - \arccos A(x, y)$ . To attain the DPH, the pixels of 2D SLM are divided into two subgroups with complementary checkerboard distributions, denoted by  $M_1(x, y)$  and  $M_2(x, y)$  as shown in Figure 2.3 a. The gray and black boxes represent 1 (modulated) and 0 (unmodulated) pixels, respectively. Such checkerboards undergo very high frequency spatial modulation, therefore diffracting the incident light to different spatial spots at the far field. This can lead to amplitude modulation by filtering out part of the light. Suppose the period of modulation is  $p$  (the period

is 2-times the pixel length), the checkerboard fields can be expressed by the Fourier series:

$$M_{1,2}(x, y) = 2 \sum_{n=-\infty}^{\infty} \sum_{m=-\infty}^{\infty} \cos\left(\frac{\pi(n \pm m)}{2}\right) \frac{\sin(\frac{n\pi}{2})}{n\pi} \frac{\sin(\frac{m\pi}{2})}{m\pi} \exp(i2\pi nx/p) \exp(i2\pi my/p) \quad (2.8)$$

Physically,  $n$  and  $m$  stand for the diffraction orders in  $x$  and  $y$  directions, respectively. Here we have assumed the checkerboards to be infinite in space for simplicity, which is reasonable given the large difference between the pixel number in each direction and the period. The encoding strategy here is to associate the two phase patterns  $\theta_1(x, y)$  and  $\theta_2(x, y)$  respectively with  $M_1(x, y)$  and  $M_2(x, y)$ , and then combined as the overall phase pattern  $\theta(x, y)$  to be loaded to the SLM:

$$\theta(x, y) = \theta_1(x, y)M_1(x, y) + \theta_2(x, y)M_2(x, y) \quad (2.9)$$

As for each pixel  $(x, y)$ , it is noted that only one of  $M_1(x, y)$  and  $M_2(x, y)$  is 1 and the other will be 0. Eq. (2.9) can thus be expressed as:

$$\exp(i\theta(x, y)) = \exp(i\theta_1(x, y))M_1(x, y) + \exp(i\theta_2(x, y))M_2(x, y) \quad (2.10)$$

Substituting Eq. (2.8) into Eq. (2.10) derives:

$$\exp(i\theta(x, y)) = \sum_{n=-\infty}^{\infty} \sum_{m=-\infty}^{\infty} \{c_1^{nm} \exp(i\theta_1(x, y)) + c_2^{nm} \exp(i\theta_2(x, y))\} \exp(i2\pi nx/p) \exp(i2\pi my/p) \quad (2.11)$$

where  $c_{1,2}^{nm} = 2 \cos(\pi(n \pm m)/2) \sin(n\pi/2) \sin(m\pi/2) / nm\pi^2$  denote the amplitudes of the diffraction orders. Typically, the frequency content of a conventional phasor is well confined within a certain region, smaller than the frequency grids defined by the diffraction of the checkerboards. This is valid due to the fact that the checkerboards have the highest spatial variation and thereby highest spatial frequency. As a result, one could separate the zero-th order from the higher diffraction orders, which can be implemented by putting a pupil in the frequency space. If only the zero-th order ( $n = m = 0$ ) is selected, Eq. (2.11) becomes:

$$U'(x, y) = \frac{1}{2} \{ \exp(i\theta_1(x, y)) + \exp(i\theta_2(x, y)) \} = U(x, y) \quad (2.12)$$

where  $c_{1,2}^{00} = 1/2$  is computed. It is clearly seen that the filtered out zero-th order field  $U'(x, y)$  is exactly the summation of two phasors, and equal to the target complex amplitude function as defined in Eq. (2.7). Therefore, such DPH method is effective in encoding both amplitude and phase functions simultaneously in a phase-only SLM, with the spatial filtering in the Fourier domain.

The encoding scheme is also verified by simulation. For example, we target the amplitude and phase modulation as shown in Figure 2.3 b. Based on Eq. (2.9), we first calculate the required phase hologram that will be loaded to the SLM (Figure 2.3 c). Then we compute the Fourier

transform of the hologram, whose spectral power distribution is shown in Figure 2.3 d. We take only the center part of the Fourier image to implement the low pass filtering. The size of the spatial filter is indicated by the red circle. In the experiment, such filtering function can be carried out using an iris in the Fourier plane of a  $4-f$  system [105]. The amplitude and phase functions retrieved are in good agreement with the target ones (Figure 2.3 b).

**Pulse shaping.** SLMs not only enable the spatial shaping of light beams, but could also sculpt the optical field in time and frequency. Since the Fourier domain pulse shaping technique is an important concept involved in the thesis, the basic principle is briefly described here.

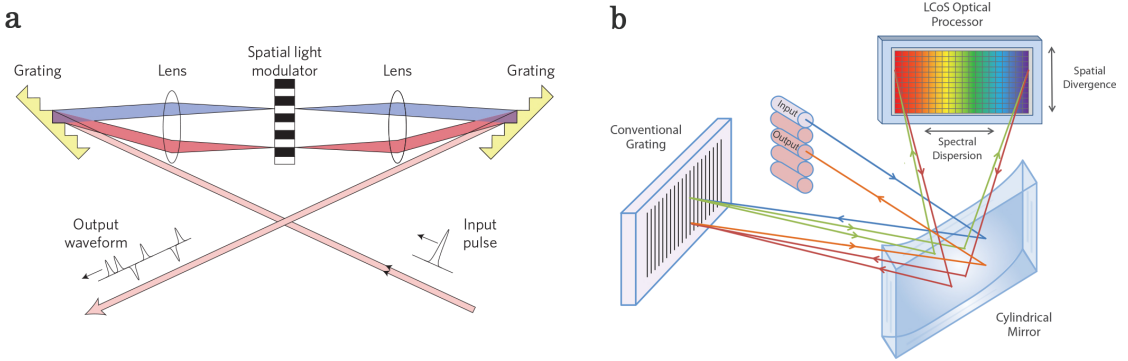


Figure 2.4 – Schematic setups of Fourier domain pulse shaping. (a) Classical  $4-f$  pulse shaper with gratings at the input and output planes, and spatial light modulator at the Fourier plane. Adapted from [106]. (b) Reflective-type pulse shaper with  $4-f$  configuration being folded. LCoS: liquid crystal on silicon. Adapted from Finisar Waveshaper product brochure.

Figure 2.4 a shows the typical setup of a Fourier domain pulse shaper [40, 106]. It is based on an optical  $4-f$  system with two identical gratings in its input plane and output plane, as well as an SLM in the Fourier plane. In this configuration, the setup is fully symmetrical, which consists of two gratings, two lenses, and a SLM. First, the frequency components of the input optical pulses are spatially dispersed by the grating. After the lens, these dispersed frequency components are made parallel, and being focused at the SLM plane. Each frequency component is then mapped to distinct position on the SLM, and can therefore be individually addressed by the SLM for both amplitude and phase modulation. The remaining part of the  $4-f$  setup does the reverse job to merge all these frequency components to one output beam. As a result, the output pulse waveform is controlled through the amplitude and phase shaping of its constituting frequency components. Noticeably, the  $4-f$  configuration can be intrinsically dispersion-less under proper alignment. Such  $4-f$  setup can also be folded, as shown in Figure 2.4 b, with a LCoS working in reflective manner. Such folded configuration benefits from using only half of the optical components (grating, lens, etc) as well as ease the optical alignment. Also as shown in Figure 2.4 b, when a cylindrical mirror is used, each frequency component of light is only focused in the horizontal axis but fully occupies the vertical axis. By applying phase ramps in the vertical direction, each frequency of light can be directed to different output position [41]. Given their usefulness in many applications, such Fourier domain pulse shapers are now commercially available.

### 2.3 The Talbot effect

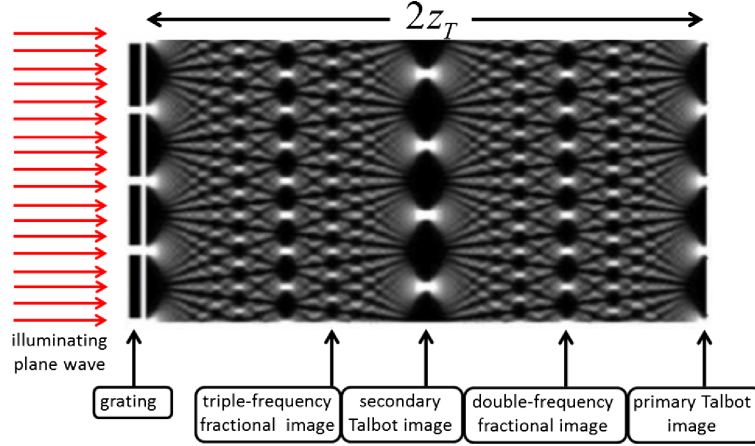


Figure 2.5 – Illustration of spatial Talbot effect. When a plane wave illuminates a periodic grating, the transmitted optical field is diffracted, and repetitively resembles itself along the propagation. The interference pattern is also known as the Talbot carpet.  $z_T$  is the Talbot length between the grating plane and the secondary Talbot image. Adapted from [107].

The Talbot effect is named after Henry Fox Talbot for the first observation in 1836 [108]. It describes unusual wave phenomena, which have been observed and used on a wide spectrum of waves, such as acoustics, plasmonics, electron beams, x-ray, in addition to optics [107]. In optics, the Talbot effect is most commonly explained in the context of spatial diffraction. As shown in Figure 2.5, when a monochromatic plane wave illuminates a periodic grating, the optical field after the grating repetitively resembles itself along the propagation in space. The elegant pattern in Figure 2.5 is also known as Talbot carpet. In addition to the Talbot image that exactly mimics the input image (primary Talbot image), more interesting patterns also appear at specific propagation distances, such as pattern with half period shift (secondary Talbot image), and fractional patterns with reduced period (double-, triple-frequency fractional images). This effect is a pure linear effect, which arises owing to the coherent interference of transverse wavevectors under Fresnel approximation. Such transverse wavevector components are exactly the Fourier series of the periodic grating function. Along the propagation, these lightwaves pick up quadratic phases due to the spatial diffraction. The multimode interference (MMI) coupler, one of the ubiquitous elements in the current photonic integrated circuitry, is also based on the spatial Talbot effect [109, 110]. It is a multi-input and multi-output device (generally  $2 \times 2$ ) that works as optical coupler. In a multimode waveguide, multiple eigenmodes of the waveguide excited at the input would interfere, and after certain length of propagation, they create self-images so as to equally split the optical power.

**Temporal Talbot effect.** Due to the space-time duality, similar spatial self-imaging phenomenon also arises in time, known as the temporal Talbot effect [52]. The multiple transverse wavevectors which constitute the periodic spatial images, are analogous to a series of frequency comb modes that make up the optical pulse trains, while the Fresnel diffraction in

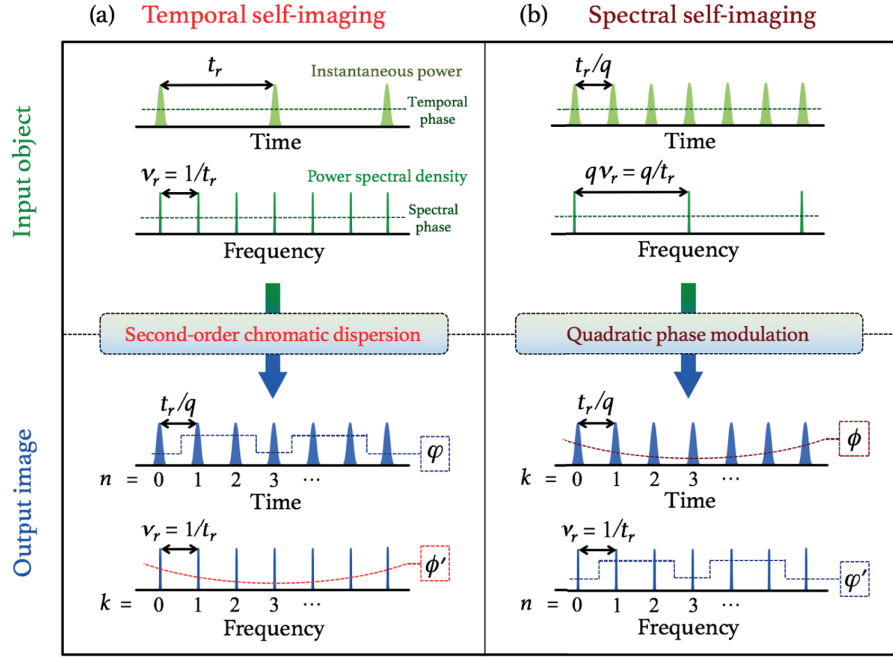


Figure 2.6 – Illustrations of temporal and spectral Talbot effects. (a) Temporal self-imaging is achieved by second-order chromatic dispersion of optical frequency combs. (b) Spectral self-imaging is achieved by quadratic phase modulation of optical pulses.  $t_r$  is the pulse period,  $\nu_r$  is the comb FSR, and  $q = 3$  is shown. The phases of optical pulses after temporal self-imaging, and the phases of frequency combs after spectral self-imaging, comply with the generalized Talbot relation. Adapted from [111].

space corresponds to the second-order dispersion in time. In the presence of dispersion, all these frequency comb modes would experience quadratic phases during propagation, therefore creating at specific positions the original or fractional self-images. The fractional self-imaging in time multiplies the repetition-rate of an optical pulse train. It is worth mentioning that the comb line spacing in the frequency domain remains unchanged, which is fundamentally different from increasing the comb FSR. The typical implementations require certain amount of second-order chromatic dispersion, like using a linearly chirped fiber Bragg grating (LCFBG) or a spool of optical fiber to realize the temporal Talbot effect [112]. Illustration of the temporal Talbot effect is shown in Figure 2.6 a.

**Spectral Talbot effect.** Spectral Talbot effect also exists given by the Fourier duality. Similar to temporal Talbot effect, the spectral version deals with frequency comb modes and optical pulse trains as well. As shown in Figure 2.6 b, when the initial optical pulse trains are under proper quadratic phase modulation, the comb FSR in the spectrum is correspondingly divided while the optical waveform intensity is preserved. Note this is also distinct from the pulse picking technique that realize comb FSR division by discarding part of the pulses periodically. The spectral self-imaging can be implemented in some nonlinear optical processes [113], or



can be inscribed in EOMs with the pre-determined multi-level EO phase modulation [57]. The loaded temporal phase patterns are the Talbot phases, which will be formulated in the following paragraph.

**Generalized Talbot effect.** Perhaps the most general Talbot phases are described as [58, 111, 114]:

$$\phi_k = \pi \frac{p}{q} k^2 \quad (2.13)$$

where  $p$  and  $q$  are mutually prime positive integers (the greatest common divisor (GCD) of  $p$  and  $q$  is 1), i.e.  $\gcd(p, q) = 1$  and  $p, q \in \mathbb{N}_+$ .  $k$  can be the index of the pulse (frequency mode) for spectral (temporal) Talbot effect.  $pz_T/q$  refers to the relative position at the Talbot carpet depicted in Figure 2.5. For instance, the triple-frequency image, secondary Talbot image, double-frequency image, and primary Talbot image in Figure 2.5 correspond to  $p/q = 2/3, 1/1, 3/2$ , and  $2/1$ , respectively. The applied Talbot phases could realize  $q$ -times self-images, with some of them showing additional half sub-period shift (the period of  $q$ -times self-images) with regards to the input image. More intriguingly, the phases of these self-images again satisfy the Talbot phase relations (neglecting the constant phase term), expressed as:

$$\phi_n = -\pi \frac{s}{q} n^2 \quad (2.14)$$

where  $n$  is the index of the self images and  $s \in \mathbb{N}_+$  defined by:

$$sp \equiv \begin{cases} 1 \pmod{2q}, & \text{if } q \equiv 0 \pmod{2} \\ 1+q \pmod{2q}, & \text{if } q \equiv 1 \pmod{2} \end{cases} \quad (2.15)$$

where  $s$  and  $q$  are also coprime and have opposite parity [111]. The mathematics behind these equations are related to the Gauss sum [115]. The phases of Talbot images have long been known from the phase relations of MMIs [110], but revived recently for the special interests in time-frequency signal processing [58, 59, 116, 117]. Such relation indicates that the temporal and spectral Talbot effects are closely linked to each other. That is to say, one could use two-step Talbot shaping to modify both the comb FSR and pulse period in a lossless manner [59]. The concatenation of phase modulation and dispersive propagation enables arbitrary repetition-rate multiplication of comb sources [59]. Similar two-step Talbot shaping has been adopted to generate optical square pulses, in temporal analog of Talbot array illuminators [117].

In this thesis work, we adopt one of the specific subset of the generalized Talbot phases [118], which will be detailed in Chapter 4.

## 2.4 Optical microresonator

Optical microresonators are resonant structures that confine light in small mode volumes, which have been used from optical sensing to quantum applications [119]. The properties of microresonators are also very well suited to use them as nonlinear optical devices, and have recently received tremendous attention [16]. Indeed, a plethora of material platforms and cavity geometries are being investigated for microcomb generation [120]. In this thesis, the microcombs are based on integrated  $\text{Si}_3\text{N}_4$  microresonators. We are particularly interested in the microcombs for applications in RF photonics. Since the thesis is not dedicated to microresonator nor microcomb generation, only the very basics relevant to the thesis work are discussed.

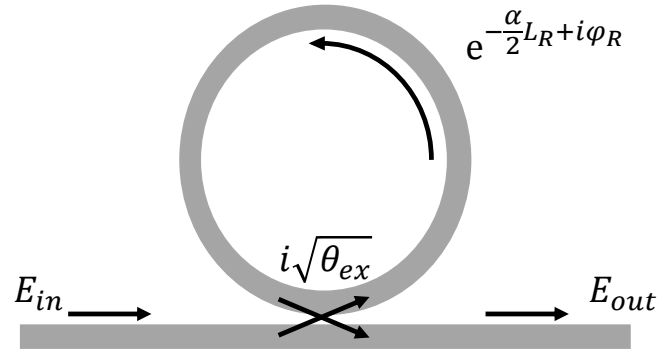


Figure 2.7 – Layout of the optical microresonator. The light is coupled from the bus waveguide to the ring resonator and collected at the bus waveguide.  $i\sqrt{\theta_{ex}}$ : cross coupling coefficient;  $L_R$ : roundtrip length;  $\alpha$ : loss per unit length;  $\phi_R$ : phase accumulated per roundtrip.

**Resonance characteristics.** First, we describe the universal linear properties of optical microresonators. As shown in Figure 2.7, a typical microresonator device is comprised of a closed-loop waveguide (mostly ring shape as depicted) being coupled to a bus waveguide via evanescent coupling. We consider that a monochromatic optical field  $E_{in}$  at angular frequency  $\omega_p$  is injected to the bus waveguide. When the gap between the bus waveguide and the ring is close enough, the spatial overlap of the evanescent fields in the bus waveguide and the ring would create a certain amount of cross coupling. We denote such power coupling strength per roundtrip as  $\theta_{ex}$ , so that for the optical field it becomes  $i\sqrt{\theta_{ex}}$  where  $i$  accounts for the  $90^\circ$  phase shift for the cross coupling. Owing to the energy conservation, the bar coupling is thus given by  $1 - \theta_{ex}$  for the power, and  $\sqrt{1 - \theta_{ex}}$  for the field. For the optical field being coupled to the ring, it travels the circumference of the ring before entering again the coupling region. The propagation of the optical field in the ring leads to a phase shift  $\phi_R = \omega_p n_{eff} L_R / c$  per roundtrip, but the field also gets attenuated by  $\exp(-\alpha L_R / 2)$  in amplitude due to the intrinsic loss.  $L_R$  denotes the round-trip length of the ring,  $n_{eff}$  is the effective refractive index and  $c$  is the speed of light.  $\alpha$  refers to the power loss per unit length in linear scale.

For the light that recirculated over one round trip in the ring, at the coupling region, partial light will stay inside the ring with bar coupling  $\sqrt{1-\theta_{ex}}$ , while the rest will be coupled back to the bus waveguide with the cross coupling  $i\sqrt{\theta_{ex}}$ . And this process repeats over and over again for the light that remains in the ring. In the bus waveguide, all of these optical waves output from different roundtrips would interfere with the initial bar coupled field. The circulating field  $E_{circ}$  and output field  $E_{out}$  can therefore be mathematically described as:

$$\begin{aligned} E_{circ} &= E_{in} i\sqrt{\theta_{ex}} \exp\left(-\frac{\alpha L}{2} + i\phi_R\right) \sum_{n=0}^{\infty} \left(\sqrt{1-\theta_{ex}} \exp\left(-\frac{\alpha L}{2} + i\phi_R\right)\right)^n \\ &= E_{in} \frac{i\sqrt{\theta_{ex}} \exp\left(-\frac{\alpha L}{2} + i\phi_R\right)}{1 - \sqrt{1-\theta_{ex}} \exp\left(-\frac{\alpha L}{2} + i\phi_R\right)} \end{aligned} \quad (2.16)$$

$$E_{out} = E_{in} \sqrt{1-\theta_{ex}} + i\sqrt{\theta_{ex}} E_{circ} = E_{in} \frac{\sqrt{1-\theta_{ex}} - \exp\left(-\frac{\alpha L}{2} + i\phi_R\right)}{1 - \sqrt{1-\theta_{ex}} \exp\left(-\frac{\alpha L}{2} + i\phi_R\right)} \quad (2.17)$$

where  $(n+1)$  refers to the number of roundtrip the light has circulated in the ring before it is coupled out. It can be clearly seen that, both Eq. (2.16) and Eq. (2.17) are periodic functions with period of  $f_{FSR} = cL_R/n_{eff}$  in the frequency domain. In the time domain, the roundtrip time is the inverse of the FSR, i.e.  $T_R = 1/f_{FSR}$ . Here we have assumed for the moment the microresonator is dispersion-less.

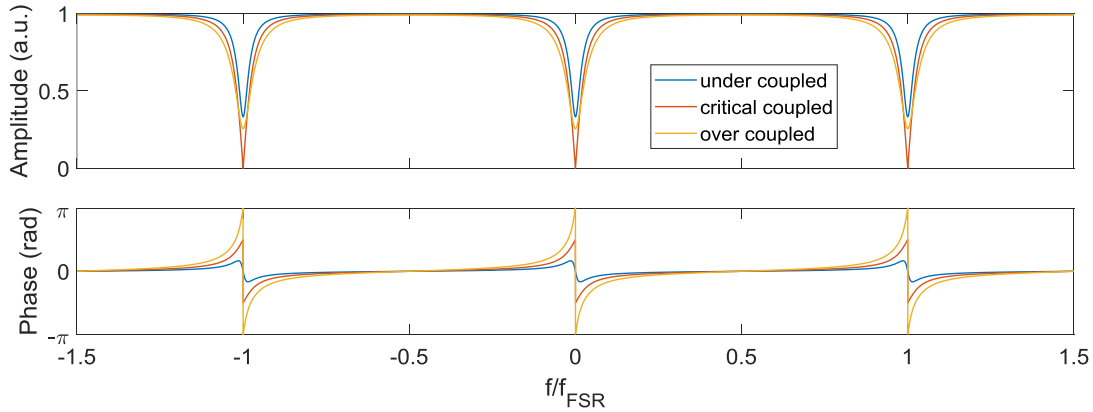


Figure 2.8 – Amplitude and phase responses of optical microresonator under three different regimes. Under-coupled regime:  $\theta_{ex} = 0.1$  (blue) ; critical-coupled regime:  $\theta_{ex} = 0.19$  (orange); over-coupled regime:  $\theta_{ex} = 0.3$  (yellow). The intrinsic loss term is  $\exp(-\alpha L/2) = 0.9$  for all cases. For critical- (under-, over-) coupling, the cross coupling  $\theta_{ex}$  is equal (smaller, larger) than the loss per roundtrip  $1 - \exp(-\alpha L)$ , or equivalently  $\kappa_0 = (>, <) \kappa_{ex}$ .

The transfer function  $H(f) = E_{out}/E_{in}$  of such linear device can be visualized as seen in Figure 2.8. As predicted, it is a periodic function demonstrating resonances in the spectrum. The lineshapes of these resonances can be inferred from the circulating optical field  $E_{circ}/E_{in}$ ,

which are expressed as:

$$\left| \frac{E_{circ}}{E_{in}} \right|^2 \sim \frac{1}{1 + \frac{4\sqrt{\rho}}{(1-\sqrt{\rho})^2} \sin^2 \frac{\phi_R}{2}} \quad (2.18)$$

where  $\rho = (1 - \theta_{ex}) \exp(-\alpha L)$  refers to the power transmitted from one roundtrip to the next. Therefore, we can find the linewidth of the resonance  $\kappa$  by:

$$\frac{\kappa}{2\pi f_{FSR}} = \frac{\Delta\phi_{R,3dB}}{2\pi} = \frac{4 \arcsin\left(\sqrt{\frac{(1-\sqrt{\rho})^2}{4\sqrt{\rho}}}\right)}{2\pi} \approx \frac{1-\rho}{2\pi} \quad (2.19)$$

The third equality holds for small roundtrip loss ( $\rho$  is close to 1). Eq. (2.19) gives the full-width-half-maximum (FWHM) of the resonance  $\kappa$  in the angular frequency as  $\kappa \approx (1 - \rho)/T_R$ . On the other hand, this can be viewed as the total power loss rate of the microresonator. We could also found separately the loss rates induced by the propagation and coupling, as  $\kappa_0 = \alpha L/T_R$  and  $\kappa_{ex} \approx \theta_{ex}/T_R$  ( $\theta_{ex} \ll 1$  assumed), respectively. And both these loss channels constitute the total loss, i.e.  $\kappa = \kappa_0 + \kappa_{ex}$ . This could also be verified from  $\kappa \approx (1 - \rho)/T_R = (1 - (1 - \theta_{ex}) \exp(-\alpha L))/T_R \approx (1 - (1 - \kappa_0 T_R)(1 - \kappa_{ex} T_R))/T_R \approx \kappa_0 + \kappa_{ex}$ . The quality factor of microresonator can be defined as the ratio of the optical angular frequency  $\omega$  and the loss rate of microresonator, i.e.  $Q = \omega/\kappa$  for loaded  $Q$  and  $Q_0 = \omega/\kappa_0$  for intrinsic  $Q$ .

**Coupling regime.** Three distinct coupling regimes are observed depending on the relation between the cross coupling strength and the loss per roundtrip. When they are equal ( $\kappa_0 = \kappa_{ex}$ ), at resonances, all of the light from the bus waveguide could be coupled to the ring resonator (orange curves in Figure 2.8). This is due to the fact that the bar-coupled optical field is exactly equal in amplitudes, but out-of-phase with all the recirculating fields from the ring. Such operation regime is denoted as critical coupling.

Other than this operation status, the light from the bus waveguide can only be partially coupled to the ring. When the intrinsic loss rate is greater than the coupling strength ( $\kappa_0 > \kappa_{ex}$ ), it is known as the under coupling (blue curves in Figure 2.8). In this case, the total linewidth  $\kappa$  is smaller compared to critical coupling regime, when we consider both cases possess the same intrinsic loss rate. The phase response of the under-coupled regime also indicates it provides roughly  $0^\circ$  phase change across the resonance frequency. Such under-coupled condition can be experimentally realized by a large gap between the bus waveguide and ring resonator, or mismatching the geometries between the bus and ring waveguides.

On the other hand, over coupling refers to the condition when the intrinsic loss rate is smaller than the coupling strength ( $\kappa_0 < \kappa_{ex}$ , yellow curves in Figure 2.8). The total linewidth is larger than the critical-coupled regime in this scenario. Interesting features are observed in the phase response of the over-coupled regime. It shows a  $2\pi$  phase shift across the resonance frequency. Moreover, the phase response exhibits an exact  $\pi$  phase inversion exactly at the resonance frequency. Such phase relation of over-coupled rings can be harnessed for some

advanced RF photonic filtering purposes [91]. Likewise, over coupling regime is generally reached by placing the bus waveguide closer to the ring resonator than for critical coupling.

**Dispersion.** Up to now, the discussion above has assumed the microresonators to be dispersionless, so that all resonances are equally-spaced. It may be approximated like this for a narrow bandwidth, the resonances would however deviate from such idealized equidistant grid for a broad bandwidth coverage. Let us recall the resonant condition for the microresonator:

$$\phi_R = \frac{\omega_m n_{eff}(\omega_m) L_R}{c} = 2\pi m \quad (2.20)$$

where  $m \in \mathbb{N}_+$ , which can be interpreted as the number of wavelengths encompassed in the ring resonator. It is noted that the effective refractive index is a function of the frequency, causing the resonances to deviate from an equidistant grid. We could study such non-uniformity of the resonances through the Taylor expansion of the resonant frequencies:

$$\omega_\mu = \omega_0 + \sum_{n=1}^{\infty} \frac{D_n}{n!} \mu^n = \omega_0 + D_1 \mu + \frac{D_2}{2!} \mu^2 + \frac{D_3}{3!} \mu^3 + \dots \quad (2.21)$$

The above equation is expanded with respect to a certain resonant frequency  $\omega_0$ .  $\mu = m - m_0 \in \mathbb{Z}$  is the relative mode index, where  $m_0$  is the corresponding mode index of  $\omega_0$ .  $D_n = \frac{\partial^n \omega_\mu}{\partial \mu^n}$  are the coefficients of the Taylor series.  $D_1$  represents the uniform spacing between adjacent resonances, thereby  $D_1 = 2\pi f_{FSR}$  which is linked to the local cavity FSR. While  $D_n (n \geq 2)$  accounts for the deviation from the equidistant distribution. Specifically, the physical meaning of  $D_2$  refers to the quadratic dependence of the resonance deviation. It is related to the group velocity dispersion  $\beta_2$  and the inverse group velocity  $\beta_1$ , which can be derived as  $D_2 = -D_1^2 \beta_2 / \beta_1$ . The sign of  $D_2$  denotes the dispersion of the microresonator, with anomalous dispersion ( $D_2 > 0$ ) and normal dispersion ( $D_2 < 0$ ). The integrated dispersion is defined as  $D_{int}(\mu) = \omega_\mu - (\omega_0 + D_1 \mu)$ , which represents the overall resonance walk-off from the equidistant grids. In addition to the second-order dispersion  $D_2$ , higher-order dispersion or avoided mode crossings could also be important contributions to the integrated dispersion. The integrated dispersion must be nonzero for microcomb generation [121].

**Avoided mode crossing.** The avoided mode crossings (AMX) are the local resonance frequency deviations that resulted from the coupling between the current mode and the other mode families. Generally, the microresonators used for microcomb generation support multiple spatial modes. Due to the distinct spatial distributions, these modes typically have unequal effective refractive indices with different frequency dependence, thereby giving different FSRs and integrated dispersion profiles. While the mismatch in FSR will lead to the resonances of two mode families crossing in frequency. Ideally, although being coincided in spectrum, the resonance frequencies of different mode families are unaffected by such crossover, as the modes are eigensolutions and thus orthogonal to each other. However, in practice, any defect of the microresonator could induce the coupling between the two mode families. And such coupling will give rise to the formation of new hybridized modes, so that their local dispersion

profiles are significantly modified [122, 123].

**Microcomb generation.** Following the description of the linear properties of microresonators, I will give a very basic overview of Kerr comb generation in microresonators. The low-loss and small mode volume of microresonators as well as their resonant nature have made them perfect devices for nonlinear optics. There are many platforms that have been used for microcomb generation from dielectric to conducting materials, such as the metal fluoride where the soliton was first observed [124], silicon nitride that is CMOS-compatible [125], and lithium niobate that exhibits both Pockels and Kerr effects [126]. The nonlinear refractive index of  $\text{Si}_3\text{N}_4$  is around  $2.4 \times 10^{-19} \text{ m}^2/\text{W}$ , which is far from the highest among all the platforms. However, the recent fabrication improvement of  $\text{Si}_3\text{N}_4$  has resulted in extremely low loss enabling microcomb excitation with mW pump power [17]. Moreover, the dispersion of integrated microresonator can be engineered by tailoring the cross-section of the waveguide. Together with the wide transparency window from the visible to the mid-infrared, the absence of two-photon absorption in the telecom-band, and the potential for mass production,  $\text{Si}_3\text{N}_4$  has become one of the most suitable platform for microcomb generation, and in general for linear and nonlinear optical processes.  $\text{Si}_3\text{N}_4$  does not naturally exhibit second-order nonlinearity  $\chi^{(2)}$ , but may be triggered by optical poling via the formation of self-organized grating structures [127]. Here we treat  $\text{Si}_3\text{N}_4$  only as a third-order nonlinearity  $\chi^{(3)}$  medium.

Microcombs are equidistant optical frequency combs generated in miniaturized microresonators, which rely on the Kerr nonlinearity to produce new frequencies. Modulational instability (MI) is the prerequisite for comb initiation. As the first step for microcomb generation, hyperparametric oscillation in optical microresonator was first observed around 15 years ago [128]. The comb spectrum is typically widely spaced by multiple FSRs also known as primary combs. In the time domain, it corresponds to stable waveforms known as Turing patterns or Turing rolls. Beyond the primary combs, broadband optical frequency combs have then followed [44, 129–131]. All of these pioneer works as well as the generation of temporal cavity solitons in fiber cavities [132], eventually led to the observation of dissipative Kerr solitons in crystalline microresonators [124, 133] and then in integrated microresonators [125]. After that, the research on microcombs has flourished as a very active field, from the fundamental understanding of the dynamics [121] towards various applications of the microcombs [28].

There are basically two types of mode-locked microcombs depending on the dispersion regimes they operated at [121]. As mentioned earlier, the existence of the MI gain is the first step for comb generation. It is well known that the MI arises under anomalous group velocity dispersion for single-pass structures, and similar condition applies to the resonant microresonators. Indeed, dissipative Kerr solitons exist in anomalous dispersion regime, analogous to the general operation of solitons that require the anomalous dispersion to counteract the self-phase modulation (SPM) effect. Figure 2.9 a showcases the spectrum and temporal waveform of a dissipative Kerr soliton obtained in a magnesium fluoride microresonator [124]. The spectrum exhibits the typical  $\text{sech}^2$  shape of soliton, together with a strong CW pump line. This manifests low conversion efficiency due to the poor overlap between the soliton and the

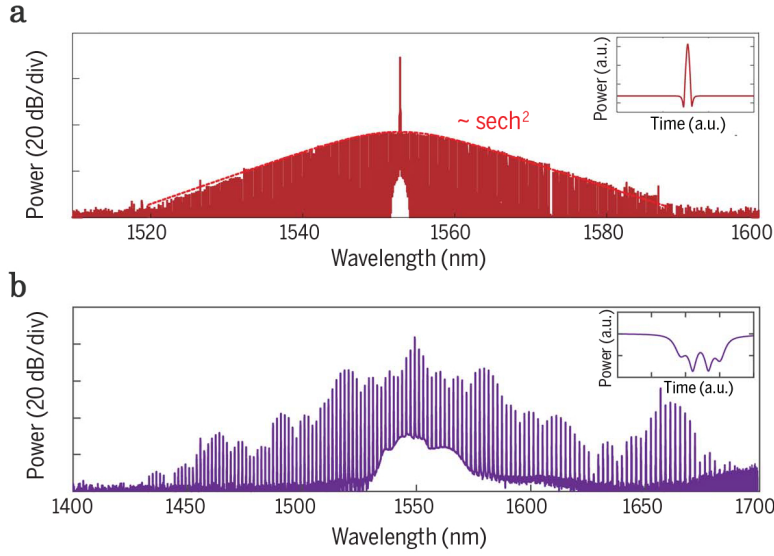


Figure 2.9 – Examples of microcomb generation in the anomalous and normal dispersion regimes. The insets show the temporal waveforms of the microcombs. (a) Dissipative Kerr soliton generation in anomalous dispersion regime, with solitons seated at the CW background. (b) Dark pulse generation in anomalous dispersion regime, with dark pulses formed in the time domain. Adapted from [16] with (a) originally from [124] and (b) originally from [134].

pump, which may be improved by pumping microresonators with optical pulse sources [135]. In the time domain, dissipative Kerr solitons correspond to short pulses seating on top of the CW background of the pump.

While less intuitive, mode-locked comb states also exist for normal dispersion microresonators. They correspond to the so-called dark pulses or platons [136]. In the context of normal dispersion, although MI is predicted to appear in the resonators [121], it is very difficult to access the region experimentally using conventional excitation methods. In the experiment, MI in normal dispersion microresonator generally arises due to the AMX effect, which locally modifies the integrated dispersion for some resonances [122]. The formation of dark pulses is recently explained being linked to interlocked switching waves between the upper and lower homogeneous states [137]. As shown in Figure 2.9 b, the microcomb generated in a normal dispersion  $\text{Si}_3\text{N}_4$  microresonator shows dark pulses in the time domain with complex temporal structures [134]. The spectrum of dark pulse microcomb features very high conversion efficiency from the pump to the comb lines, but typically requires additional pulse shaping for target applications due to its rugged spectrum.

**Lugiato-Lefever equation.** The formation of Kerr combs in optical microresonators is most generally described by coupled mode equations [138], Ikeda map [139], or the Lugiato-Lefever equation (LLE) [140]. Unlike Ikeda map which emulates the field as it propagates, the LLE is based on mean-field approximation to speed up simulation. That is, the LLE assumes the field to be slowly varying within the roundtrip time, which is valid for the scenario of microcomb

generation. Mean-field LLE describes a damped, driven, detuned microresonator as [141]:

$$\frac{\partial A}{\partial t} = \left( -\left(\frac{\kappa}{2} + i\delta\omega\right) + i\frac{D_2}{2}\frac{\partial^2}{\partial\Phi^2} + ig|A|^2 \right)A + \sqrt{\kappa_{ex}}s_{in} \quad (2.22)$$

where  $A(\Phi, t)$  is the temporal envelope of the intracavity field, and is normalized such that  $|A|^2$  corresponds to the intracavity photon number.  $t$  is the 'slow time' linked to the number of the roundtrips light circulated. While  $\Phi$  is the 'fast time' quantity that represents the location of the envelope function in the angular coordinate of the resonator.  $\kappa$  is the total power loss rate as described before.  $\delta\omega = \omega_0 - \omega_p$  is the detuning between the resonance frequency and pump frequency.  $\frac{D_2}{2}\frac{\partial^2}{\partial\Phi^2}$  is the second-order dispersion operator. Here the LLE is moving at the frame of the group velocity of the envelope, and higher-order dispersion is omitted.  $g$  is the Kerr frequency shift per photon, defined as  $g = \hbar\omega_0^2cn^2/n_0^2V_{eff}$ , where  $n_0$  is the effective group refractive index,  $n_2$  is the nonlinear refractive index, and  $V_{eff}$  is the effective mode volume. The term  $g|A|^2$  accounts for the SPM.  $\sqrt{\kappa_{ex}}s_{in}$  represents the external driving term, where  $|s_{in}|^2$  denotes the pump power.

As in the simulation of the nonlinear Schrödinger equation (NLSE) [142], the LLE can also be numerically solved using split-step method. In Eq. (2.22), the dispersion term is generally computed in the frequency domain, while the SPM term is computed in the time domain. Thanks to the efficient fast Fourier transform computation, the repeated Fourier transforms required by this method can be efficiently implemented. In this thesis, the LLE subjected to additional AMX is simulated in Chapter 5 to understand the binding effect of two solitons.

## 2.5 Conclusions

In this chapter, the general principles related to the thesis study are described, providing the guidelines for the following chapters. First, the working principles of EOMs lay the foundations for optical sinc pulse generation and EO modulation. Second, the basis of SLMs are described, with the emphasis on spatial light shaping and Fourier domain pulse shaping. Then various representations of the Talbot effect in space, time, and frequency are introduced, and are generalized with the concept of the Talbot phases. Finally, the basic properties of optical microresonators and microcomb generation are briefly discussed.





## 3 Generation and applications of optical sinc pulses

The content in this chapter is based on the following publications:

- **J. Hu**, S. J. Fabbri, and C.-S. Brès, "Flexible Width Nyquist Pulse Based on a Single Mach-Zehnder Modulator, " in Conference on Lasers and Electro-Optics (CLEO), SF3N.6 (2018). [143]
- **J. Hu**, S. J. Fabbri, and C.-S. Brès, "Reconfigurable Filter-free Sinc-shaped RF Photonic Filters Based on Rectangular Optical Frequency Comb," in Conference on Lasers and Electro-Optics (CLEO), SM1C.1 (2018). [144]
- **J. Hu**, S. Kharitonov, S. J. Fabbri, and C.-S. Brès, "Add-Drop Multiplexing Architecture for Nyquist OTDM Signals Based on a Single Mach-Zehnder Modulator," in Asia Communications and Photonics Conference (ACP), M4A.38 (2019). [145]

### 3.1 Introduction

Optical sinc pulses have been used for a wide range of photonics-related applications. Due to their rectangular spectral shape and zero inter-symbol interference (ISI) in time domain, they have been used in Nyquist OTDM systems [64] to achieve high spectral efficiency as comparable to OFDM systems. In this case, sinc pulses, or more generally Nyquist pulses, would serve as the carriers for data symbols. They are aggregated in time to form an optical superchannel. For the implementation of high-speed Nyquist OTDM systems, the optical generation of sinc pulses is favored in order to supplant the limited electronic bandwidth [146]. As a consequence, simple and effective synthesis of sinc pulses has been actively pursued.

Moreover, the sinc pulses may not only be needed in the transmitter, but also in the receiver side to demultiplex the Nyquist OTDM signals via matched sampling [68]. While for optical networks, in addition to demultiplexing a specific subcarrier, the ability to replace such subcarrier with a new data stream is essential. However, no such scheme exists for Nyquist OTDM systems, as have been envisioned or demonstrated for many other advanced multiplexing techniques [70, 147, 148].

Further, the frequency comb nature of sinc pulses is also appealing to use them for comb-based RF photonic filters [80]. For this specific application, the requirement of the optical source is much relaxed, as no linear phase relation among the comb lines is needed (even the laser lines can be incoherent). The rectangular spectra of sinc pulses would impart the RF filters with sinc response, which may be potentially used for the demultiplexing of RF OFDM signals.

In this chapter, I will present the main results regarding the generation of optical sinc pulses, as well as their usages in RF photonics and optical communications. Section 3.2 briefly discusses the mathematical foundation of sinc pulses. Section 3.3 demonstrates a flexible sinc pulse generation scheme based on a single MZM driven by multi-harmonic RF signals. Section 3.4 synthesizes RF photonic filters with sinc-shaped responses based on rectangular frequency combs. Section 3.5 provides time-domain reconfigurable optical add-drop multiplexing architectures for Nyquist OTDM signals.

### 3.2 Properties of sinc pulses

A sinc pulse is a special case of a more general pulse category, named Nyquist pulse or raised-cosine pulse, which is defined as [149]:

$$r(t) = \frac{\sin(\pi t/T_s)}{\pi t/T_s} \frac{\cos(\alpha \pi t/T_s)}{1 - (2\alpha t/T_s)^2} \quad (3.1)$$

where  $T_s$  is half of the pulse duration between the zero crossings, and  $\alpha$  is the roll-off factor falling in the range  $0 \leq \alpha \leq 1$ . As can be seen from Eq. (3.1),  $r(mT_s) = 0$  for  $m \in \mathbb{Z}_{\neq 0}$ . That means the Nyquist pulse is free from ISI with its  $T_s$ -spaced time translates. When being multiplexed, although the Nyquist pulses are temporally overlapped, they can be unambiguously sampled at these zero-crossing points.  $T_s$  also represents the symbol period in this case. As a result, Nyquist pulses can be more densely packed in time compared to Gaussian pulses. The spectrum of Nyquist pulse is given by:

$$\tilde{R}(f) = \begin{cases} T_s, & \text{if } |f| \leq \frac{1-\alpha}{2T_s} \\ \frac{T_s}{2} \left\{ 1 + \cos\left(\frac{\pi T_s}{\alpha} \left(|f| - \frac{1-\alpha}{2T_s}\right)\right) \right\}, & \text{if } \frac{1-\alpha}{2T_s} \leq |f| \leq \frac{1+\alpha}{2T_s} \\ 0, & \text{otherwise} \end{cases} \quad (3.2)$$

It is obvious from Eq. (3.2) that the bandwidth occupancy of a Nyquist pulse increases with the roll-off factor  $\alpha$ . The minimum bandwidth is achieved when  $\alpha = 0$ , and the spectrum becomes rectangular with the temporal waveform being sinc-shaped. The sinc pulse is orthogonal to its  $T_s$ -spaced time translates (usually not the case for  $\alpha > 0$ ), and is therefore of particular interest among the family of Nyquist pulses. According to Parseval's theorem, this is equivalent to

prove the orthogonality in frequency domain:

$$\begin{aligned} & \int_{-\infty}^{\infty} \frac{\sin(\pi(t - mT_s)/T_s)}{\pi(t - mT_s)/T_s} \frac{\sin(\pi(t - nT_s)/T_s)}{\pi(t - nT_s)/T_s} dt \\ &= \int_{-\frac{1}{2T_s}}^{\frac{1}{2T_s}} \exp(-i2\pi f m T_s) T_s \exp(-i2\pi f n T_s) T_s df = T_s \delta_{mn} \end{aligned} \quad (3.3)$$

where  $m, n \in \mathbb{Z}$  and  $\delta_{mn}$  is the Kronecker delta function ( $\delta_{mn} = 1$  if  $m = n$ , otherwise  $\delta_{mn} = 0$ ). In Eq. (3.3), we also utilize the Fourier transform property stating that the delay in time domain corresponds to a phase shift in frequency. The orthogonality of sinc pulses implies that the symbols modulated on sinc pulses can be more easily retrieved with sinc pulse sampling, instead of using a very short pulse (Dirac function).

In practice, generally, periodic sinc pulses are synthesized rather than producing an isolated single sinc pulse. As mentioned earlier, frequency combs with comb lines having equal amplitudes and linear spectral phases correspond to a sequence of sinc pulses in time domain. The mathematical derivation is explained as follows. For simplicity, frequency combs with odd number of lines  $N$ , centered at frequency  $f_0$  and spaced by  $\Delta f$ , as well as zero initial phases for all frequency components are assumed. The time domain representation of the optical field is thus given by:

$$\begin{aligned} E(t) &= \frac{E_0}{N} \sum_{k=-\frac{N-1}{2}}^{\frac{N-1}{2}} \exp(i2\pi(f_0 + k\Delta f)t) = \frac{E_0}{N} \exp(i2\pi f_0 t - i\pi(N-1)\Delta f t) \frac{1 - \exp(i2\pi N\Delta f t)}{1 - \exp(i2\pi \Delta f t)} \\ &= \frac{E_0}{N} \frac{\sin(\pi N\Delta f t)}{\sin(\pi \Delta f t)} \exp(i2\pi f_0 t) \end{aligned} \quad (3.4)$$

where  $\frac{\sin(\pi N\Delta f t)}{N \sin(\pi \Delta f t)}$  corresponds to the normalized envelope of the optical field. It actually corresponds to a sequence of sinc pulses, which can be analyzed in the frequency domain by Fourier transform:

$$\begin{aligned} F\left\{\frac{\sin(\pi N\Delta f t)}{N \sin(\pi \Delta f t)}\right\} &= F\left\{\frac{1}{N} \sum_{k=-\frac{N-1}{2}}^{\frac{N-1}{2}} \exp(i2\pi k\Delta f t)\right\} = \frac{1}{N} \sum_{k=-\frac{N-1}{2}}^{\frac{N-1}{2}} \delta(f - k\Delta f) \\ &= \frac{1}{N} \Pi_{N\Delta f}(f) \sum_{k=-\frac{N-1}{2}}^{\frac{N-1}{2}} \delta(f - k\Delta f) \end{aligned} \quad (3.5)$$

where  $F\{\}$  represents the Fourier transform.  $\Pi_{N\Delta f}(f)$  is a rectangular function defined as:

$$\Pi_{N\Delta f}(f) = \begin{cases} 1, & \text{if } |f| \leq \frac{N\Delta f}{2} \\ 0, & \text{otherwise} \end{cases} \quad (3.6)$$

Owing to the convolution theorem, the envelop function can be expressed as:

$$\begin{aligned} \frac{\sin(\pi N \Delta f t)}{N \sin(\pi \Delta f t)} &= \frac{1}{N} F^{-1}\{II_{N \Delta f}(f)\} \otimes F^{-1}\left\{\sum_{k=-\frac{N-1}{2}}^{\frac{N-1}{2}} \delta(f - k \Delta f)\right\} \\ &= \frac{1}{N} \frac{\sin(\pi N \Delta f t)}{\pi t} \otimes \frac{1}{\Delta f} \sum_{k=-\infty}^{\infty} \delta\left(t - \frac{k}{\Delta f}\right) = \sum_{k=-\infty}^{\infty} \frac{\sin\left(\pi N \Delta f\left(t - \frac{k}{\Delta f}\right)\right)}{\pi N \Delta f\left(t - \frac{k}{\Delta f}\right)} \end{aligned} \quad (3.7)$$

where  $F^{-1}\{\}$  is the inverse Fourier transform and  $\otimes$  represents the convolution operation. Similarly, the optical field in the case of even number of comb lines can be derived:

$$\frac{\sin(\pi N \Delta f t)}{N \sin(\pi \Delta f t)} = \sum_{k=-\infty}^{\infty} (-1)^k \frac{\sin\left(\pi N \Delta f\left(t - \frac{k}{\Delta f}\right)\right)}{\pi N \Delta f\left(t - \frac{k}{\Delta f}\right)} \quad (3.8)$$

From Eq. (3.7) and (3.8), we have confirmed that a series of comb lines with equal-amplitudes and linear phases indeed correspond to sinc pulses in time. The period of the sinc pulse train is the inverse of the comb FSR, i.e.  $T = 1/\Delta f$ . The symbol period  $T_s$ , which is also half of the zero crossings of the main peak, is found to be  $T_s = 1/N\Delta f$ . Although the expressions of optical fields are different for odd and even number of comb lines, their intensity expressions are unified:

$$I(t) = |E(t)|^2 = E_0^2 \frac{\sin^2(\pi N \Delta f t)}{N^2 \sin^2(\pi \Delta f t)} = E_0^2 \sum_{k=-\infty}^{\infty} \frac{\sin^2(\pi N \Delta f(t - kT))}{(\pi N \Delta f(t - kT))^2} \quad (3.9)$$

where Eq. (3.9) uses the orthogonality of sinc pulses described in Eq. (3.3). The frequency and time domain representations of sinc pulses are shown in Figure 3.1.

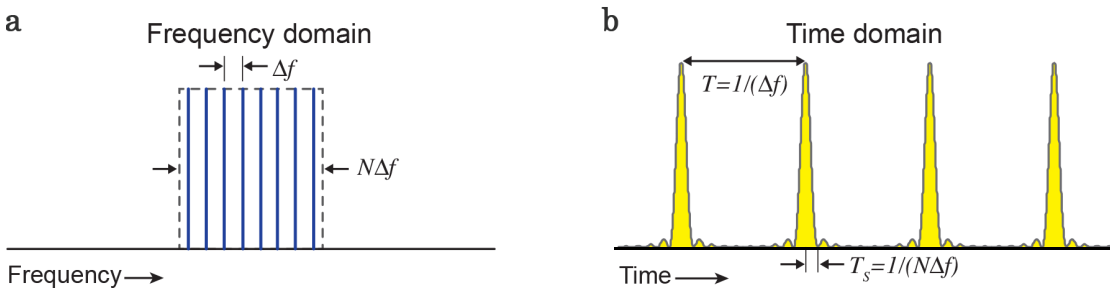


Figure 3.1 – Frequency and time representations of periodic sinc pulses. (a) In the frequency domain, sinc pulses correspond to a series of equal amplitudes, linear phases frequency comb lines.  $\Delta f$ : comb FSR;  $N$ : number of comb lines. (b) In the time domain, the intensity of sinc pulses is shown.  $T$ : pulse period;  $T_s$ : the symbol period, or equivalently half of the zero-crossings between the main peak. Adapted from [65].

### 3.3 Flexible optical sinc pulse generator

Optical sinc pulses can be obtained through the general optical arbitrary waveform generation techniques [106]. By manipulation of the amplitudes and phases of frequency combs in a pulse shaper, the temporal waveforms can be shaped to sinc pulses. Besides the external shaping of existing frequency combs, pulse shaper may also be used inside an active mode-locked laser cavity to tailor the spectrum, thereby directly outputting the target sinc pulses [149].

There are also schemes generating sinc pulses without involving pulse shapers. As described in Section 2.1, sinc pulses with 5 spectral comb lines can be obtained based on DP-MZM [89]. Besides, sinc pulses with 9 spectral lines can be produced based on two cascaded MZMs driven by two synchronized RF frequencies [63]. Although other methods could generate Nyquist pulses with flexible or more number of spectral lines, for instance the demonstrations based on dual-drive MZM [67], or times lens (PM) [150, 151], they do not correspond to sinc pulses with zero roll-off factors. Since the number of comb lines constituting the sinc pulses also determines the number of channels that can be aggregated in time, flexibility of comb lines is desired as to reconfigure the Nyquist OTDM systems.

**Principle of flexible optical sinc pulse generator.** Here we propose an alternative simple method for generating sinc pulses based on a single MZM. Synchronized multi-harmonic RF signals are electrically combined to drive the MZM. Such scheme could realize sinc pulses with arbitrary number of lines below  $2N + 1$  using  $N$  RF sinusoidal signals. In the experiment, we showcase sinc pulse generation with 4 to 9 comb lines based on 2 to 4 synchronized RF signals. The use of multi-harmonic RF signals provides the precise amplitude and phase control of each pair of sidebands. Hence, the perfect flatness and linear phase relation of the optical combs can be achieved, alongside with the high side mode suppression ratio (SMSR) in the spectrum. Recalling the operating principle of the MZM, when it is driven by  $N$  RF sinusoidal waves, the MZM output is formulated as:

$$\begin{aligned} E(t) &= E_0 \cos(\psi + \sum_{k=1}^N \beta_k \cos \omega_k t) \exp(i\omega_0 t) \\ &= E_0 \left\{ \cos \psi \cos \left( \sum_{k=1}^N \beta_k \cos \omega_k t \right) - \sin \psi \sin \left( \sum_{k=1}^N \beta_k \cos \omega_k t \right) \right\} \exp(i\omega_0 t) \end{aligned} \quad (3.10)$$

where  $\psi = V_{DC}/2V_{\pi,DC}$  is the normalized bias,  $\beta_k = V_k/2V_{\pi,\omega_k}$  are the modulation indices for RF sinusoidal waves at angular frequencies  $\omega_k$ , ( $k = 1, \dots, N$ ). By keeping  $\beta_k$  of each RF component identical and small ( $\beta = \beta_1 = \dots = \beta_N \ll 1$ ), as well as setting the multi-harmonic RF signal as  $\omega_k = k\Delta f$ , ( $k = 1, \dots, N$ ), Eq. (3.10) can be approximated by:

$$E(t) \approx E_0 \left\{ \cos \psi - \frac{\beta \sin \psi}{2} \sum_{k=1}^N (\exp(-ik\Delta f t) + \exp(ik\Delta f t)) \right\} \exp(i\omega_0 t) \quad (3.11)$$

In order to obtain equal amplitude and in-phase relation of all optical frequency components,  $\cos \psi = -\beta \sin \psi / 2$  has to be satisfied here. Therefore, sinc pulses of  $2N + 1$  comb lines with

comb FSR  $\Delta f$  are generated, based on  $N$  synchronized RF tones. Note that since the modulation index is small, the bias point is close to the minimum transmission point (MITP) of the MZM.

Similarly, sinc pulses with even number of comb lines can also be synthesized using multi-harmonic approach. Still by keeping the modulation indices  $\beta = \beta_1 = \dots = \beta_N \ll 1$ , when the MZM is driven with RF frequencies of  $\omega_k = (k - 1/2)\Delta f$ , ( $k = 1, \dots, N$ ) and biased at MITP ( $\psi = \pi/2$ ), the output optical field is approximated as:

$$E(t) \approx -E_0 \frac{\beta}{2} \sum_{k=1}^N \left\{ \exp\left(-i\left(k - \frac{1}{2}\right)\Delta f t\right) + \exp\left(i\left(k - \frac{1}{2}\right)\Delta f t\right) \right\} \exp(i\omega_0 t) \quad (3.12)$$

where  $2N$  comb lines satisfying sinc pulse condition are also generated. Noticeably, the input optical carrier is completely notched in this case. To sum up, sinc pulses with up to  $2N + 1$  lines can be obtained when the MZM is driven by  $N$  multi-harmonic RF signals.

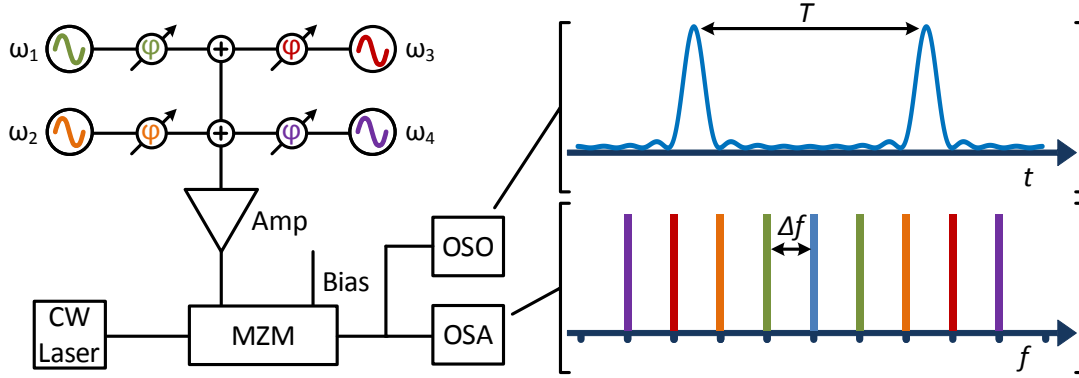


Figure 3.2 – Schematic setup of flexible sinc pulse generator. A CW laser is injected to the MZM driven by a number of synchronized RF sinusoidal waves. OSO: optical sampling oscilloscope; OSA: optical spectrum analyzer;  $\varphi$ : tunable phase shifter; Amp: electrical amplifier. The MZM output is directed to the OSO and OSA for measurement, where the intensity waveform and spectrum of sinc pulses with 9 comb lines are shown.

**Experimental results.** The schematic setup of the flexible sinc pulse generator is depicted in Figure 3.2. A CW laser is directed to a 40 GHz low  $V_\pi$  MZM driven by multiple synchronized RF signals. The modulator output is then split equally for simultaneous waveform and spectrum measurements, using an optical sampling oscilloscope (OSO) and an optical spectrum analyzer, respectively. Due to the low sensitivity of the OSO, the optical signal is amplified by an erbium-doped fiber amplifier (EDFA), and the amplified spontaneous noise (ASE) is filtered before the OSO. The electrical part of the setup consists of four synchronized RF clock sources of various frequencies, RF broadband amplifiers, RF power combiners, and electrical delay lines as phase controllers. Alternatively, a single clock source can be used followed by a bank of RF frequency multipliers [152]. In the experiment, we target sinc pulses with standard 10 GHz comb FSR. For sinc pulses with 5, 7, 9 lines, 2 to 4 RF frequencies are used with 10 GHz

fundamental frequency and its harmonics, i.e. 20 GHz, 30 GHz, and 40 GHz. While for sinc pulses with 4, 6, 8 lines, 2 to 4 RF frequencies are set to 5 GHz, 15 GHz, 25 GHz, and 35 GHz. The relative phases of these RF components are fully tunable either from the clock sources directly or by inserting electrical phase shifters in the paths.

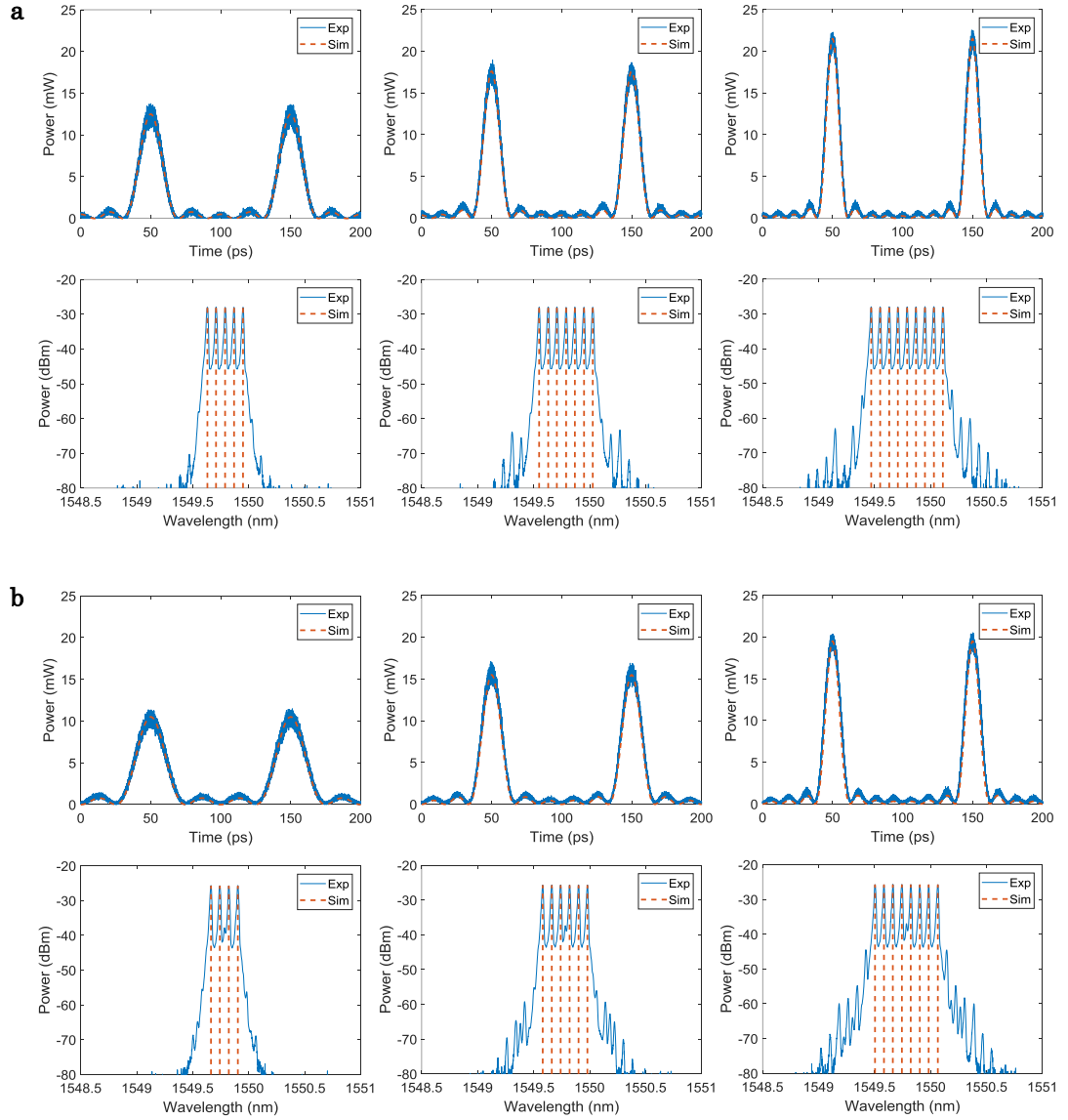


Figure 3.3 – Waveforms and spectra of optical sinc pulses. (a) Optical sinc pulses with 5, 7, and 9 comb lines when the MZM is driven by 10, 20, 30, 40 GHz. (b) Optical sinc pulses with 4, 6, and 8 comb lines when the MZM is driven by 5, 15, 25, 35 GHz. Blue: experiment; Orange: simulation.

Figure 3.3 presents the measured waveforms and spectra of synthesized optical sinc pulses, where the number of comb lines ranges from 3 to 9 while maintaining the comb FSR at 10 GHz. The temporal waveforms are very close to the ideal sinc functions for all cases, and



the sinc pulse width gets narrower with more spectral comb lines. With regards to the sinc pulses with odd number of comb lines, the spectra show characteristic rectangular shapes, with minimum power imbalance and high SMSR. As seen in Figure 3.3 a for 5, 7, and 9 comb lines, the flatness is 0.08 dB, 0.09 dB, and 0.15 dB, and the SMSR is about 30.0 dB, 30.4 dB, and 23.9 dB, respectively. In terms of even number of lines with 4, 6, 8 combs shown in Figure 3.3 b, the flatness is measured to be 0.08 dB, 0.05 dB, and 0.12 dB, respectively. However, the SMSR is much smaller compared to the odd number of comb lines, as the laser carrier cannot be completely notched, limited by the extinction ratio of the MZM. The SMSR is measured to be 12.2 dB, 11.8 dB, and 11.2 dB.

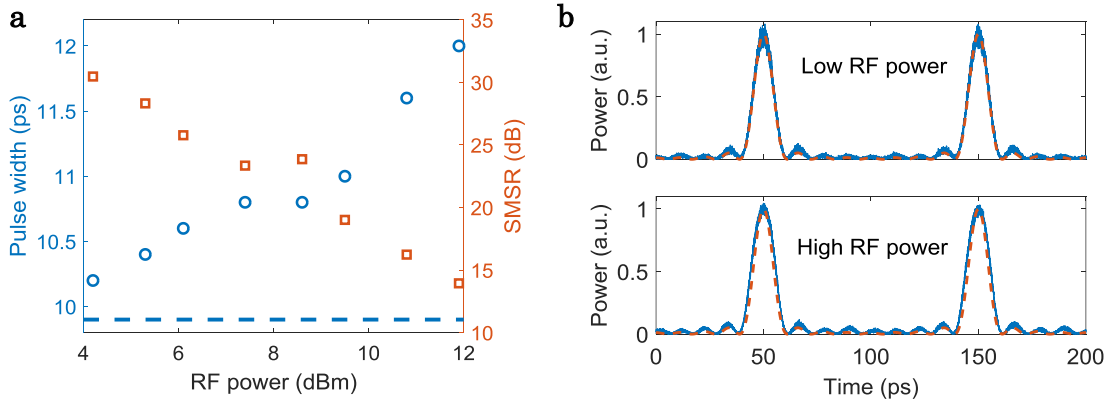


Figure 3.4 – Optical sinc pulses of 9 comb lines under different RF power levels. (a) The measured pulse widths of sinc pulses (blue) and SMSR of the comb spectra (orange) versus the RF power input to the MZM. Blue dashed line corresponds to the ideal FWHM of sinc pulse with 9 comb lines. (b) The temporal waveform of the sinc pulses under 4.2 dBm (top) and 11.9 dBm (bottom), respectively. Blue: experiment; Orange: simulation.

Optical sinc pulse generation under different RF power level is also studied, in the case of 9 comb lines as an example. As mentioned above, the multi-harmonic method only generates sinc pulses under small RF power, therefore, the optical pulses obtained under large RF power deviate from the ideal sinc shapes. This can be seen in Figure 3.4 a. In the frequency domain, the pulse spectra show worse SMSR with the increase of input RF power, which is due to the fact that the MZM generates stronger higher-order sidebands. In the time domain, the FWHM pulse width also increases with the RF power input to the MZM, and diverges from the ideal sinc pulse width of 9.9 ps (indicated as blue dashed line in Figure 3.4 a). Figure 3.4 b showcases the measured optical waveforms under low RF power (top, 4.2 dBm) and high RF power (bottom, 11.9 dBm). It can be clearly seen that the sinc pulses under low RF power modulation are better fit with the ideal sinc pulses (the mean absolute deviation of the normalized waveforms are 1.4% and 2.7%, respectively). Nonetheless, since the MZM is biased either at or close to the MITP, using small signal modulation results in low pulse power. Such low power will bring in excessive ASE after the pulse amplification. Therefore, there exists a trade-off between the perfect sinc pulse shape and the optical signal-to-noise ratio (OSNR).

### 3.4 RF photonic filters of sinc responses

RF filters based on optical frequency combs and dispersive propagation enable RF signal processing in the photonic domain [37, 39]. Compared to their electrical counterparts, this approach provides versatile filter shapes and wide tuning range empowered by the possible line-by-line shaping of the optical combs [80–83]. For instance, highly selective rectangular RF filters have been demonstrated using programmable pulse shapers to tailor the optical frequency combs [153] or slice ASE source [154]. From a communication perspective, RF photonic filters with sinc responses may offer promising potential to high-speed OFDM systems, optimizing the spectral efficiency among electrical, optical, and wireless applications. Given the complex features of sinc-shaped RF filters, direct implementation in the electrical domain is challenging.

On the other hand, RF photonic filters with sinc responses can be obtained based on rectangular frequency spectra. Since we know how to directly generate optical sinc pulses that also show rectangular spectra, we would like to apply this to the RF photonic filtering. As mentioned above, the linear phase relation of the comb lines is generally not required for most of the comb-based RF filters [37, 80]. As in the case of optical sinc pulse generation, we also target sinc-shaped RF filters without additional spectral shapers. But here we use two cascaded MZMs driven by synchronized RF frequencies to obtain rectangular comb spectra [63]. The proposed RF filter scheme can be easily reconfigured by modifying the RF signals (frequency, power), and the DC bias driving the MZMs. The flexibility of the RF filters are shown by varying the number of comb lines, thereby changing the number of filter taps while maintaining near perfect sinc responses.

**Principle of comb-based RF filter with sinc response.** The conceptual setup and experimental implementation of comb-based RF filter is illustrated in Figure 3.5. Note that similar operation also applies to Chapter 5. The comb source (dashed box) is obtained by external modulation of a CW laser using two cascaded MZMs, driven at frequency  $f_1$  and  $f_2$ , respectively. Then the generated comb goes to a DP-MZM through a polarization controller. A small portion of combs is tapped for spectrum monitoring on an OSA. The RF signal from the vector network analyzer (VNA) is loaded to the in-phase and quadrature ports of the DP-MZM through an electrical  $90^\circ$  hybrid coupler. After propagation through a spool of dispersion compensating fiber (DCF), the comb carriers and SSB signals acquire differential delays. Finally, the optical signals are directed to a photodetector (PD) where they beat to retrieve the original RF signal. The response of the obtained RF photonic filter is measured by the VNA.

Let us generalize the operating principle of comb-based RF filters by considering the frequency combs of arbitrary shapes:

$$E_{comb}(t) = E_0 \exp(ik\omega_0 t) \sum_{k=0}^{N-1} a_k \exp(ik2\pi \Delta f t) \quad (3.13)$$

where  $N$  is the number of comb lines. The comb lines are spaced by  $\Delta f$  in frequency, and the

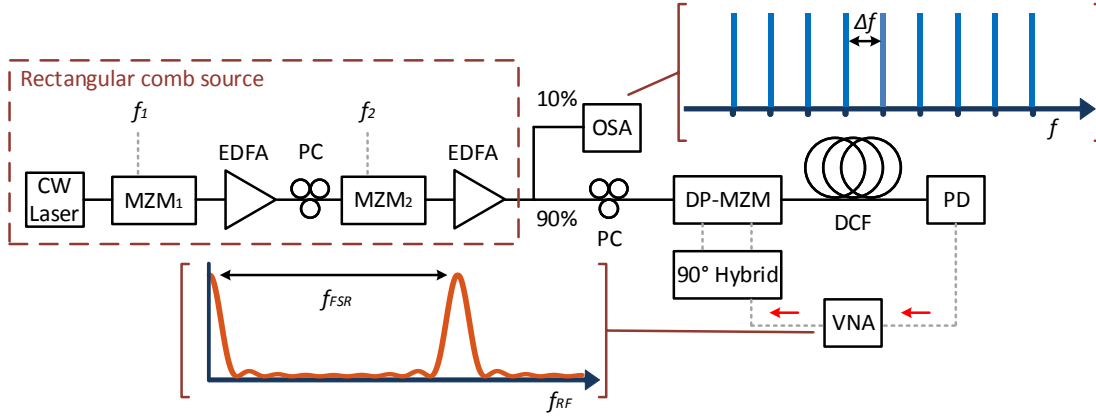


Figure 3.5 – Experimental setup of sinc-shaped RF filters based on rectangular optical combs. EDFA: erbium-doped fiber amplifier; PC: polarization controller; DCF: dispersion compensating fiber; PD: photodetector; OSA: optical spectrum analyzer; VNA: vector network analyzer. The rectangular optical combs are generated using two MZMs driven by two RF frequencies  $f_1$  and  $f_2$  separately. The RF signal from the VNA is upconverted to the optical domain in a DP-MZM via the electrical  $90^\circ$  hybrid. Then the frequency comb lines carrying the information of the RF signals acquire differential delays through propagation in a spool of DCF. After being detected by the PD, the RF signal is retrieved and send back to the VNA for the filter response measurement. The images of OSA and VNA show the target rectangular optical comb spectrum and sinc-shaped RF response, respectively.

$\omega_0$  denotes the angular frequency of the first line.  $a_k$  is the complex amplitude of each comb line, which contains both amplitude and phase information. Then the frequency combs are injected to the DP-MZM, which is modulated by the scanning RF signal  $f_{RF}$  from the VNA. As detailed in Section 2.1, DP-MZM could achieve SSB modulation with an arbitrary ratio between the carrier and the sideband:

$$E_{DP-MZM}(t) = E_0 \exp(ik\omega_0 t) \sum_{k=0}^{N-1} a_k \exp(ik2\pi\Delta f t) (1 + \gamma \exp(i2\pi f_{RF} t)) \quad (3.14)$$

where  $\gamma$  is the coefficient between the sideband and the carrier. It can be seen from Eq. (3.14) that the RF signal now is broadcast to the frequency combs. Then the optical signals propagate through a dispersive medium (DCF used here), where they would pick up quadratic phases as:

$$E_{DCF}(t) = E_0 \exp(ik\omega_0 t) \sum_{k=0}^{N-1} a_k \{ \exp(ik2\pi\Delta f t + i\Theta_2 2\pi^2 (k\Delta f)^2) + \dots \gamma \exp(ik2\pi\Delta f t + i2\pi f_{RF} t + i\Theta_2 2\pi^2 (k\Delta f + f_{RF})^2) \} \quad (3.15)$$

where  $\Theta_2 = -\beta_2 L$  refers to the product of group velocity dispersion (GVD) of the fiber  $\beta_2$  and fiber length  $L$ . At the output of dispersive propagation, each carrier and sideband receives a distinct quadratic phase. Then the optical signals are converted back to electrical signals at a

square-law PD. Since the VNA measures at the frequency it sent out (i.e.  $f_{RF}$ ), the photocurrent generated at  $f_{RF}$  frequency is given by [80, 155]:

$$\begin{aligned} i_{f_{RF}}(t) &\sim \frac{1}{2} r \langle |E(t) + E^*(t)|^2 \rangle \\ &= r |E_0|^2 \sum_{k=0}^{N-1} |a_k|^2 |\gamma|^2 \cos(2\pi f_{RF} t + \Theta_2 4\pi^2 \Delta f f_{RF} + \Theta_2 2\pi^2 f_{RF}^2 + \theta_\gamma) \end{aligned} \quad (3.16)$$

where  $\langle \rangle$  stands for the averaging at optical frequency and  $r$  is the responsivity of the PD.  $|\gamma|$  and  $\theta_\gamma$  is the amplitude and phase of  $\gamma$ , i.e.  $\gamma = |\gamma| \exp(i\theta_\gamma)$ . Therefore, the transfer function  $H(f_{RF})$  of the comb-based RF filter can be found:

$$H(f_{RF}) \sim \exp(i\Theta_2 2\pi^2 f_{RF}^2) \sum_{k=0}^{N-1} |a_k|^2 \exp(i\Theta_2 4\pi^2 \Delta f f_{RF}) \quad (3.17)$$

In the above equation, we have omitted all the scaling factors and the static phase. The filter function consists of a quadratic phase term and the discrete Fourier transform of the comb intensity  $|a_k|^2$ . Therefore, the RF filter response can be seen as a TDL filter, where  $|a_k|^2$  are the tap weights. Also the response is periodic with the frequency  $f_{FSR} = 1/2\pi\Theta_2\Delta f$ . Since the tap weights of the filter are all-positive, the response shows peaks at  $n f_{FSR}$ , ( $n = 0, 1, \dots$ ). When the input comb spectrum is rectangular (i.e.  $|a_k|^2 = 1$ ,  $k = 1, \dots, N$ ), Eq. (3.17) rewrites:

$$\begin{aligned} H(f_{RF}) &\sim \exp(i\Theta_2 2\pi^2 f_{RF}^2) \frac{\exp(i\Theta_2 4\pi^2 N \Delta f f_{RF}) - 1}{\exp(i\Theta_2 4\pi^2 \Delta f f_{RF}) - 1} \\ &\sim \exp(i\Theta_2 2\pi^2 f_{RF}^2 + i\Theta_2 2\pi^2 (N-1) \Delta f f_{RF}) \frac{\sin(\Theta_2 2\pi^2 N \Delta f f_{RF})}{\sin(\Theta_2 2\pi^2 \Delta f f_{RF})} \end{aligned} \quad (3.18)$$

where the amplitude response of  $H(f_{RF})$  actually corresponds to periodic sinc functions. This can be derived as for Eq. (3.7) and (3.8):

$$\frac{\sin(\Theta_2 2\pi^2 N \Delta f f_{RF})}{\sin(\Theta_2 2\pi^2 \Delta f f_{RF})} = \begin{cases} N \sum_{k=-\infty}^{\infty} (-1)^k \frac{\sin(N\Theta_2 2\pi^2 \Delta f (f_{RF} - k f_{FSR}))}{N\Theta_2 2\pi^2 \Delta f (f_{RF} - k f_{FSR})}, & \text{if } N \equiv 0 \pmod{2} \\ N \sum_{k=-\infty}^{\infty} \frac{\sin(N\Theta_2 2\pi^2 \Delta f (f_{RF} - k f_{FSR}))}{N\Theta_2 2\pi^2 \Delta f (f_{RF} - k f_{FSR})}, & \text{if } N \equiv 1 \pmod{2} \end{cases} \quad (3.19)$$

Here we have confirmed that the RF filter based on rectangular comb is indeed of sinc shape. The quadratic phase term represents a linear group delay additional to the periodic sinc carver, which is due to the modulation scheme being used [155]. While the linear phase term vanishes when the center of the comb is set as reference.

**Experimental results.** In the experiment, MZM<sub>1</sub> and MZM<sub>2</sub> are driven by RF clocks of 30 GHz and 20 GHz, respectively. By properly setting the RF power and DC bias to MZM<sub>1</sub>, 2 comb lines (carrier suppressed), 3 comb lines (odd-order harmonics suppressed), or 4 comb lines

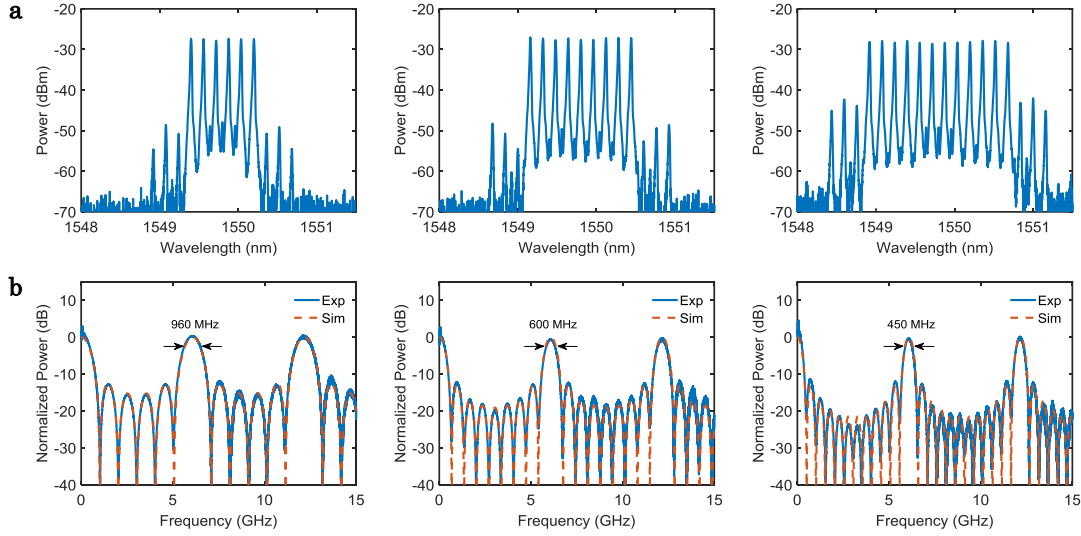


Figure 3.6 – RF photonic filters with sinc responses based on optical combs with rectangular shapes. (a) Optical rectangular combs generated based on cascaded MZMs with 6, 9, 12 spectral lines at 20GHz comb FSRs. (b) Corresponding sinc-shaped RF photonic filters based on rectangular combs in (a). The 3 dB bandwidth of the RF filters are indicated. Blue: experiment; Orange: simulation (ideal sinc).

(even-order harmonics suppressed) spaced at  $2f_1 = 60$  GHz are generated. While the  $\text{MZM}_2$  is driven at  $f_2 = 20$  GHz to triple the number of comb lines and lower the comb repetition rate to  $\Delta f = f_2$ . The resultant frequency combs with 6, 9, and 12 comb lines and 20 GHz comb FSRs are illustrated in Figure 3.6 a. They show flatness of 0.5 dB, 0.6 dB, 0.7 dB, and SMSR of 20.3 dB, 20.8 dB, 13.8 dB, respectively. Note that these rectangular combs do not necessarily correspond to sinc pulses in time. The DCF module we used in the experiment could compensate the dispersion of 60 km SMF fiber. Consider the typical 17 ps/nm/km of SMF in C-band, the DCF corresponds to -1020 ps/nm amount of dispersion and results in  $\Theta_2 \approx 1.3 \times 10^{-21} \text{ s}^2$  at 1550 nm. Therefore, the peak of the RF filter can be predicted by  $f_{\text{FSR}} = 1/2\pi\Theta_2\Delta f \approx 6.1$  GHz. All these filters operate within the first Nyquist zone (DC to 10 GHz) so that they are free from spurious frequency [80]. Figure 3.6 b shows the measured RF filter responses, where all of them exhibit near perfect sinc shapes. Center frequencies of these filters are as predicted at around 6.1 GHz. By varying the rectangular comb bandwidths from 120 GHz to 240 GHz, the 3 dB bandwidths of the corresponding sinc-shaped filters are reconfigured from 960 MHz to 450 MHz.

We also study the phase responses of the sinc-shaped RF filters. Figure 3.7 shows the measured phase response of the filter based on rectangular combs constituting 9 lines. Note that here the quadratic phase is not shown as the VNA is calibrated on the single laser carrier. The measured phase response is then unwrapped, which demonstrates clear  $\pi$  phase jump at every notch point of the amplitude response, as the sinc function flips the sign at every zero crossing. The experimental results match well with simulated pure  $\pi$  phase jumps at the amplitude nulls.

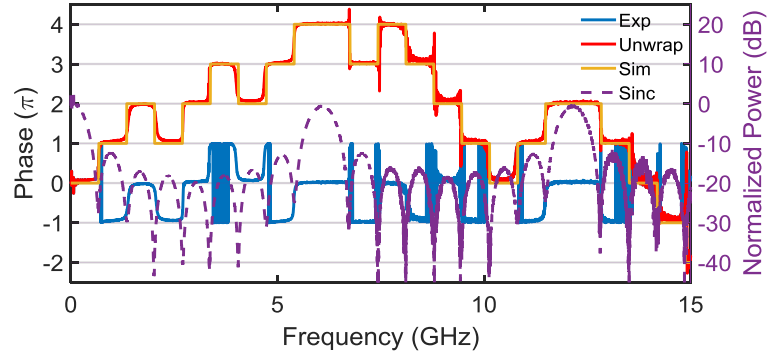


Figure 3.7 – Phase response of the RF photonic filter based on the rectangular combs with 9 spectral lines. Blue: measured phase response; Orange: unwrapped phase response; Yellow: simulated phase response; Purple: measured power response. The RF filter shows  $\pi$  phase jumps at the nulls of the sinc function.

### 3.5 Add-drop multiplexer for Nyquist OTDM system

All-optical ADM is a key element in high data rate optical networks to completely extract a channel while inserting a new channel back to the link, without involving optical to electrical domain conversion. It has been widely investigated in both TDM and WDM systems in the past decades. Recently, the development of high spectral efficiency superchannels such as OFDM, Nyquist WDM, and Nyquist OTDM, have reinforced the design consideration of their corresponding ADMs, due to the fact that they are more compactly packed in either time or frequency domains. For Nyquist WDM signals, the pulse shaper, also known as a wavelength selective switch (WSS) can fulfill the add-drop functionality as in general for WDM system [147]. A ring-assisted MZI pre-filtering interleaver with sharp response, in conjugation with a WSS, has been utilized to enhance the add-drop ability of Nyquist WDM with minimum guard band [148]. OFDM ADM has been demonstrated by first demultiplexing the target channel, then destructive interfering the original signal with dropped channel to clear up the spectral slot for the new channel [70]. However, for Nyquist OTDM system - the temporal counterpart of OFDM, an ADM architecture is still elusive.

In this section, we propose a simple ADM structure for Nyquist OTDM signals. Unlike TDM systems, Nyquist OTDM systems consist of a number of sinc pulse subchannels that are orthogonally overlapped in time (when roll-off factor is 0). This makes it difficult to notch a single channel while not affecting the rest. The specific requirement of the ADM would be the complete notch at the temporal positions of the target subchannel, while being lossless at the other zero ISI points. This feature somewhat resembles the sinc function but in a flipped manner, or termed as dark sinc function. Therefore, we could basically utilize the complementary nature of dual-output modulators. When one of the modulator output gives the periodic sinc pulse trains, the other port would be the dark sinc pulse trains.

**Optical bright and dark sinc carver pair.** The proposed ADM architecture is based on this

simple principle. It uses multi-port MZM for the simultaneous synthesis of bright and dark sinc pulse carver pair. Such MZMs are commercially available. For example, EOSPACE provides both  $1 \times 2$  MZM (one input, two outputs) and  $2 \times 2$  MZM (two inputs, two outputs). These MZMs can be explored to obtain the pulse carvers exactly the same way as generating sinc pulses driven by multi-harmonic RF signals. The bright and dark sinc functions are respectively the matched sampling/pulse shaping and the notch functions needed for add-drop of Nyquist OTDM signals. A proof-of-concept simulation is carried out for 50 Gb/s on-off keying (OOK) Nyquist OTDM system, which is aggregated from  $5 \times 10$  Gb/s orthogonal subchannels. Two slightly different ADM implementations are proposed, and are compared in terms of add-drop setups and penalties.

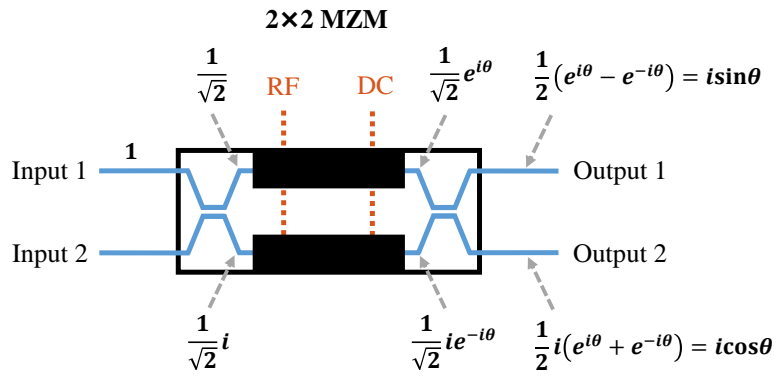


Figure 3.8 – Layout of  $2 \times 2$  MZM with the flow of optical fields. As an example, the optical modulation function is calculated when a unit optical field is injected to the input port 1 of the  $2 \times 2$  MZM. The modulation function for the bar coupling and cross coupling are respectively  $i \sin \theta$  and  $i \cos \theta$ , where  $\theta$  denotes the total phase shift per arm.

Let us recall the operating principle of the conventional MZM driven by multi-harmonic RF signals (Eq. (3.10)). In fact, this just corresponds to one of the output port of the MZI structure, while the other port should be the complement of Eq. (3.10). The total power is preserved due to energy conservation. Considering the most general  $2 \times 2$  MZM topology as sketched in Figure 3.8, the modulation function can be derived:

$$m_{ij}(t) = \begin{cases} i \sin(\psi + \sum_{k=1}^N \beta_k \cos \omega_k t), & \text{if } i = j, \text{ bar function} \\ i \cos(\psi + \sum_{k=1}^N \beta_k \cos \omega_k t), & \text{if } i \neq j, \text{ cross function} \end{cases} \quad (3.20)$$

where  $m_{ij}$  is the temporal modulation function connecting the input port  $i$ , ( $i = 1, 2$ ) and output port  $j$ , ( $j = 1, 2$ ). As defined previously,  $\psi = V_{DC}/2V_{\pi,DC}$  is the normalized bias,  $\beta_k = V_k/2V_{\pi,\omega_k}$  are the modulation indices for RF frequencies  $\omega_k$ , ( $k = 1, \dots, N$ ). For simplicity, we drop the common static phase shift  $i$ . Here the modulation function of the multi-port MZM is defined instead of its output optical field. The derivation of Eq. (3.20) can be carried out as implemented in Figure 3.8. It is found that the bar coupling ( $i = j$ ) and the cross coupling

( $i \neq j$ ) functions are respectively sine and cosine functions, which are indeed complementary in terms of power.

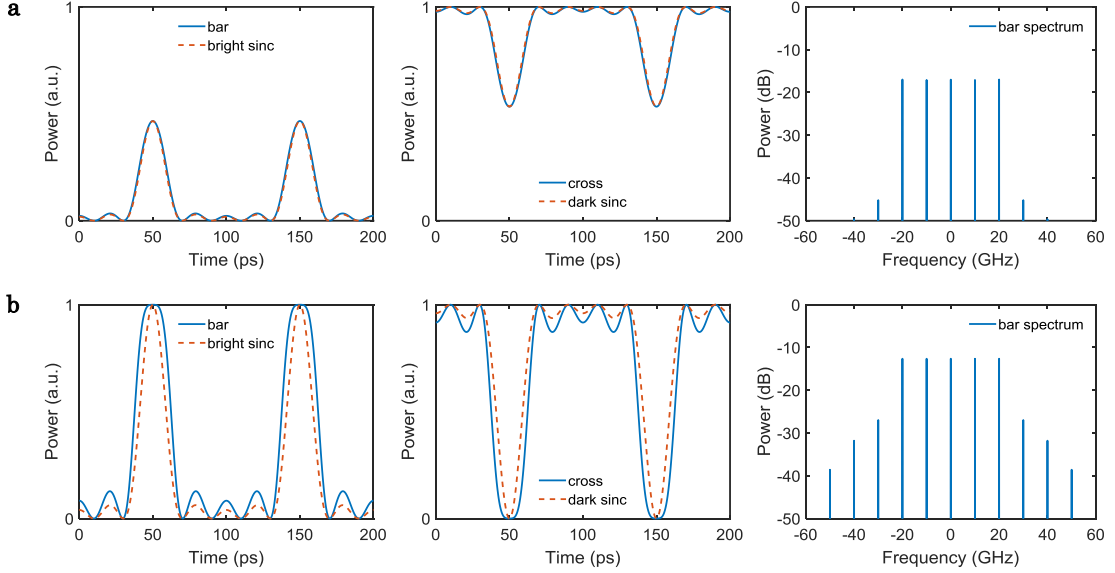


Figure 3.9 – Bar and cross pulse carvers in comparison with ideal bright and dark sinc functions. The  $2 \times 2$  MZM is driven by two RF frequencies at 10 GHz and 20 GHz. (a) When the RF modulation is weak, the bar function is close to the ideal sinc shape and its rectangular spectrum shows high SMSR. However, the cross function could not achieve the complete notch in time. The simulation is obtained by  $\psi = 0.152$ ,  $\beta_1 = 0.3$ , and  $\beta_2 = 0.3$ . (b) When the RF modulation is large, the bar function deviates from the ideal sinc shape and its rectangular spectrum shows poor SMSR. The cross function does achieve almost complete notch in time, and shows nearly no loss at the other ISI points. The simulation is obtained by  $\psi = 0.323$ ,  $\beta_1 = 0.635$ , and  $\beta_2 = 0.605$ .

Since we consider the Nyquist OTDM system with  $5 \times 10$  Gb/s substreams, the pulse carvers associated to it should be the sinc function with 5 spectral lines spaced at 10 GHz, as well as its complement. Regarding the implementation, the  $2 \times 2$  MZM is driven by two RF frequencies at 10 GHz and 20 GHz. Without loss of generality, let us assume that the bar function achieves the bright sinc shape that may be used for matched sampling or pulse shaping. Noticeably, the sinc pulse condition can only be realized under weak RF modulation as described in section 3.3. While in this scenario, the cross function could not achieve complete notch in time as shown in Figure 3.9 a. This does not fulfill the notch function of ADM, as one of the subchannel needs to be completely removed. Therefore, RF power needs to be increased. By properly adjusting the RF power and the DC bias to the  $2 \times 2$  MZM, complete notch can be achieved for the cross coupling function as shown in Figure 3.9 b. Clearly, the cross function obtained deviates from the ideal dark sinc shape. This can also be seen from its complementary bar function, which shows broader transmission window than the ideal sinc shape in time. In frequency domain, a number of sidebands in addition to the rectangular spectrum is also observed. Luckily, the synthesized dark sinc carver shows minimal loss at the ISI points of the



Nyquist OTDM signals. In Figure 3.9 b, the zero positions of the dark pulse carver are within 0.4 ps deviation from the ideal sinc for 20 ps channel spacing, well maintaining the zero ISI criterion. Moreover, the proposed method is fully flexible in terms of the sinc carver width based on the multi-harmonic technique described in 3.3. This correspondingly adapts the ADM for Nyquist OTDM comprised of different subchannel number.

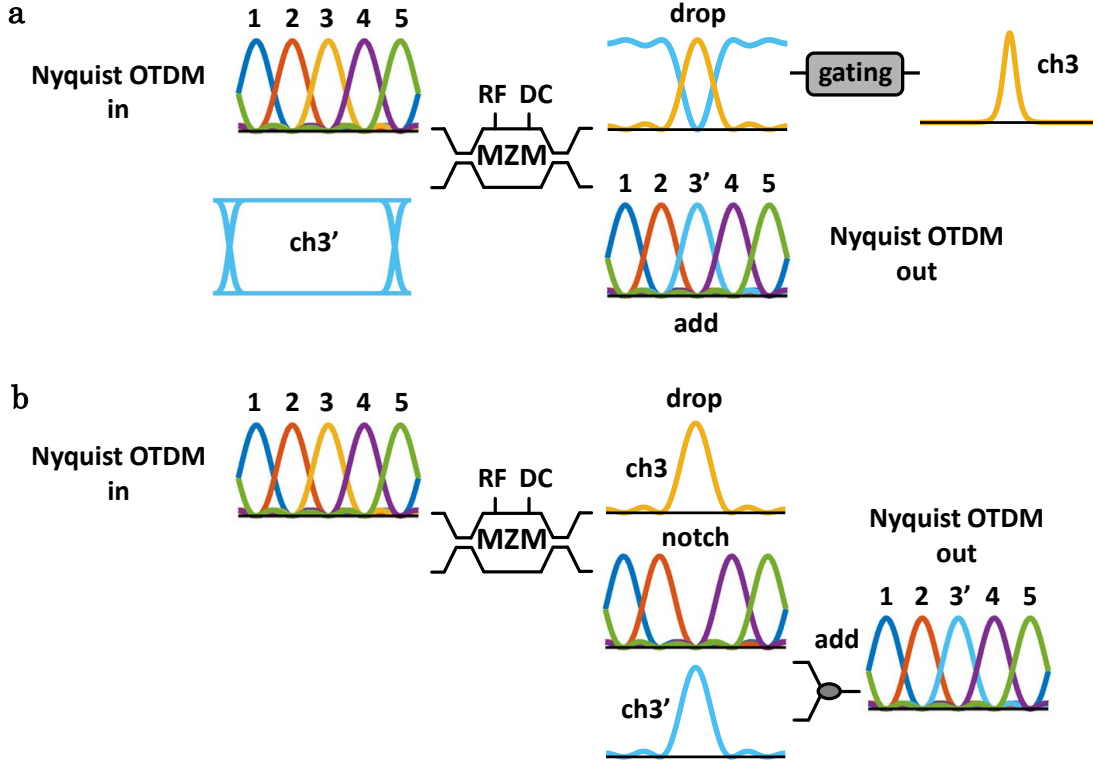


Figure 3.10 – Schematic diagrams of add-drop multiplexers based on  $2 \times 2$  MZM operated as simultaneous bright and dark sinc carvers. (a) The original multiplexed Nyquist OTDM channels (ch1, ..., ch5) and the new channel ch3' are directed to the two input ports of the  $2 \times 2$  MZM. One of the output of the MZM after temporal gating corresponds to the dropped ch3. The other port directly outputs the Nyquist OTDM signals with ch3 being replaced by the new ch3'. (b) Only the original multiplexed Nyquist OTDM channels are injected to the MZM. The two outputs of MZM correspond to the dropped ch3 and the Nyquist OTDM signals with ch3 being notched, respectively. The new channel ch3' is then combined with the notched Nyquist OTDM signals in an optical coupler, thereby forming the new Nyquist OTDM signals with ch3' instead of ch3.

**ADM structures for Nyquist OTDM.** Figure 3.10 presents two add-drop schemes based on multi-port MZM. When both of the  $2 \times 2$  MZM inputs are utilized (Figure 3.10 a), the Nyquist OTDM signals and the new channel ch3' are directed to the upper and lower input port of MZM simultaneously. Note that here the added ch3' can be input to the MZM without prior sinc pulse shaping. Since the MZM functions as a bright sinc for bar coupling and a dark sinc for cross coupling, the lower output port will receive new ch3' with sinc carving, while the ch3

within the original Nyquist OTDM signals will be notched out. This is exactly the add function of the incoming Nyquist OTDM signals, where  $ch3$  is replaced by  $ch3'$ . Here the insertion of  $ch3'$  at the right time slot (where  $ch3$  being cleared up) is automatically guaranteed by the complementary nature of MZM carver pair, although we do need a electrical or optical delay line to align the symbol with peak of the sinc function. For the upper output port, the bright sinc carver extracts  $ch3$  from the incoming Nyquist OTDM stream by quasi-matched sampling [68, 156], and the dark sinc carves the added  $ch3'$ . Therefore,  $ch3$  is dropped out at the upper output port with background interference from dark sinc of  $ch3'$ . An optical gating stage is required to clear  $ch3'$  and finally drop out  $ch3$ .

In order to get rid of the  $ch3'$  in the drop port, a modified add-drop scheme is proposed without adding  $ch3'$  directly (Figure 3.10 b). In this case, the upper output port of the  $2 \times 2$  MZM functions as a quasi-matched sampler of the incoming streams thereby drop out  $ch3$ , while the lower output corresponds to the original signal with  $ch3$  notched out. Therefore, the lower output of MZM creates an empty time slot for the insertion of  $ch3'$  via a simple optical coupler. Unlike in Figure 3.10 a, here  $ch3'$  needs prior Nyquist pulse shaping before the insertion. However, the temporal gating of the dropped signal is not necessary for this implementation. To sum up, in order to perform the full ADM, the first implementation requires an additional gating stage while the second implementation requires an additional sinc shaping stage.

The simulation setups of the proposed ADM schemes are depicted in Figure 3.11. The typical setup of Nyquist OTDM transmitter is first shown in Figure 3.11 a [63]. A CW laser is externally modulated by synchronized 10 GHz and 20 GHz RF signals to obtain sinc pulse trains with 5 comb lines, and then split to 5 streams. Each stream is independently modulated by 10 Gb/s electrical data symbols with 10% rise-time (10 ps). This forms in total 50 Gb/s Nyquist OTDM signals after recombining these 5 subchannels with proper delays (eye diagram Figure 3.11 (i)). The Nyquist OTDM signals are then directed to a  $2 \times 2$  MZM for the add-drop multiplexing. Figure 3.11 b and Figure 3.11 c respectively correspond to the ADM schemes described in Figure 3.10 a and Figure 3.10 b, including the required measurement setups for the assessment of their add-drop performances. Here the bit error rates (BER) of all channels are estimated by direct counting with iterative Monte-Carlo method. A Gaussian-distributed optical white noise is loaded to emulate the OSNR, in order to assess the penalties of proposed ADMs. In Figure 3.11 b, typical 8 ps FWHM pulses from electro-absorption modulator (EAM) [157] is simulated to gate the drop signal. In all cases, the overall data streams are matched sampled with an optical sinc pulses of the same shape generated by MZM [156]. A 20 GHz Gaussian-shaped optical bandpass filter is used for all cases to open up the optical eyes before the BER estimation.

The eye diagrams at different positions of the two ADM schemes are explicitly shown in Figure 3.11. It can be seen that the zero ISI property is well maintained after clearing  $ch3$  and inserting  $ch3'$  (Figure 3.11 (iii) and (vi) respectively for the two schemes), although the eye shapes are a bit distorted. For the drop ports, an optical gating is required for the ADM scheme described

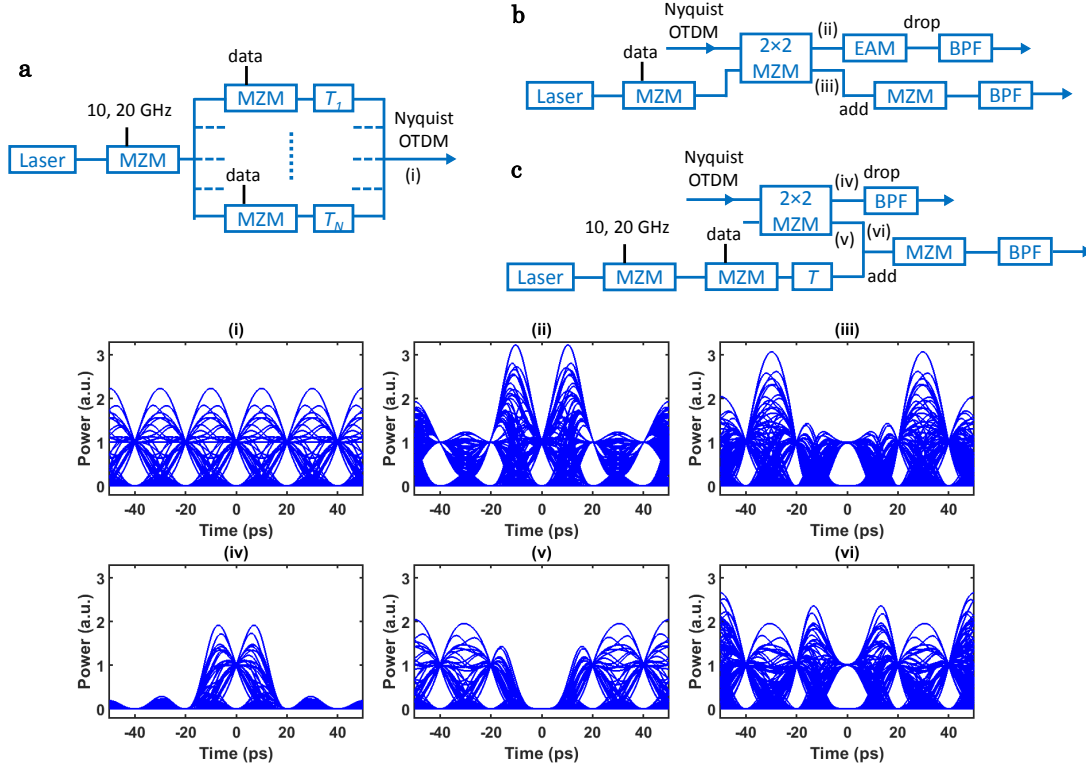


Figure 3.11 – Simulation setups for the assessment of Nyquist OTDM ADMs. (a) Nyquist OTDM transmitter consists of 5 streams of time-multiplexed 10 Gb/s modulated sinc pulse trains. (b) The proposed ADM based on both input ports of the  $2 \times 2$  MZM as well as its detection setup. (c) The proposed ADM based on only one input port of the  $2 \times 2$  MZM as well as its detection setup. (i)-(vi) are eye diagrams at different locations specified in the setups (a)-(c). (i) original Nyquist OTDM signals; (ii) dropped signal ch3 in (b); (iii) new Nyquist OTDM signals with ch3' replacing ch3 in (b); (iv) dropped signal ch3 in (c); (v) notched Nyquist OTDM signals (without ch3); (vi) new Nyquist OTDM signals with ch3' replacing ch3 in (c).

in Figure 3.10 a. It samples at the correct time points where ch3 is maximized and ch3' is minimized (Figure 3.11 (ii)), as a strong ch3' background is present at the eye. But this is not necessary for the scheme depicted in Figure 3.10 b without the distortion from ch3' (Figure 3.11 (vi)).

**Performance assessment of the ADM schemes.** Figure 3.12 shows the estimated BER performance of the proposed ADMs. Ch1 and ch2 have very similar BER to ch5 and ch4, respectively, as they are mirrored channels with respect to ch3, and are thus not plotted. This is also manifested from the eye diagrams in Figure 3.12 (iii) and (vi). 7% hard-decision forward error correction (FEC) threshold ( $\text{BER} = 3.8 \times 10^{-3}$ ) is plotted as a reference. The ideal curve in Figure 3.12 corresponds to the BER performance of back-to-back matched sampling, setting as the benchmark for penalty estimation. The receiver sensitivity of the proposed ADMs are all assessed at  $\text{BER} = 1 \times 10^{-3}$ . When the Nyquist OTDM signals and new subchannel ch3 are

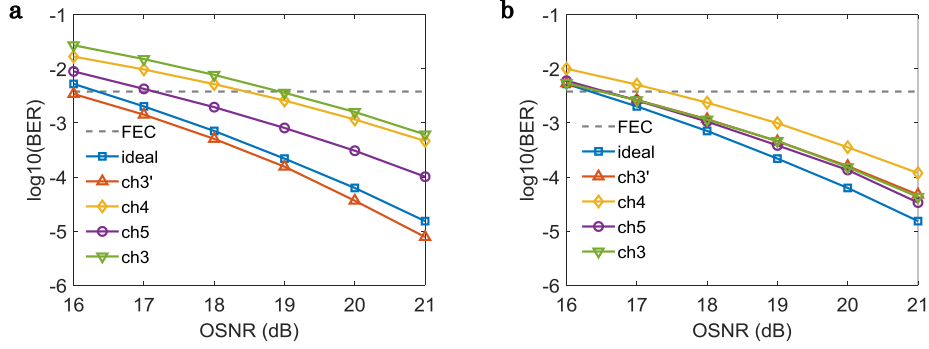


Figure 3.12 – BER performances of proposed ADMs based on  $2 \times 2$  MZM. (a) BER curves of add, drop, and other subchannels when the ADM uses both of the input ports of  $2 \times 2$  MZM. (b) BER curves of add, drop, and other subchannels when the ADM uses only one of the input ports of  $2 \times 2$  MZM. FEC: 7% hard-decision forward error correction threshold ( $\text{BER} = 3.8 \times 10^{-3}$ ); Ideal: back-to-back matched sampling.

injected to the  $2 \times 2$  MZM simultaneously (Figure 3.12 a), the penalties of ch4, and ch5 are respectively 2.5 dB and 1.1 dB, while ch3' is enhanced by 0.3 dB rather than degraded. The gain of ch3' is due to the fact that the synthesized carver of MZM is actually broader than the ideal sinc shape. This broader carver not only clears more temporal space for ch3', but also shapes ch3' to occupy more time slot. The effect is clearly seen in the eye of ch3' that is wider after the ADM (Figure 3.11 (iii)) compared to initial eye (Figure 3.11 (i)). A 2.8 dB difference is observed for the drop ch3 with respect to the ideal matched sampling. This can be improved by using shorter pulse for optical sampling. When only the Nyquist OTDM signals are injected to the  $2 \times 2$  MZM (Figure 3.12 b), the penalties are reduced as ch3' is shaped to near perfect sinc before being multiplexed. Ch3', ch4, ch5 show respectively 0.5 dB, 1.3 dB, and 0.4 dB penalties, while a difference of 0.5 dB is observed for the dropped ch3. In both schemes, the subchannels adjacent to the added ones (ch4) are the most degraded rather than the added channels themselves (ch3). When we separate the implementation of add and notch functions, it significantly reduces the penalty at the cost of prior sinc shaping of ch3 before adding to the link. Also the coupler to combine ch3' and the notched Nyquist OTDM channels inevitably possesses 3 dB loss. However, this scheme allows the direct detection of the dropped ch3 without additional optical gating.

Note that the proposed ADMs are limited by the modulator bandwidth and scalability of multi-harmonic RF signals, therefore not readily suitable for ultra-short pulse Nyquist OTDM systems. In this scenario, lossless time-lens method [60] may be adopted to expand the bandwidth before the  $2 \times 2$  MZM, together with dispersion compensating stage to obtain complementary short pulse carver pair. It is worth to mention that the proposed approach is in principle modulation format transparent. Nevertheless, the performances of the proposed ADMs are sensitive to the modulation depth of the RF signals, therefore would require  $2 \times 2$  MZM with high extinction ratio.

### 3.6 Conclusions

In conclusion, a simple yet fully flexible optical sinc pulse generator is demonstrated. By using multi-harmonic synchronized RF signals to drive a single-stage MZM, the full control is given over the repetition rate, the duty cycle, and the central wavelength without external pulse shaping. Based on 2 to 4 RF sinusoidal waves, we report optical generation of sinc pulses of 4 to 9 comb lines at a constant repetition rate of 10 GHz, together with clear rectangular comb spectra. Moreover, we investigate the impact of the RF signal power on the synthesized sinc pulses, and highlight the trade-off between the pulse quality and the ideal sinc shape.

In addition, RF filters with near perfect sinc responses are demonstrated based on optical combs of rectangular shapes. Here the rectangular combs are directly generated from the MZMs without external shaping. The filter bandwidths are easily reconfigured by changing the number of comb lines, via tuning of the DC bias and RF power input to the MZMs. While the center frequencies of the RF filters can be adjusted by changing the driving RF frequencies or using interferometric setup [80]. Such sinc-shaped RF filters may be useful in demultiplexing subcarriers for RF OFDM systems.

At last, two add-drop multiplexing schemes are proposed for Nyquist OTDM signals. While slightly different in the detailed implementations, both ADM approaches utilize the bright and dark sinc carver pair synthesized from a  $2 \times 2$  MZM. Such complementary sinc pulse carvers are demanded in the sampling/shaping and notch procedures of ADM realization. The add-drop performances of two approaches are assessed and compared in proof-of-concept simulation. The proposed ADM schemes would empower the optical Nyquist OTDM systems with the ability of flexibly switching subchannels in the optical domain.

## 4 Temporal and azimuthal Talbot effects

The content in this chapter is based on the following publications:

- **J. Hu**, C.-S. Brès, and C.-B. Huang, "Talbot effect on orbital angular momentum beams: azimuthal intensity repetition-rate multiplication," *Optics Letters*, **43**, 4033-4036 (2018). [158]
- **J. Hu**, S. J. Fabbri, and C.-B. Huang, C.-S. Brès, "Investigation of temporal Talbot operation in a conventional optical tapped delay line structure," *Optics Express*, **27**, 7922-7934 (2019). [159]

### 4.1 Introduction

High repetition-rate optical pulse trains are widely used for high-speed optical communications, optical sampling, and microwave photonics [39]. In addition to increasing the repetition-rate directly at the laser cavity, repetition-rate multiplication (RRM) outside the laser cavity is also sometimes desired [160]. As the optical pulse trains spectrally correspond to frequency combs, RRM is most generally achieved by spectral amplitude filtering. It increases the comb line spacing of the spectrum, using programmable pulse shaper or optical tapped delay line (TDL) structure [48]. Another approach, however, maintains the comb line spacing but applies spectral phase filtering, also known as temporal Talbot effect. Typical methods include using LCFBG [55] or pulse shaper [56].

Here we show that the TDL structure that has long been used for spectral amplitude filtering, can actually function as a temporal Talbot multiplier as well. Moreover, flexible combinations of amplitude and phase filtering can also be implemented in such structure, all leading to the same multiplication factor. The simple TDL structure is amenable to photonic integration, hence very promising for versatile RRM on-chip.

OAM modes of light resemble the frequency comb modes in many ways. They are characterized with the helical phase fronts that are typically integer number of  $2\pi$  around the azimuthal

angle [74]. This integer number is also known as the topological charge. Noticeably, the topological charge of an OAM mode is analogous to the mode index of frequency comb line, while the azimuthal angle can be seen as time but with only one period from 0 to  $2\pi$ . Indeed, the superposition of OAM modes has already been shown to create azimuthal petals [77], similar to pulse train in time domain. Likewise, when a number of OAM modes are superimposed with Talbot phases, azimuthal self-imaging would occur analogous to the temporal Talbot effect. This implies that, the shaping concepts that have been developed for frequency comb or optical pulse, may be adapted for shaping the OAM spectrum or the azimuthal profile of the beam.

In this chapter, I will present the results on the temporal and azimuthal Talbot effects. First, Section 4.2 discusses the mathematical foundations and properties of the Talbot phases used in this thesis. Section 4.3 utilizes these Talbot phases to implement temporal Talbot operation in optical TDL architecture. Section 4.4 extends the self-imaging concept to the OAM modes of light, with the brief introduction of the OAM modes and then the demonstration of the azimuthal Talbot effect.

## 4.2 Properties of Talbot phases

In Section 2.3, we have already described the generalized formula for Talbot phases. Throughout this chapter, the Talbot phases adopted are specifically from [118], which can be formulated as:

$$\phi_n = \begin{cases} \frac{\pi n^2}{N}, & \text{if } N \equiv 0 \pmod{2} \\ \frac{2\pi n^2}{N}, & \text{if } N \equiv 1 \pmod{2} \end{cases} \quad (4.1)$$

where  $n \in \mathbb{Z}$ . Comparing Eq. (4.1) with Eq. (2.13), we have chosen  $p = 1$  and  $q = N$  if  $N$  is an even number, while  $p = 2$  and  $q = N$  if  $N$  is an odd number. For both cases, the greatest common divisors (GCD) between the nominators (without  $\pi n^2$ ) and denominators are 1, i.e.  $\gcd(1, N) = 1$  for even  $N$  and  $\gcd(2, N) = 1$  for odd  $N$ . This satisfies the coprime criterion for Eq. (2.13). In the case of an odd  $N$ , it is noted that 2 is used as the nominator in Eq. (4.1) instead of 1. The reason may be inferred from the Talbot carpet as sketched in Figure 4.1. When  $N$  is even, the first  $N$ -self-images ( $p/q = 1/N$ ) are aligned with the initial images without a period shift, which can be seen from 1/2 and 1/4 indicted in the Talbot carpet with solid boxes. However, for an odd  $N$ , the first  $N$ -self-images always show a period shift compared to the initial images, while the second  $N$ -self-images are aligned. It is manifested from the 1/3 and 2/3 indicted in the Talbot carpet with dashed boxes. And this may account for the definition of Talbot phases when  $N$  is an odd number.

There are peculiar properties of Talbot phases as they are closely related to quadratic Gauss sum [111, 114]. The main property is stated as follows. A sequence of phasors with Talbot

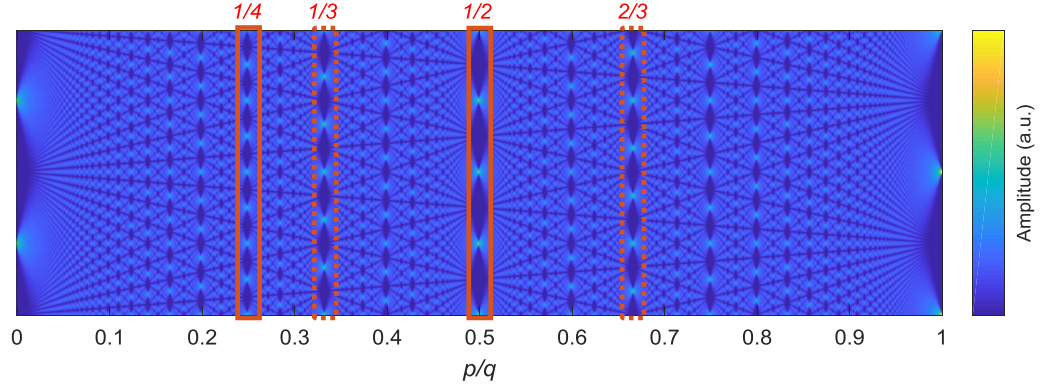


Figure 4.1 – The Talbot carpet (half).  $p/q = 1/4$  and  $1/2$  are indicated with the solid boxes, while  $1/3$  and  $2/3$  are indicated with the dashed boxes. It can be seen that 3-times self-images at  $1/3$  shows a period shift compared to the initial images, while not for  $1/4$ ,  $1/2$ , and  $2/3$ . This may account for the definition of Talbot phases in [118]. Reproduced from [58].

phases, after discrete Fourier transform, also gives another sequence of phasors with Talbot phases. This can be formulated for our Talbot phases as:

$$\sum_{n=0}^{N-1} \exp(-i \frac{2\pi n k}{N} - i \phi_n) = \begin{cases} \sqrt{N} \exp(-i \frac{\pi}{4} + i \phi_k), & \text{if } N \equiv 0 \pmod{2} \\ \sqrt{N} \exp(i \frac{3N+1}{4} \phi_k), & \text{if } N \equiv 1 \pmod{4} \\ \sqrt{N} \exp(-i \frac{\pi}{2} + i \frac{N+1}{4} \phi_k), & \text{if } N \equiv 3 \pmod{4} \end{cases} \quad (4.2)$$

where  $k \in \mathbb{Z}$ . Since Eq. (4.2) is repetitive in  $k$  with period of  $N$ , we will confine the discussion of the integer  $k$  between  $[0, N-1]$ . Note here  $(3N+1)/4$  for  $N \equiv 1 \pmod{4}$  and  $(N+1)/4$  for  $N \equiv 3 \pmod{4}$  are both integers and also coprime with  $N$ . The detailed derivation of Eq. (4.2) from scratch is beyond the scope of this thesis. Instead, we will begin with a lemma called the generalized Landsberg-Schaar identity [115] (Eq. (2.8) in the reference):

$$\sum_{n=0}^{N-1} \exp(-i \pi \frac{n^2 l + n m}{N}) = \sqrt{\frac{N}{L}} \exp(i \pi \frac{m^2 - N l}{4 N l}) \sum_{n=0}^{l-1} \exp(i \pi \frac{n^2 N + n m}{l}) \quad (4.3)$$

where  $m \in \mathbb{Z}$ ,  $N \in \mathbb{N}_+$ ,  $l \in \mathbb{N}_+$ , and  $Nl + m$  needs to be an even number. In the following, we will separately address the three conditions of Eq. (4.2) based on Eq. (4.3).

- $N \equiv 0 \pmod{2}$

When  $N$  is an even number, set  $m = 0$  and  $l = 1$ , so that  $Nl + m = N$  satisfies the even number condition. Substitute these values into Eq. (4.3), we can derive the following identity:

$$\sum_{n=0}^{N-1} \exp(-i \frac{\pi n^2}{N}) = \sqrt{N} \exp(-i \frac{\pi}{4}) \quad (4.4)$$



Therefore the discrete Fourier transform of the Talbot phasors can be calculated:

$$\begin{aligned} \sum_{n=0}^{N-1} \exp(-i \frac{2\pi nk}{N} - i\phi_n) &= \exp(i \frac{\pi k^2}{N}) \sum_{n=0}^{N-1} \exp(-i \frac{\pi(n+k)^2}{N}) \\ &= \sqrt{N} \exp(-i \frac{\pi}{4} + i \frac{\pi k^2}{N}) \end{aligned} \quad (4.5)$$

Note that for an even number  $N$ , the quadratic sums of  $n$  and  $(n+k)$  are the same. As a result, Eq. (4.4) can be used for the second equality of Eq. (4.5).

- $N \equiv 1 \pmod{4}$

When  $N$  is an odd number, let  $m = 2k$  ( $k \in \mathbb{Z}$ ),  $l = 2$  in Eq. (4.3), which also satisfies  $Nl + m = 2N + 2k$  is an even number. We derive that:

$$\sum_{n=0}^{N-1} \exp(-i\pi \frac{2n^2 + 2nk}{N}) = \sqrt{\frac{N}{2}} \exp(i \frac{\pi k^2}{2N} - i \frac{\pi}{4}) \{1 + \exp(i\pi \frac{N+2k}{2})\} \quad (4.6)$$

Here Eq. (4.6) is valid whenever  $N$  is an odd number, so it holds for both  $N \equiv 1 \pmod{4}$  and  $N \equiv 3 \pmod{4}$  cases. When  $N \equiv 1 \pmod{4}$ :

$$1 + \exp(i\pi \frac{N+2k}{2}) = \begin{cases} \frac{1}{\sqrt{2}} \exp(i \frac{\pi}{4}), & \text{if } k \equiv 0 \pmod{2} \\ \frac{1}{\sqrt{2}} \exp(-i \frac{\pi}{4}), & \text{if } k \equiv 1 \pmod{2} \end{cases} \quad (4.7)$$

Also note that:

$$\exp(i \frac{\pi k^2}{N}) = \begin{cases} \exp(i \frac{\pi k^2}{2N} + i \frac{3\pi}{2} k^2), & \text{if } k \equiv 0 \pmod{2} \\ \exp(i \frac{\pi k^2}{2N} + i \frac{3\pi}{2} (k^2 - 1)), & \text{if } k \equiv 1 \pmod{2} \end{cases} \quad (4.8)$$

In Eq. (4.8), we have used the fact that  $k^2$  (or  $k^2 - 1$ ) is divisible by 4 if  $k$  is even (or odd). Substitute Eq. (4.7) and Eq. (4.8) into Eq. (4.6), we can degenerate the two conditions regardless  $k$  is even or odd:

$$\sum_{n=0}^{N-1} \exp(-i\pi \frac{2n^2 + 2nk}{N}) = \sqrt{N} \exp(i \frac{\pi k^2}{2N} + i \frac{3\pi k^2}{2}) = \sqrt{N} \exp(i \frac{3N+1}{4} \frac{2\pi k^2}{N}) \quad (4.9)$$

In this case,  $(3N+1)/4$  is also an integer number, and is coprime with  $N$ . Eq. (4.9) is equivalent to Eq. (4.2) in the condition of  $N \equiv 1 \pmod{4}$ .

- $N \equiv 3 \pmod{4}$

Note that Eq.(4.6) is also valid for  $N \equiv 3 \pmod{4}$ . In this case:

$$1 + \exp(i\pi \frac{N+2k}{2}) = \begin{cases} \frac{1}{\sqrt{2}} \exp(-i\frac{\pi}{4}), & \text{if } k \equiv 0 \pmod{2} \\ \frac{1}{\sqrt{2}} \exp(i\frac{\pi}{4}), & \text{if } k \equiv 1 \pmod{2} \end{cases} \quad (4.10)$$

Similar expression as Eq. (4.8) for  $N \equiv 3 \pmod{4}$  is found:

$$\exp(i\frac{\pi k^2}{N}) = \begin{cases} \exp(i\frac{\pi k^2}{2N} + i\frac{3\pi}{2}k^2), & \text{if } k \equiv 0 \pmod{2} \\ \exp(i\frac{\pi k^2}{2N} + i\frac{3\pi}{2}(k^2 - 1)), & \text{if } k \equiv 1 \pmod{2} \end{cases} \quad (4.11)$$

The odd and even conditions of  $k$  can also be merged into one equation as:

$$\sum_{n=0}^{N-1} \exp(-i\pi \frac{2n^2 + 2nk}{N}) = \sqrt{N} \exp(-i\frac{\pi}{2} + i\frac{\pi k^2}{2N} + i\frac{\pi k^2}{2}) = \sqrt{N} \exp(-i\frac{\pi}{2} + i\frac{N+1}{4} \frac{2\pi k^2}{N}) \quad (4.12)$$

In Eq. (4.12),  $(N+1)/4$  is also an integer and it is easy to prove that it coprimes with  $N$ . Here we have derived Eq. (4.2) in the condition of  $N \equiv 3 \pmod{4}$ .

Overall, Eq. (4.2) is proved by incorporating all three parts above. Indeed, the discrete Fourier transform of the Talbot phasors also gives a sequence of phasors with quadratic phases. By comparing the calculated results with the generalized Talbot phases in Eq. (2.14), we found that  $s=1$  for an even  $N$ ,  $s=(3N+1)/2$  for  $N \equiv 1 \pmod{4}$ , or  $s=(N+1)/2$  for  $N \equiv 3 \pmod{4}$ , respectively. Noticeably, this complies with Eq. (2.15) as well as the parity difference between  $s$  and  $N$ . Eq. (4.2) underpins many Talbot phenomena in space, time, frequency, or even in azimuthal angle as will be presented in this chapter.

### 4.3 Temporal Talbot multiplier based on an optical tapped delay line

The proposed temporal Talbot multiplier is based on a conventional optical TDL structure as sketched in Figure 4.2. It consists of  $N$  parallel delay lines with incremental delay  $T_0$  from 0 to  $(N-1)T_0$ , each embedded with a phase tuning element. We assume the phase shifters  $\varphi_n$  ( $n=0, 1, 2, \dots, N-1$ ) have at least  $2\pi$  phase tuning range. Here the delay  $T_0$  is chosen to be  $1/N$  of the input optical pulse period, while  $N$ -times RRM is always achieved at the output. We suppose that the splitter used at the input and combiner at the output equally splits and collects light with no additional phase relation between the arms: the additional phase in each arm can be compensated through the corresponding phase tuning element without loss of

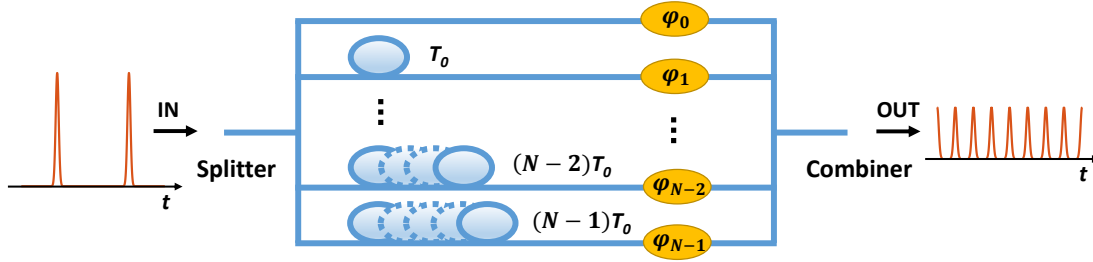


Figure 4.2 – Schematic diagram of the optical tapped delay line (TDL) structure. It is composed of  $N$  parallel arms with incremental delays and phase tuning elements.  $T_0$  is the unit delay time, and  $\varphi_n$  ( $n = 0, 1, 2, \dots, N-1$ ) are the phases applied to phase shifters.

generality. This architecture is well-known and can be integrated, and is indeed a simplified version of the photonic integrated circuits demonstrated in [47, 48], albeit without power control of each arm. The transfer function of such structure is given by:

$$H(f) = \frac{1}{N} \sum_{n=0}^{N-1} \exp(-i2\pi n f T_0 - i\varphi_n) \quad (4.13)$$

Here we have adopted an opposite sign convention of the phases in Eq. (4.13) compared to the equations developed for EO modulation, in order to comply with the publication [159]. But the main results and conclusions remain the same. It can be seen that the TDL response is periodic with a FSR equal to the inverse of the elementary delay, i.e.  $f_{FSR} = 1/T_0$ . Before discussing the temporal Talbot operation of the proposed structure, we first review the well-known spectral amplitude filtering as a comparison.

**Spectral amplitude filtering.** When all the phase shifters are set in-phase, for example  $\varphi_n = 0$  ( $n = 0, 1, 2, \dots, N-1$ ), the filter response becomes a periodic sinc function [48]. This was employed in optical OFDM systems for the demultiplexing of subcarriers [161]. As an example, Figure 4.3 a showcases the power and phase response of the TDL filter when  $N = 8$ . It is clearly seen that the filter suppresses all the frequency components at every  $1/N$  (grey markers) of  $f_{FSR}$ , except the maximum transmission at every integer  $f_{FSR}$  (red markers). Note that the overshoot spikes in the phase response are artifacts at zero amplitudes. Therefore, if a pulsed source with repetition-rate  $f_{FSR}/N$  is sent through the filter, such that the comb lines are aligned to the filter FSR, the comb spacing will be increased by  $N$ -times leading to  $N$ -times RRM. This is shown in Figure 4.3 b. In the simulation, we have used periodic Gaussian pulses as the input pulses, whose FWHM widths correspond to  $1/25$  of the period. The pulse repetition-rate at the output of the filter is multiplied 8-times due to the increased comb line spacing.

**Spectral phase-only filtering.** Spectral phase-only filtering, or temporal Talbot effect, is characterized by RRM in the time domain while maintaining the spectral shape. Now we consider the situation that the phase tuning elements are associated with the Talbot phases, i.e.  $\varphi_n = \phi_n$  ( $n = 0, 1, 2, \dots, N-1$ ), where the actual phases being applied are the residues after

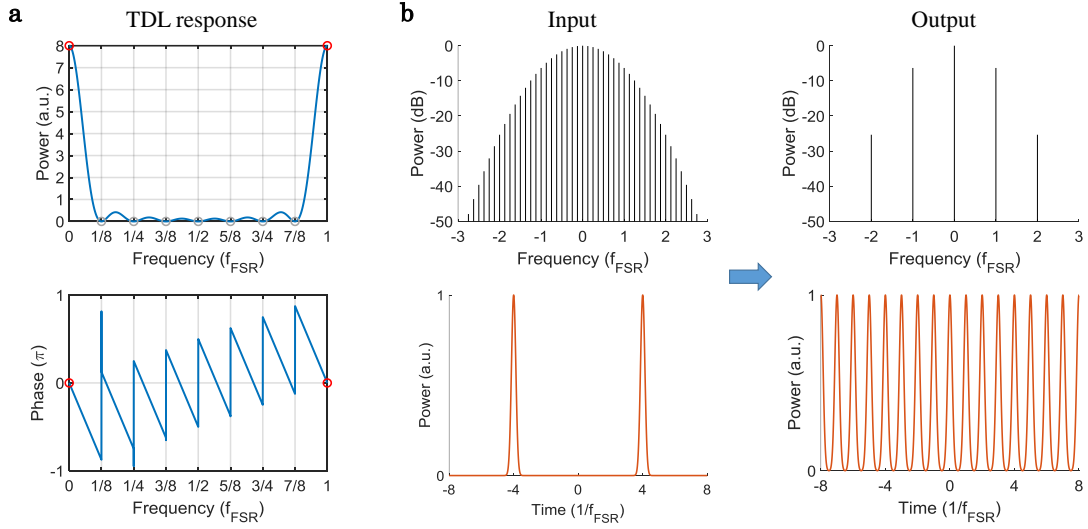


Figure 4.3 – Spectral amplitude filtering operation of the TDL structure for  $N$ -times repetition-rate multiplication (RRM). The phase tuning elements of the TDL are configured all in-phase, i.e.  $(0,0,0,0,0,0,0,0)$ . (a) Power (top) and phase (bottom) response of the TDL structure. (b) Optical spectra (top) and temporal waveforms (bottom) at the input and output the TDL filter. In simulation,  $N = 8$  is used and the FWHM of the input pulse is set to  $1/25$  of its period.  $f_{FSR} = 1/T_0$  is the free spectral range of the device.

modulo  $2\pi$ . When the input comb lines are aligned with the filter FSR, the transfer function at the comb line locations can be found:

$$H(f_k = \frac{k}{NT_0}) = \frac{1}{N} \sum_{n=0}^{N-1} \exp(-i2\pi n f T_0 - i\phi_n) = \frac{1}{\sqrt{N}} \exp(-i\theta + i s_\phi \phi_k) \quad (4.14)$$

where  $f_k = k/NT_0$  are the frequency locations of the input comb lines ( $k$  is the comb index with respect to the center optical carrier). The second equality in Eq. (4.14) is valid due to the property of Talbot phases proven in the identity of Eq. (4.2).  $\theta$  and  $s_\phi$  are respectively a constant phase and an integer multiplicative factor of the Talbot phases. As it has been described in Section 4.2, they respectively correspond to  $\pi/4$  and 1 if  $N$  is even, 0 and  $(3N+1)/4$  if  $N \equiv 1 \pmod{4}$ ,  $\pi/2$  and  $(N+1)/4$  if  $N \equiv 3 \pmod{4}$ .

It can be inferred from Eq. (4.14) that, the TDL filter with Talbot phases creates identical transmissions at the comb line locations. As a result, the shape of the input comb spectrum is preserved. Here the varying part of the TDL filter is the phase response,  $s_\phi \phi_k$ , which complies again with the Talbot phases ( $N$  is even) or multiples of the Talbot phases ( $N$  is odd). As such, in addition to the same transmissions for all the input frequency components, the relative phase response of the filter also fulfills the condition for the temporal Talbot effect therefore resulting in  $N$ -times RRM.

A more straightforward explanation is from the time domain. As discussed in the spectral

amplitude filtering case, the TDL structure with phase shifters tuned all in-phase enlarges the spectral spacing by  $N$ -times. Then if we configure the phase shifters corresponding to the Talbot phases, the spectral Talbot effect would occur, converting the spectrum with increased spacing back to the original shape as the input. This is similar to spectral self-imaging achieved by periodic multi-level Talbot phase modulation of pulse train, through arbitrary waveform generator (AWG) [53, 57, 59]. Here the phase modulation of the pulse trains are implemented through the phase tuning element associated to each copy of the initial pulse train.

Figure 4.4 shows again the case of  $N = 8$  in this regard with the same input pulse train. Here the phase shifters are configured with Talbot phase of  $N = 8$ , i.e.  $(0, \pi/8, \pi/2, 9\pi/8, 0, 9\pi/8, \pi/2, \pi/8)$ . As shown in 4.4 a, the phase response of the filter (red markers in the bottom plot) is again of periodic sequences  $(0, \pi/8, \pi/2, 9\pi/8, 0, 9\pi/8, \pi/2, \pi/8)$  exactly matching the phases required for temporal Talbot effect, together with equal amplitude transmission (red markers in the top plot). Note that  $\theta$  is omitted for illustration purpose here and afterwards, as a constant phase will not change the waveform. The spectra and waveforms at the input and output of the TDL device illustrated in Figure 4.4 b confirm the temporal Talbot operation. That is, the repetition-rate of the pulses is 8-times multiplied, but the spectral shape remains identical to the input spectrum. This is in stark contrast to the spectral amplitude filtering.

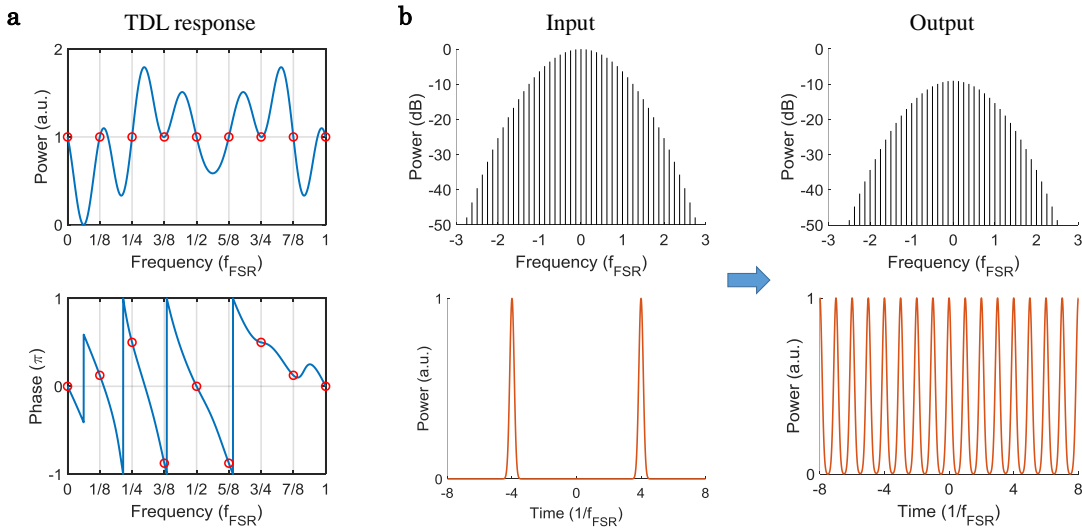


Figure 4.4 – Spectral phase-only filtering (temporal Talbot) operation of the TDL structure for  $N$ -times RRM. The phase tuning elements of the TDL are configured with Talbot phases of  $N = 8$ , i.e.  $(0, \pi/8, \pi/2, 9\pi/8, 0, 9\pi/8, \pi/2, \pi/8)$ . (a) Power (top) and phase (bottom) response of the TDL structure. (b) Optical spectra (top) and temporal waveforms (bottom) at the input and output the TDL filter.

**Combined amplitude and phase filtering.** In addition, the combination of spectral amplitude and phase filtering [162], in between pure amplitude and pure phase-only filtering, can also be realized in the TDL structure enabling the same  $N$ -times RRM. As an illustration, 8-times RRM can be synthesized by combining either 2-times amplitude filtering with 4-times Talbot

effect or 4-times amplitude filtering with 2-times Talbot effect, as shown in Figure 4.5 a and b, respectively. Figure 4.5 a illustrates the case when the phase shifters are configured according to the repeated Talbot phase of  $N = 4$ , i.e.  $(0, \pi/4, \pi, \pi/4, 0, \pi/4, \pi, \pi/4)$ , 2-times amplitude filtering is realized due to 2- times repetition of applied phases to the phase shifters. This is characterized both from the transmission profile (red/grey markers) of the filter response and the doubled comb line spacing at the filter output. Moreover, the phase response at the remaining comb lines follows the periodic Talbot phase relation  $(0, \pi/4, \pi, \pi/4)$ , so that 4-times temporal Talbot effect is achieved simultaneously. As such, 8-times RRM is observed at the output of the filter while the spectrum appears as combs with comb line separation that is only doubled. Similar condition applies to Figure 4.5 b for 8-times RRM, when the phase shifters are configured to repeated Talbot phase sequence of  $N = 2$ , i.e.  $(0, \pi/2, 0, \pi/2, 0, \pi/2, 0, \pi/2)$ . In general,  $N$ -times RRM can be synthesized in the TDL architecture through arbitrary integer factor of  $N$  by spectral amplitude filtering, together with the complementary factor by temporal Talbot effect. The strategy for the phase applied is the same as the example herein.

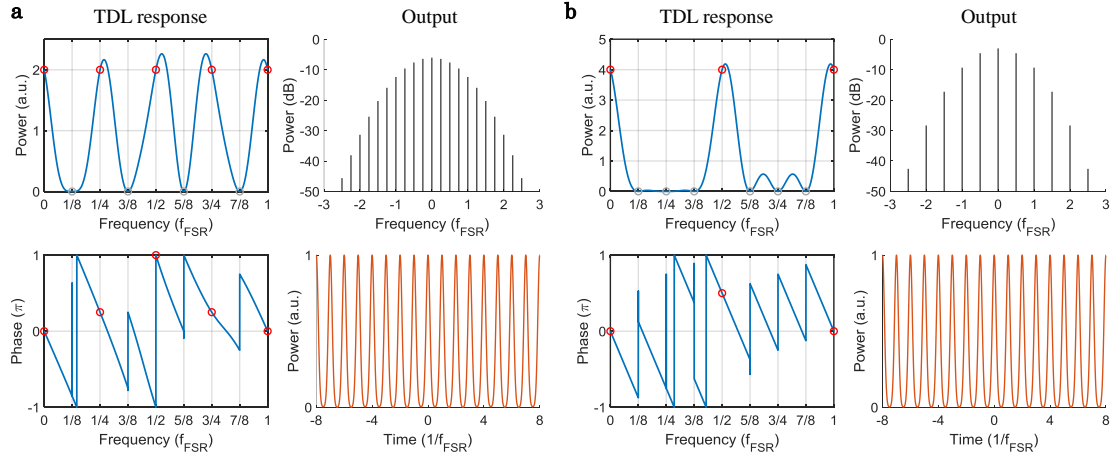


Figure 4.5 – Combined amplitude and phase filtering operation of the TDL structure for  $N$ -times RRM. (a) Power (top) and phase (bottom) response of the TDL and the spectrum (top) and temporal waveform (bottom) at the output of TDL filter, when the phase tuning elements of the TDL are configured with repeated Talbot phases of  $N = 4$ , i.e.  $(0, \pi/4, \pi, \pi/4, 0, \pi/4, \pi, \pi/4)$ . 8-times RRM is achieved by 2-times spectral amplitude filtering and 4-times Talbot effect. (b) Power (top) and phase (bottom) response of the TDL and the spectrum (top) and temporal waveform (bottom) at the output of TDL filter, when the phase tuning elements of the TDL are configured with Talbot phases of  $N = 2$ . 8-times RRM is achieved by 4-times spectral amplitude filtering and 2-times Talbot effect.

**Proof-of-concept verification.** A proof-of-concept test is carried out with a commercial Mach-Zehnder delay line interferometer (DLI), which is functionally equivalent to the proposed structure at  $N = 2$ . The delay time between the two arms of interferometer is fixed at 100 ps i.e.  $f_{FSR} = 10$  GHz, thereby is generally used as demodulator for 10 GHz differential-phase-shift-keying (DPSK) signal. A piezo phase shifter is embedded in one arm to control the phase relation between the two arms of the interferometer. Here we demonstrate that the DLI can be

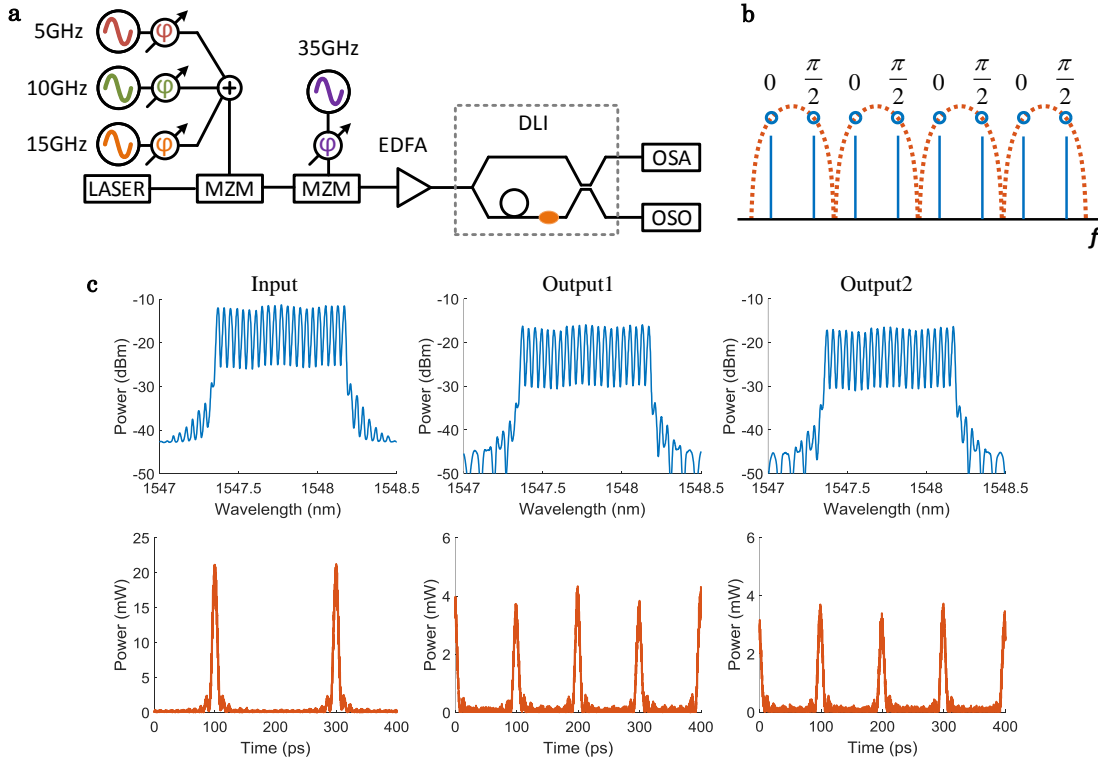


Figure 4.6 – Proof-of-concept verification of the proposed structure ( $N = 2$ ) using a delay line interferometer (DLI). (a) Experimental setup. MZM: Mach-Zehnder modulator; EDFA: erbium-doped fiber amplifier; OSA: optical spectrum analyzer; OSO: optical sampling oscilloscope. Input pulse trains with 5 GHz repetition-rate and 21 comb lines are synthesized based on cascade modulators. The spectra and waveforms of the output pulse trains from the DLI are measured with OSA and OSO. (b) The principle of temporal Talbot operation based on DLI. The orange dashed lines corresponds to the DLI's transfer function, where the blue circles show equal transmission meanwhile periodic  $(0, \pi/2)$  phase response. (c) Optical spectra (top) and temporal waveforms (bottom) measured at the input and two output ports of the DLI.

used to implement the temporal Talbot effect of 5 GHz pulse trains to achieve 2-times RRM.

Figure 4.6 a illustrates the experimental setup. Pulse trains with 5 GHz repetition-rate and 21 comb lines of rectangular shape are generated based on cascaded MZMs, when driven by synchronized RF signals similar to Section 3.3. The spectrum and the waveform of the input pulse trains (Fig. 4.6 c, input) are measured by an optical spectrum analyzer (OSA) and an optical sampling oscilloscope (OSO), respectively. As sketched in Figure 4.6 b, the embedded phase shifter is tuned so that the DLI have equal transmission to all the comb lines, therefore the output spectrum shape will be identical to the input. As described above, an additional periodic  $(0, \pi/2)$  phase profile also exists at these frequency comb locations that gives rise to the temporal Talbot effect. This can be seen from both the two output ports of DLI (Figure 4.6 c, output 1 & output 2): the pulse repetition-rates are doubled in the time domain, while their spectra maintain the original shapes. Indeed, we have confirmed the temporal

Talbot operation in the simplest case of  $N = 2$ . The asymmetrical pulse amplitude in the time domain is mainly attributed to the power imbalance of the used DLI device, or equivalently the extinction ratio of the DLI (nominal 18dB). Besides, the power discrepancy between the input and each of the two outputs is roughly 5 dB, where 2 dB is the nominal insertion loss of the DLI and 3 dB is due to the two outputs with equal power.

**Efficiency and performance analysis.** The efficiency of performing temporal Talbot effect in the proposed TDL structure, however, is not a lossless process due to interference. Suppose the input pulse train is comprised of  $K$  number of comb lines separated by  $f_{FSR}/N$ , the frequency representation of the input signal is given by:

$$E_{in}(f) = \frac{E_0}{\sqrt{K}} \sum_{k=0}^{K-1} a_k \delta(f - f_k) \quad (4.15)$$

where  $a_k$  is the relative amplitude of the  $k$ -th frequency component  $f_k$ . The total power of the input source is  $|E_0|^2 \sum_{k=0}^{K-1} |a_k|^2 / K$ . When the comb lines are aligned with the filter FSR, the TDL output in the Talbot condition can be calculated:

$$E_{out}(f) = E_{in}(f) H(f) = \frac{E_0}{\sqrt{KN}} \sum_{k=0}^{K-1} a_k \exp(-i\theta + i s_\phi \phi_k) \delta(f - f_k) \quad (4.16)$$

where  $\theta$ ,  $s_\phi$  and  $\phi_k$  are the same in Eq. (4.14). The total power at the output of the TDL is therefore  $|E_0|^2 \sum_{k=0}^{K-1} |a_k|^2 / KN$ , which corresponds to  $1/N$  of the input power. As such, the loss scales up for large number RRM by temporal Talbot effect. Nevertheless, this efficiency is similar to performing spectral amplitude filtering in the same structure, where every one out of  $N$  frequency components are selected.

If  $N \times N$  discrete Fourier transform network [163] is installed as the output coupler,  $N$  temporal Talbot RRM pulse trains can be accessed simultaneously. In fact, such  $N \times N$  network has been utilized in spectral amplitude filtering to direct different frequency spectra to different ports, hence outputs  $N$  optical pulse trains with  $N$ -times RRM. Similarly, the incremental linear phase imposed by the discrete Fourier transform network for each output port would incrementally shift the Talbot pulse train by  $1/T_0$  in time domain. Thus, all the  $N$  output pulse trains are time-translated replica of initial Talbot pulse train. When all these Talbot pulse trains are considered as a whole, the optical power is conserved. This is experimentally shown above in the case of  $N = 2$ . Both outputs of the DLI exhibit 2-times Talbot pulse train, making the overall structure in principle lossless if insertion loss is subtracted.

As seen from the output waveforms of the DLI, they deviate from ideal temporal Talbot effect. To assess the performance of the TDL-based temporal Talbot multiplier, we evaluate the possible degradation due to the power imbalance and delay line length inaccuracy of the structure. The power imbalance arises from both input and output couplers, as well as the unequal loss in the arms due to the delay line length difference. Additional tunable Mach-Zehnder couplers [48] or variable in-line attenuators can be adopted in the structure to tackle the imbalance.



This would be necessary to improve the performance of temporal Talbot effect for sub-GHz pulse train, as power imbalance increases with the delay line length difference. Another factor that would degrade the performance is the delay line length inaccuracy. The filter response is no longer periodic in this scenario. It is worth to mention that when the applied phases also account for the phases induced by the length inaccuracy, the filter response around the center frequency will still be close to ideal shape [164]. Nevertheless, the degradation would inevitably be severe for input pulse trains with broader bandwidth. Unlike the power imbalance which causes the Talbot-multiplied pulses to be of unequal amplitudes, the inaccuracy of delay length mainly results in the output spectrum deviating from the input spectral shape.

Compared to its SLM-based pulse shaper counterpart, the proposed multiplier features several advantages in terms of temporal Talbot implementation. The method benefits from the periodic nature of its transfer function, thereby eliminating the use of SLM to apply periodic Talbot phase. And it is particularly appealing to multiply relatively low repetition-rate (sub-GHz) pulse train, which is not easily accessible by 4-f pulse shaper of limited spectral resolution. Most importantly, while 4-f pulse shaper is generally bulky, the structure is ready to be integrated to all kinds of platforms in a simple and compact manner. Compared to the LCFBG, the TDL structure benefits from the flexible spectral amplitude and phase shaping. Also the working bandwidth of the proposed structure is generally larger than the LCFBG. Nevertheless, loss is intrinsic to the proposed multiplier as well as the potential degradation discussed above. Overall, it provides a complementary approach to implement temporal Talbot RRM which is amenable to photonic integration.

#### 4.4 Azimuthal Talbot effect based on orbital angular momentum beams

In this section, we demonstrate the self-imaging of azimuthal petals based on OAM modes when superimposed with Talbot phases. First, we briefly discuss the basis of OAM of light, and we draw close analogy between OAM mode and frequency comb mode, as well as between azimuthal angle and time domain. Given the existence of temporal Talbot effect, similar phenomenon is likely to occur in the azimuthal domain, i.e. the azimuthal Talbot effect. We experimentally demonstrate such self-imaging effect using a series of superimposed OAM modes, with experimental results in good agreement with simulation. The azimuthal Talbot effect may offer more flexibility for various OAM-involved applications, such as particle manipulation, laser inscription, quantum optics, and space-division multiplexing (SDM) optical communication.

Optical angular momenta can be classified into two types: spin angular momentum (SAM) and orbital angular momentum (OAM). SAM is linked to the circular polarization state of light field, and is found to carry additional  $\pm\hbar$  of angular momentum per photon with respect to linear polarization state, where  $\hbar$  is the reduced Planck constant and the sign distinguishes the left or right circular polarization [74]. OAM is associated to the helical phase structure

of light wavefront. Figure 4.7 shows the wavefronts (top) and cross-section phase profiles (bottom) of a number of OAM states of light. Mathematically, the OAM phase is characterized by  $\exp(il\Phi)$  in the cylindrical coordinate, where  $\Phi$  is the azimuthal angle around the beam center and  $l$  is known as the topological charge of the optical vortex. Compared to plane wave, OAM state also carries additional angular momentum of  $l\hbar$  per photon. Note that the topological charge  $l$  and thereby the angular momentum  $l\hbar$  are also quantized. In fact, fractional OAM state can be viewed as superposition of a number of integer OAM modes by Fourier series [165]. The helical structure of light wavefront has attracted significant research attention and found many applications in particle manipulation [166], quantum optics [167], optical communication [168], sensing [77], and super-resolution microscopy [169].

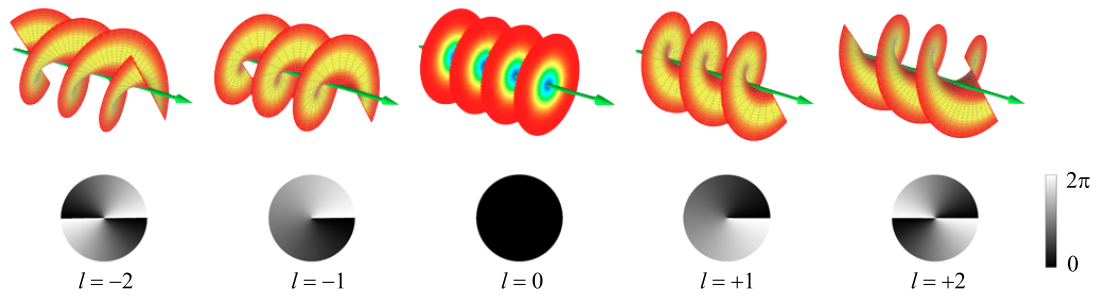


Figure 4.7 – Schematics of orbital angular momentum (OAM) modes of light. Helical phase fronts (top) and phase profiles at the cross-sections (bottom) of OAM modes are shown, with topological charges from  $l = -2$  to  $2$ . Note that  $l = 0$  corresponds to the plane wave of a Gaussian beam. The phase fronts are adapted from Wikipedia.

**Concept of azimuthal Talbot effect.** Notably, the mathematical expression of OAM mode as well as its discrete nature shares high similarity with optical frequency comb mode. That is, a number of OAM modes superimposed with Talbot phases may also give rise to the self-imaging in the azimuthal angle. However, unlike in the case of temporal Talbot effect which typically relies on dispersive propagation to obtain quadratic phase, there is no such dispersive counterpart in the azimuthal angle. Indeed for a beam propagating in free space, the diffraction only occurs in the radial direction. Here we adopt the method by directly associating the Talbot phase with each OAM mode, similar to implementing the temporal RRM using a pulse shaper [56]. Consider a number of consecutive OAM modes with topological charges from  $-M$  to  $M$  ( $2M + 1$  in total), and the superposition of OAM modes is given by:

$$E(r, \Phi) = \sum_{l=-M}^M A_l(r) \exp(il\Phi + i\varphi_l) \quad (4.17)$$

where  $A_l(r)$ , and  $\varphi_l$  are the amplitude and initial phase associated with  $l$ -th order OAM mode, respectively. It is clearly seen from Eq. 4.17 that the expression of superimposed OAM modes is alike a number of comb modes with different amplitudes and initial phases. Therefore, when these OAM modes are of equal amplitudes and in-phase ( $\varphi_l = 0$ ,  $l = -M, \dots, M$ ), there will be a

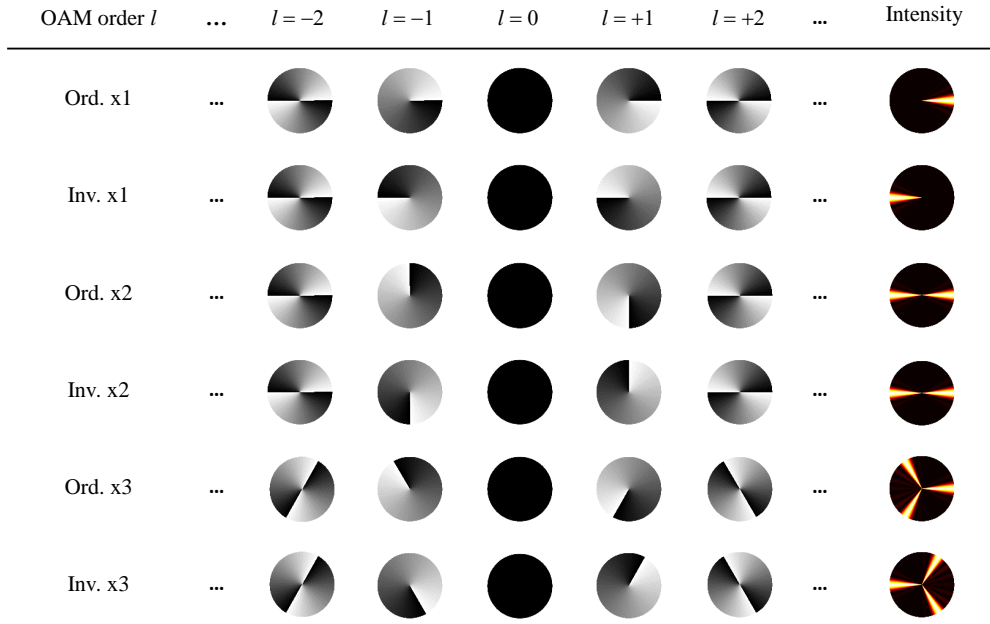


Figure 4.8 – Concept of azimuthal Talbot effect. When the OAM modes are superimposed with Talbot phases, intensity self-images occur in the azimuthal angle. The last column shows the intensity profile corresponding to the summation of all the OAM modes in each row (topological charges from  $-10$  to  $10$  are used in the simulation while only  $-2$  to  $2$  are shown). Ordinary (Ord.) and inverted (Inv.) with integer ( $\times 1$ ) and fractional ( $\times 2$  and  $\times 3$ ) Talbot effects are illustrated.

single sinc-shaped petal generated in the azimuthal angle (Figure 4.8, Ord.  $\times 1$ ). Moreover, the position of the petal can be modified by applying linear phases to the OAM modes, where the translation in azimuthal angle is given by the linear phase slope. A specific example is when the initial phases of adjacent OAM modes are  $\pi$  out-of-phase. In this case, the sinc-shaped petal is also  $\pi$  shifted, which corresponds to the inverted pattern of the initial petal (Figure 4.8, Inv.  $\times 1$ ). These two conditions actually represent respectively the ordinary integer Talbot and the inverted integer Talbot [52]. More interesting situation comes when the initial phases of the OAM modes are the Talbot phases as defined in Eq. (4.1), i.e.  $\varphi_l = \phi_l$ . For instance,  $N = 2$  and  $N = 3$  of Eq. (4.1) gives the periodic Talbot phases as  $(0, \pi/2)$  and  $(0, 2\pi/3, 2\pi/3)$ , respectively. When applying these periodic phase sequences to the OAM modes, the single intensity petal will get self-imaged in the azimuthal angle by 2 or 3-times (Figure 4.8, Ord.  $\times 2$  & Ord.  $\times 3$ ). This corresponds to the fractional Talbot images in the Talbot carpet, and is analogous to temporal Talbot effect that achieves 2 or 3-times RRM. For all the inverted cases of Figure 4.8, additional alternating  $(0, \pi)$  phase sequences are added on top of the ordinary Talbot phases. In the Talbot carpet, they correspond to the half-period shifted fractional Talbot images. While in the context of azimuthal angle, half-period is  $\pi$  and it is just the image inversion.

**Experimental demonstration of azimuthal Talbot effect.** The experiment setup to implement azimuthal Talbot effect is shown in Figure 4.9. We synthesize the superposition of a series of OAM modes based on a 2D phase-only SLM and an optical  $4-f$  system. The technique to encode complex amplitude modulation via such setup is described in Section. 2.2. The  $4-f$  imaging system incorporates a SLM in its input plane, a camera in its output plane, and an iris placed in its Fourier plane. Two identical lenses with focal lengths  $f = 15$  cm are used in the  $4-f$  system. In the experiment, a linear phase ramp is added in addition to the calculated hologram to separate encoded field from reflection, while preserving the amplitude images recorded at the camera [102]. As a result, although the  $4-f$  system is aligned based on the reflection from the SLM (red dashed line), the iris is displaced and selects the diffracted light. Note that the iris here not only blocks out the unmodulated light, but also filters out higher-order diffraction orders to achieve complex amplitude modulation [104]. A CW laser at telecom wavelength is attenuated by an in-line attenuator to avoid saturation at the camera, and passed through a polarization controller to maximize the SLM modulation efficiency. The light beam is then collimated to 3.6 mm diameter and sent to the  $4-f$  system described above.

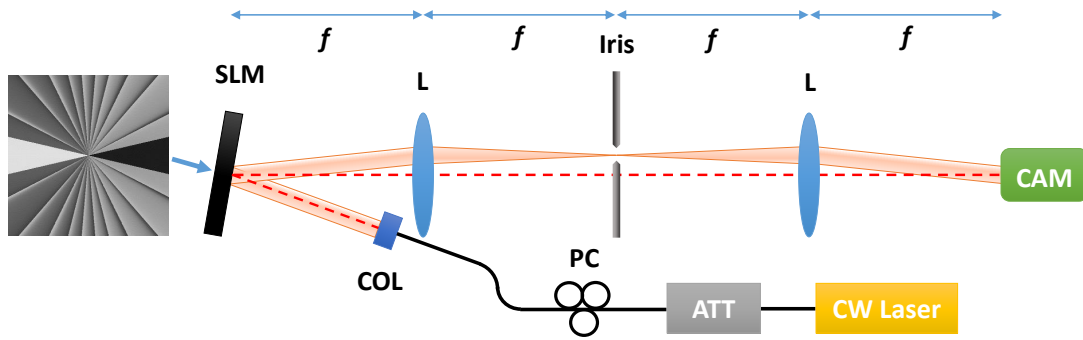


Figure 4.9 – Experimental setup for the demonstration of azimuthal Talbot effect. ATT: attenuator; PC: polarization controller; COL: collimator; SLM: spatial light modulator; L: lens; CAM: camera;  $f$ : focal length. The setup consists of an optical  $4-f$  system to encode superposition of OAM modes, with a SLM in its input plane, an iris in its Fourier plane, and a camera in its output plane. The SLM is loaded with target phase pattern (the image corresponds to the 2-times azimuthal Talbot effect), and is illuminated by a collimated laser beam.

Figure 4.10 shows the experimental and simulated images of azimuthal self-imaging. Noticeably for a  $4-f$  imaging system, the output image is an inverted replica of the input. Thus, all the ordinary (inverted) Talbot images taken at the output plane of the  $4-f$  system show intensity peaks aligned at negative (positive) x-axis. In both experiment and simulation, we use OAM topological charge orders from  $-10$  to  $10$  with equal amplitudes. The results for ordinary integer and inverted integer (obtained when neighboring OAM modes are  $\pi$  out of phase) are shown in Figure 4.10 a and d, respectively. When proper Talbot phases defined by Eq. (4.1) are applied, the doubling and tripling of the azimuthal intensity repetition-rate are clearly observed in Figure 4.10 b and c. Figure 4.10 e and f are the inverted replica of Figure 4.10 b and c with additional periodically alternating  $(0, \pi)$  phases. All of the azimuthal Talbot

images correspond to specific planes in a Talbot carpet.

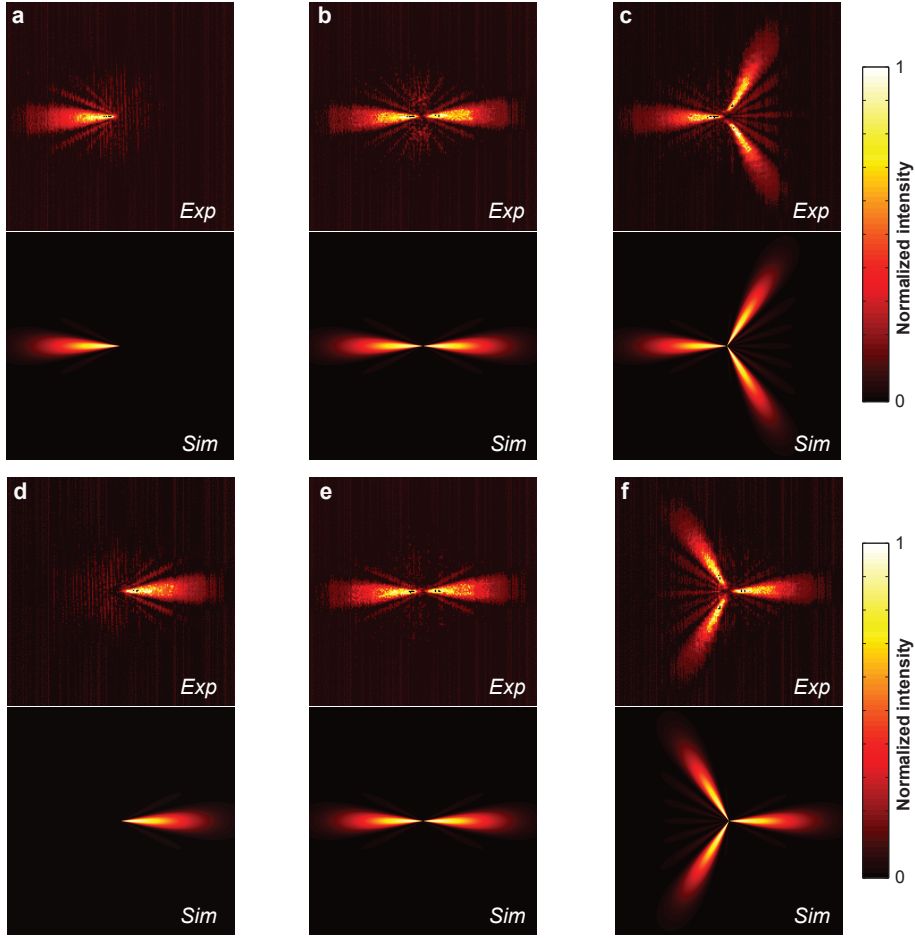


Figure 4.10 – Experiment and simulation images of azimuthal Talbot effect. The OAM modes used in the experiment and simulation are ordered from  $-10$  to  $10$  of equal amplitudes. Ordinary (a) integer Talbot ( $\times 1$ ): OAM modes all in-phase; (b) fractional Talbot ( $\times 2$ ): OAM modes with periodic  $(0, \pi/2)$  phases; (c) fractional Talbot ( $\times 3$ ): OAM modes with periodic  $(0, 2\pi/3, 2\pi/3)$  phases. Inverted (d) integer Talbot ( $\times 1$ ): OAM modes with periodic  $(0, \pi)$  phases; (e) fractional Talbot ( $\times 2$ ): OAM modes with periodic  $(0, 3\pi/2)$  phases; (f) fractional Talbot ( $\times 3$ ): OAM modes with periodic  $(0, 5\pi/3, 2\pi/3, \pi, 2\pi/3, 5\pi/3)$  phases.

In order to have a better comparison between experiment and simulation results, we extract the azimuthal intensity of the experimental images in the case of inverted Talbot effect. The experimental azimuthal intensity profile is obtained by first positioning a narrow donut ring of interest around the origin of the beam, and then mapping the azimuthal angle and the light intensity of all the pixels inside the ring. Finally, all the azimuthal angle and intensity pairs are unwrapped in a  $(-\pi, \pi)$  plot, as well as being normalized. The azimuthal intensity profiles of the experimental images of Figure 4.10 d, e, and f are extracted as in Figure 4.11. The extracted azimuthal intensity distributions are in reasonably good agreement with the

simulation. The self-imaged petals are indeed aligned with simulation results, and even the sidelobes are visible due to the rectangular shape of the constituting OAM spectra. The noise background observed in the experimental images is mainly attributed to the imperfection of the camera being used, which shows a time-changing noise floor even without input light. As such, the contrast between peaks and sidelobes of experimental images is degraded after normalization, when compared to numerical results.

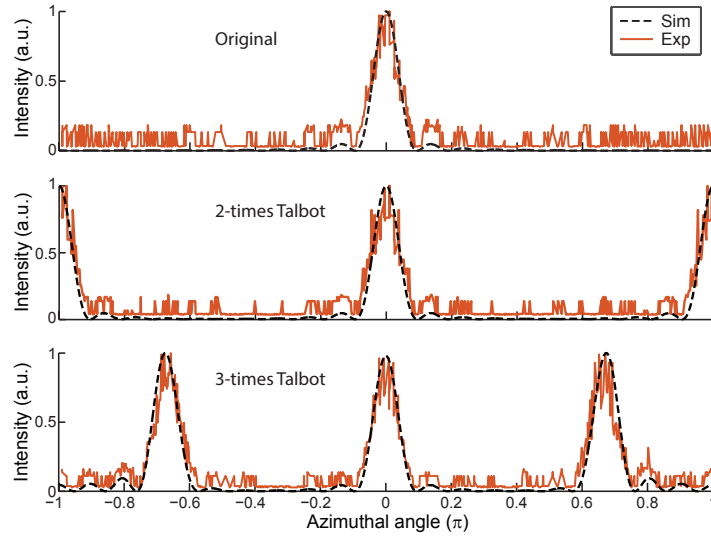


Figure 4.11 – Extracted azimuthal intensity profiles of inverted Talbot images. From top to bottom: original (integer Talbot), 2–times azimuthal Talbot, and 2–times azimuthal Talbot. Orange: experiment; dashed black: simulation.

**Azimuthal Talbot effect of Gaussian-apodized OAM spectrum.** The petal shapes can also be structured by tailoring the amplitude profiles of the OAM modes. When the OAM spectrum is Gaussian-apodized, the corresponding azimuthal petal will also be Gaussian-shaped. This is analogous to its time-domain counterpart: a transform-limited Gaussian pulse also corresponds to a Gaussian-shaped frequency spectrum. The experiment and simulation images of azimuthal intensity RRM using Gaussian-apodized OAM spectra are shown in Figure 4.11. By using a Gaussian-apodized OAM spectrum ordered from  $-10$  to  $10$ , 2-times (Figure 4.11 b) and 3-times (Figure 4.11 c) azimuthal self-imaging can be realized by adapting Talbot phase to the spectrum (Figure 4.11 c). As expected, less sidelobes and broadening of the petal angular occupancy are observed compared to a rectangular OAM spectrum, confirmed by both experiment the simulation results. Higher multiplication factors can be obtained when increasing the number of OAM orders as illustrated in Figure 4.11 d-f. Gaussian-shaped OAM spectra ordered from  $-20$  to  $20$  are combined with appropriate Talbot phases in order to reach a 10, 11, 12-fold azimuthal Talbot RRM.

**Azimuthal Talbot effect of Laguerre-Gaussian modes.** A widely used set of beams carrying OAM is the Laguerre–Gaussian (LG) beam. The LG beam is characterized not only by the azimuthal index, but also the radial index that corresponds to the number of nodes in the



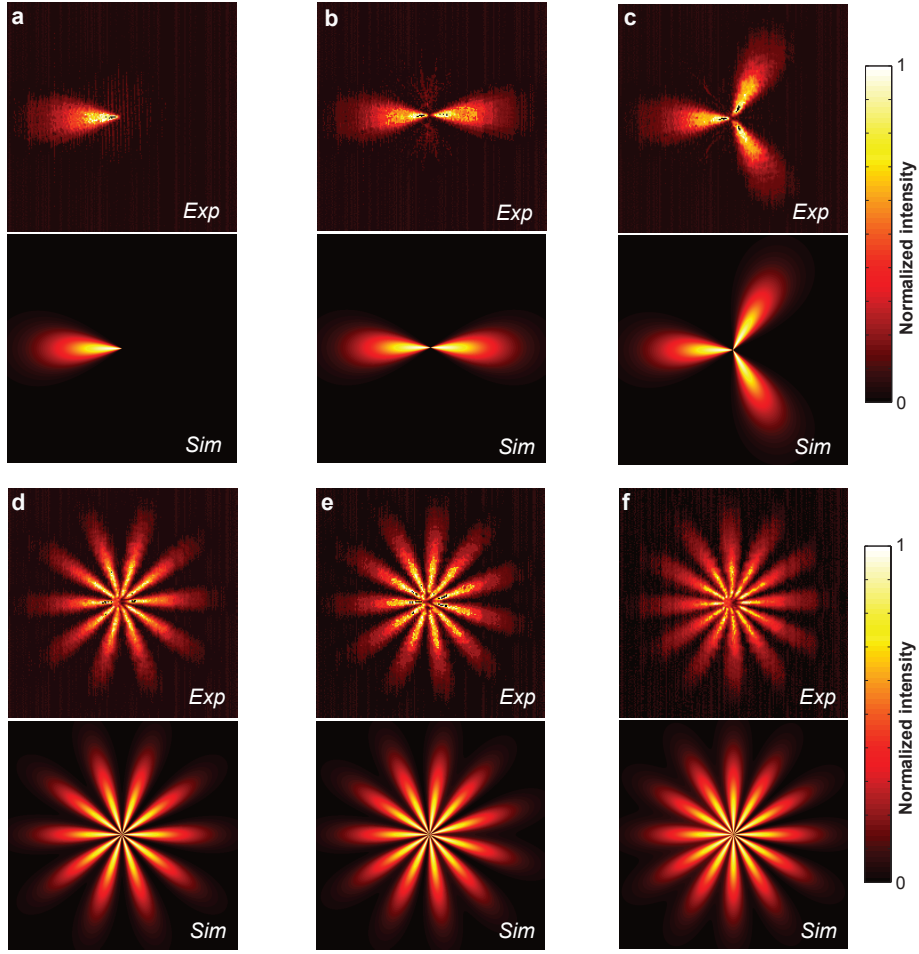


Figure 4.12 – Experiment and simulation images of azimuthal Talbot effect with Gaussian-apodized OAM spectrum. OAM modes ordered from  $-10$  to  $10$  with Gaussian apodization for (a) integer Talbot ( $\times 1$ ) (b) fractional Talbot ( $\times 2$ ) (c) fractional Talbot ( $\times 3$ ) in the azimuthal angle. OAM modes ordered from  $-20$  to  $20$  with Gaussian apodization for (d) fractional Talbot ( $\times 10$ ) (e) fractional Talbot ( $\times 11$ ) (f) fractional Talbot ( $\times 12$ ) in the azimuthal angle.

radial axis [74]. Here, we also demonstrate the azimuthal Talbot effect for a number of LG beams of the same radial indices but different topological charges, given the full amplitude and phase control of our setup. In the experiment, the laser beam is collimated to a larger size (7 mm diameter) to approximate uniform illumination. Similar to previous conditions, Talbot phases are associated with the topological charges for the azimuthal Talbot effect. Figure 4.13 shows the corresponding experimental and numerical results of superimposed LG modes with the same radial indices. LG modes with radial indices of 0 and topological charges from  $-10$  to  $10$  of equal weights are shown in Figure 4.13 a-c. For such LG modes, they only have one nodal rings, while the size of hollow center enlarges with an increasing topological charge. Therefore, the resulting Talbot images are qualitatively similar to images implemented from pure OAM

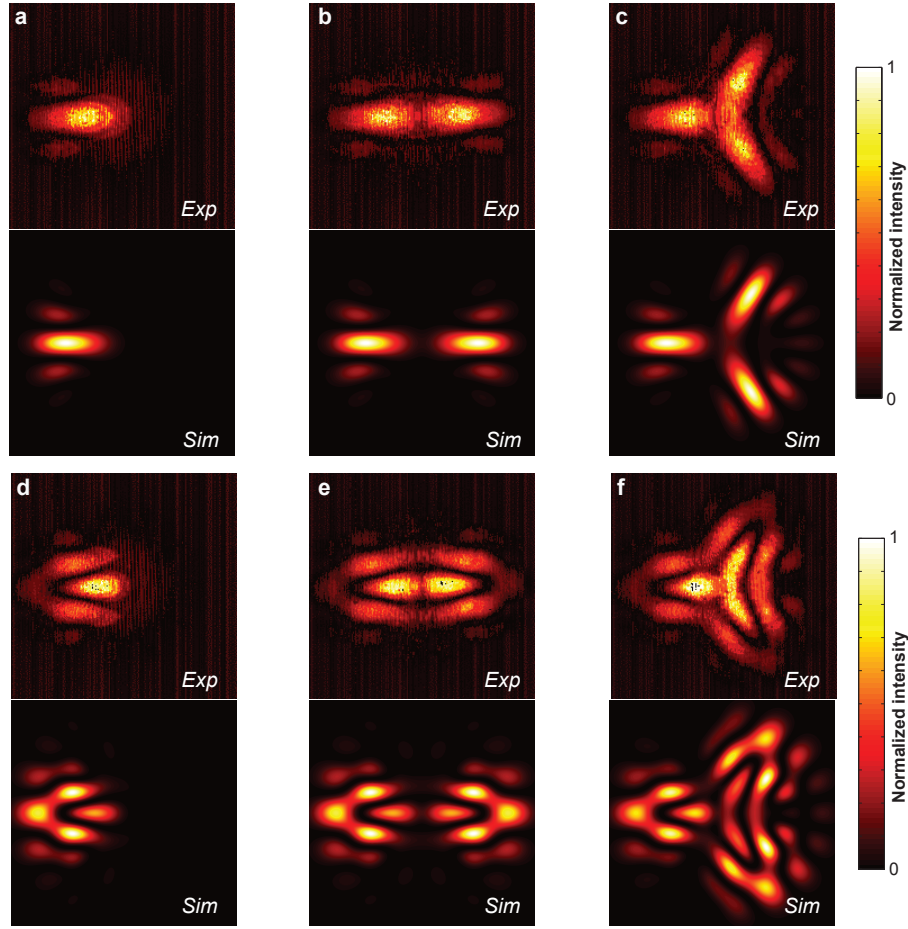


Figure 4.13 – Experiment and simulation images of azimuthal Talbot effect of Laguerre-Gaussian (LG) modes. LG modes with radial index of 0 and azimuthal indices ordered from  $-10$  to  $10$  for (a) integer Talbot ( $\times 1$ ) (b) fractional Talbot ( $\times 2$ ) (c) fractional Talbot ( $\times 3$ ) in the azimuthal angle. LG modes with radial index of 1 and azimuthal indices ordered from  $-10$  to  $10$  for (d) integer Talbot ( $\times 1$ ) (e) fractional Talbot ( $\times 2$ ) (f) fractional Talbot ( $\times 3$ ) in the azimuthal angle.

phases. LG modes with radial indices of 1 and topological charges from  $-10$  to  $10$  of equal weights are displayed in Figure 4.13 d-f. We can see that in Figure 4.13 d the initial intensity petal breaks down in the middle. This can be attributed to the interference from different azimuthal modes of different nodal ring orders. Nevertheless, the azimuthal intensity RRM is still manifested according to the applied Talbot phases. The discrepancy between experiment and simulation images, with experiment images attenuated in the periphery and intensified in the center, is mainly due to the nonuniform illumination of the input Gaussian spatial profile.

It is worth to mention that the results presented in this section demonstrate the azimuthal self-imaging at the generation stage. While the external Talbot phase shaping of an existing OAM spectrum is possibly be implemented in the Fourier plane [170]. The OAM beams after Fourier



transforms [171] or mode sorters [172] map the OAM orders into a series of spatially-resolved concentric rings or different locations in a spatial axis, respectively. In this regard, the Talbot phases can be easily associated with the OAM modes using a phase-only SLM. The technique is analogous to using Fourier-domain pulse shaping for temporal Talbot implementation [56]. This may offer substantial interest for classical and quantum information processing when OAM mode is used as the basis.

## 4.5 Conclusions

In summary, a novel temporal Talbot multiplier is proposed based on optical TDL structure, which is conventionally used for spectral amplitude filtering. We demonstrate that, temporal Talbot effect and versatile combined amplitude and phase filtering can be synthesized in such an architecture, all leading to the same RRM factor. The working principle is theoretically derived and numerically simulated, also confirmed by a proof-of-concept experiment. In addition, we evaluate the efficiency and potential performance degradation of the proposed temporal Talbot multiplier.

Also, the azimuthal Talbot effect based on the interference of OAM modes is demonstrated. Various Talbot conditions from ordinary to inverted azimuthal self-images are demonstrated, as well as achieving high petal multiplication factor. The close analogy between the azimuthal and temporal Talbot intensity RRM is discussed. In addition, the azimuthal self-imaging in the scenarios of Gaussian-apodized OAM spectrum and LG beam is also investigated. The finding of azimuthal Talbot effect implies the duality between OAM mode and frequency comb mode. Therefore, the shaping techniques of frequency combs may be borrowed for the processing of OAM spectra, or vice versa.

## 5 Soliton microcomb based RF photonic filters

The content in this chapter is based on the following publication:

- **J. Hu**, J. He, J. Liu, A. S. Raja, M. Karpov, A. Lukashchuk, T. J. Kippenberg, and C.-S. Brès, "Reconfigurable radiofrequency filters based on versatile soliton microcombs," *Nature Communications*, **11**, 4377 (2020). [173]

The microresonators used in this study are fabricated by Junqiu Liu and characterized by Jijun He. Jijun He also carried out part of the experiment and simulation in this work.

### 5.1 Introduction

Thanks to the ever-maturing photonic integration, RF photonic systems and subsystems have been brought to new height [87, 174], in terms of footprint, scalability, and potentially cost-effectiveness. Particularly, RF filtering at the chip-scale is a key enabling function [91]. Paradigm demonstrations include the integration of the basic filtering blocks, such as delay lines [175], optical spectral shaper [46], programmable mesh topologies [176], ring resonators [93], as well as the use of stimulated Brillouin scattering in waveguides [177]. Recently, an all-integrated RF photonic filter has been shown in a monolithic platform [178]. In addition to these approaches, RF filters can also be constructed based on multi-wavelength sources and dispersive propagation [37, 80]. For such RF photonic filters, each optical wavelength is equivalent to the filter tap of a TDL filter, while the differential delay is given by a common dispersive element. The single dispersive delay line greatly simplifies the structure complexity of a TDL filter. Nevertheless, the main complexity is then shifted to the multi-wavelength source. EO combs [37, 80], MLLs [179, 180], or laser banks [175] are generally adopted as light sources, which remain expensive and bulky options.

Integrated microcombs have appeared as an interesting alternative for comb-based RF photonic filters [81–83]. It is worth to mention that, besides filtering RF signals, microcombs have been used in other various RF photonic functions, such as true-time delay beamforming [181],

RF channelizer [182], and analog computation [183]. In regards to microcomb-based RF filters, the large comb line spacing of microcombs also enhances RF filters with broader Nyquist zone (spur free range), lower latency [81], less dispersion induced fading, as well as larger number counts of equivalent delay lines [82], unparalleled by other approaches. However, so far all these microcomb-based RF filters have been implemented on either dark pulses [81, 136] or complex soliton crystal states [82, 83]. Additional programmable pulse shaping modules are inevitably required to equalize or smooth the comb spectral shape. Thus, the system complexity is significantly increased while the potential for low-cost and compactness of such RF filters is compromised.

We demonstrate soliton-based RF photonic filters without any external shaping. In addition, the synthesized RF filters can be all-optically reconfigured through the internal shaping of versatile soliton states. Specifically, we trigger, in a deterministic fashion, the perfect soliton crystals (PSC) to multiply the comb line spacing [62, 184], thereby dividing the RF passband frequencies. Moreover, we achieve filter reconfiguration based on versatile two-soliton microcombs (TSM). The spectral interference of two solitons is functionally equivalent to an interferometric setup, shifting the filter passband frequency via modification of the angle between them. The internal exploitation of abundant and regulated soliton formats of a microresonator effectively bypasses external pulse shaping, which is required previously to obtain RF filters with good suppression ratio and reconfigurability.

In this chapter, I will present the results regarding the internal shaping of soliton microcombs for reconfigurable RF photonic filters. Section 5.2 describes the conceptual setup of soliton-based RF filters and formulates the RF filter responses of various soliton states. Section 5.3 elaborates the excitation approaches of versatile soliton states and the characterization of the microresonator chip being used. Section 5.4 details the reconfigurable RF photonic filters based on these soliton states, together with a proof-of-concept system demonstration. Section 5.5 compares the performances of our filters with other comb-based RF filters, and a simple link optimization of our RF filter is also provided.

## 5.2 Principle of operation

The working principle of comb-based RF photonic filters has been detailed in Section 3.4. In terms of the current implementation, the conceptual diagram is depicted in Figure 5.1. Firstly, a tunable C-band CW laser initiates soliton microcomb generation. As before, the comb lines serve as the filter taps for the TDL RF photonic filter. By modulating the RF signals from a VNA on MZM, the RF signals are broadcast to each microcomb mode. Then the upconverted signals are propagated through a spool of SMF to acquire incremental delays between the filter taps. Finally, the signals are converted back to the RF domain in a fast PD. The overall setup of microcomb-based RF filter is slightly different from the one based on EO combs. Apart from the difference in the comb source, MZM is used here instead of DP-MZM for RF modulation, and also SMF is used instead of DCF for dispersive propagation.

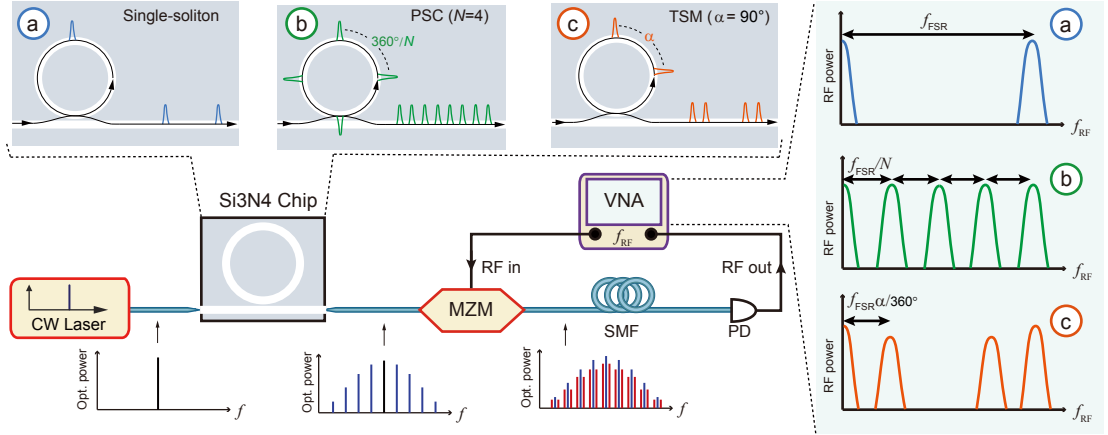


Figure 5.1 – Schematic diagram of versatile soliton-based RF photonic filters. The conceptual setup consists of four parts: microcomb generation, RF signal upconversion, dispersive propagation, and photodetection. MZM: Mach-Zehnder modulator; SMF: single-mode fiber; PD: photodiode; VNA: vector network analyzer. Reconfigurable RF filters are synthesized based on versatile soliton microcombs. (a) Single-soliton RF filter with passband centered at  $f_{FSR}$  (blue). (b)  $N$ – perfect soliton crystals (PSC) RF filters with passband centered at  $f_{FSR}/N$  (green,  $N = 4$  is shown); (c) Two-soliton microcomb (TSM) RF filters with passband centered at  $f_{FSR}\alpha/360^\circ$  (orange), where  $\alpha$  is the relative azimuthal angle between two solitons ( $\alpha = 90^\circ$  is shown).

**RF filter responses of versatile soliton states.** Recall that the comb-based RF filters can be described by the discrete Fourier transform of the frequency comb intensity:

$$H(f_{RF}) \sim \cos(2\pi^2 \Theta_2 f_{RF}^2) \sum_k |a_k|^2 \exp(i4\pi^2 \Theta_2 k \Delta f f_{RF}) \quad (5.1)$$

where  $|a_k|^2$  denotes the power of each comb line,  $\Theta_2 = -\beta_2 L$  is the product of the second-order dispersion  $\beta_2$  of the dispersive element and its length  $L$ , and  $\Delta f$  is the comb line spacing.  $f_{FSR} = 1/2\pi\Theta_2\Delta f$  is the FSR of the RF filters. The definitions of the parameters are the same as in Eq. (3.17). While for Eq. 5.1, an amplitude modulation term replaces the quadratic phase term of Eq. (3.17), as here the simple double-sideband (DSB) modulation based on MZM is used [155]. Thanks to the large comb line spacing of microcombs, the required accumulated dispersion  $\Theta_2$  is much less to achieve similar  $f_{FSR}$ . This makes the amount of dispersion within reach via an integrated delay element [175]. Moreover, in this condition, the power fading resulting from the amplitude modulation ( $\cos(2\pi^2 \Theta_2 f_{RF}^2)$  term of Eq. (5.1)) is also minimized for small  $\Theta_2$ . Note that the simple RF modulation via MZM bypasses the need of complex modulator structure (DP-MZM) and a broadband electrical  $90^\circ$  hybrid.

The exact RF filter responses are obtained by substituting the microcomb spectral profile into

Eq. (5.1). For single-soliton microcomb, the optical field is given by:

$$E(t) \sim \text{sech}\left(\frac{t}{T_s}\right) \otimes \sum_{n=-\infty}^{\infty} \delta(t - nT) \quad (5.2)$$

where  $T_s$  and  $T = 1/\Delta f$  are the soliton pulse width and period, respectively.  $\delta(t - nT)$  is the Dirac function and sech is the hyperbolic secant function of soliton pulse shape. Taking the Fourier transform of Eq. (5.2), the single soliton spectrum is derived as:

$$\tilde{E}(f) \sim \text{sech}(\pi^2 T_s f) \sum_{k=-\infty}^{\infty} \delta(f - k\Delta f) \quad (5.3)$$

where  $f$  is the frequency offset between the comb mode and pump mode. This leads to the power of each comb line, or equivalently the filter tap weights, being  $|a_k|^2 \sim \text{sech}^2(\pi^2 k T_s / T)$ .  $k \in \mathbb{Z}$  is the mode index with respect to the center comb line. Disregarding the envelope term of Eq. (5.1) for the moment, we can rewrite the summation part using Poisson summation formula:

$$\sum_{k=-\infty}^{\infty} |a_k|^2 \exp(i2\pi k \frac{f_{RF}}{f_{FSR}}) = f_{FSR} P(f_{RF}) \otimes \sum_{n=-\infty}^{\infty} \delta(f_{RF} - n f_{FSR}) \quad (5.4)$$

where  $P(f_{RF})$  is the Fourier transform of the generalized form of  $|a_k|^2$ , at which the mode index  $k$  is substituted by an arbitrary variable  $x$ , times a factor  $f_{FSR}$ :

$$P(f_{RF}) = \int \text{sech}^2\left(\frac{\pi^2}{T_s f_{FSR}} T x\right) \exp(i2\pi f_{RF} x) dx \sim \frac{2 \frac{T}{T_s} \frac{f_{RF}}{f_{FSR}}}{\sinh\left(\frac{T}{T_s} \frac{f_{RF}}{f_{FSR}}\right)} \equiv G(f_{RF}) \quad (5.5)$$

where the Fourier transform of sech-squared function can be analytical calculated using the residue theorem [185], and is defined as  $G(f_{RF})$ . Therefore, the single-soliton-based RF filter response  $H_{SSM}(f_{RF})$  is derived by substituting  $G(f_{RF})$  back to Eq. (5.1) as:

$$H_{SSM}(f_{RF}) \sim \cos(2\pi^2 \Theta_2 f_{RF}^2) \sum_{n=-\infty}^{\infty} G(f_{RF} - n f_{FSR}) \quad (5.6)$$

It is seen that the RF filter shows periodic filter responses and modulated by a fading envelope, with FSR of  $f_{FSR}$ . As the tap weights are all-positive, the passband frequencies of the RF filters are at every multiples of  $f_{FSR}$ , including a DC response. We focus on the first passband in this chapter. This single-soliton condition is shown schematically in Figure 5.1 a.

Figure 5.1 b illustrates the condition when the  $N$ -PSC state ( $N = 4$  is shown) is generated and being used for the RF filtering. The defect-free  $N$ -PSC corresponds to  $N$  ( $N \in \mathbb{N}_{\geq 2}$ ) in-phase solitons equally distributed in one period. Spectrally,  $N$ -PSC multiplies the initial comb line spacing by  $N$ -times, as if the single soliton is generated from a  $N$ -times smaller microresonator. Their corresponding RF filter responses  $H_{N-PSC}(f_{RF})$  can thus be simply inferred from the

single-soliton case:

$$H_{N-PSC}(f_{RF}) \sim \cos(2\pi^2 \Theta_2 f_{RF}^2) \sum_{n=-\infty}^{\infty} G(f_{RF} - n \frac{f_{FSR}}{N}) \quad (5.7)$$

Here the filter FSR  $f_{FSR} = 1/2\pi\Theta_2\Delta f$  is effectively reduced by  $N$ -times due to the  $N$ -times enlargement of the comb FSR. As a result, this would impart  $N$ -times division of the filter passband frequencies.

When there are two solitons circulating in the microresonator, the corresponding RF filter response can be formulated in a similar manner. Assume that the two solitons are of identical amplitudes and pulse widths, which is generally the case for multi-soliton microcombs. The optical field is thus given by:

$$E(t) \sim \left\{ \text{sech}\left(\frac{t}{T_s}\right) + \text{sech}\left(\frac{t - \frac{\alpha T}{2\pi}}{T_s}\right) \right\} \otimes \sum_{n=-\infty}^{\infty} \delta(t - nT) \quad (5.8)$$

where  $\alpha$  is the relative azimuthal angle between two solitons, expressed in radian. The TSM spectrum can be found by Fourier transform of Eq. (5.8):

$$\tilde{E}(f) \sim \text{sech}(\pi^2 T_0 f) (1 + \exp(-i\alpha k)) \sum_{k=-\infty}^{\infty} \delta(f - k\Delta f) \quad (5.9)$$

We then obtain the filter tap weights as:

$$|a_k|^2 \sim \text{sech}^2(\pi^2 k T_0 / T) (2 + 2\cos(\alpha k)) \quad (5.10)$$

where  $k \in \mathbb{Z}$  is the comb mode index relative to the center mode. Inserting Eq. (5.10) back to Eq. (5.1) derives:

$$H_{TSM}(f_{RF}) \sim \cos(2\pi^2 \Theta_2 f_{RF}^2) \sum_{n=-\infty}^{\infty} \left\{ 2G(f_{RF}) + G(f_{RF} - \frac{\alpha}{2\pi} f_{FSR}) + G(f_{RF} + \frac{\alpha}{2\pi} f_{FSR}) \right\} \quad (5.11)$$

Compared to Eq. 5.6, clearly new passbands of halved amplitudes appear due to two-soliton interference, which are displaced at both sides from the initial response according to the relative angle between them. Thus, the RF filter passbands can slide inside the  $f_{FSR}$  by modifying the relative soliton angles. This condition is depicted in Figure 5.1 c.

Besides, we can also derive the RF filter bandwidth from Eq. (5.5), which is approximately  $2.98 T_s f_{FSR} / T$ . It is proportional to the soliton pulse width and the RF filter FSR, as well as the repetition-rate of the underlying microcomb.

**Microresonator FSR selection.** We also investigate the impact of microresonator FSR on the synthesized RF filter. The simulation is based on the fundamental single-soliton condition formulated in Eq. (5.6), therefore the microcomb FSR corresponds to the microresonator FSR, while the RF filters using PSC and TSM states are simply the division and translation of the

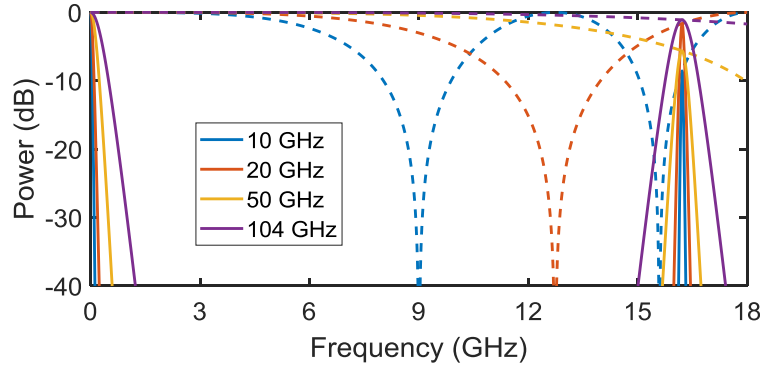


Figure 5.2 – Visualization of RF filter response using different microcomb FSR. Simulated RF filter responses (solid lines) based on various microcomb FSRs  $\Delta f$  from 10 GHz, 20 GHz, 50 GHz to 104 GHz (FSR used in this study) are shown. The dispersion-induced fading envelopes (dashed lines) are also sketched. Soliton pulse width  $T_s = 100$  fs is considered for all the cases in the simulation, while the accumulated dispersion  $\Theta_2$  is adapted so that all these RF filters coincide at the same frequency.

single soliton case. Subjected to the measurement range of VNA, we have chosen the RF FSR  $f_{FSR}$  to be around 16 GHz. Here the amount of accumulated dispersion  $\Theta_2$  also needs to be adjusted for different microcomb FSR.

In Figure 5.2, we visualize specifically the RF photonic filters using 10 GHz, 20 GHz, 50 GHz, and 104 GHz single-soliton states, with identical soliton pulse width  $T_s = 100$  fs assumed. It is clearly observed that the envelope fading becomes more severe for small FSR microcomb due to the large  $\Theta_2$  being used as to maintain the same center frequency of the filter. That is the reason why advanced modulation technique is needed in Section 3.4 to eliminate the fading effect. In comparison, microcombs of large comb spacing allow for a simple RF uploading method. Also, since we are interested in RF filters up to around 16 GHz, the underlying comb with repetition-rate over 32 GHz is preferred to avoid spurs generated from the signal beating with other comb lines [37]. Such spur-free frequency range is the so-called Nyquist zone given by half of the comb FSR. On the other hand, if one requires RF filters with narrower bandwidth, a microresonator with larger size generating smaller FSR comb will be a better choice. This is because the filter bandwidth scales with the comb FSR given a certain soliton pulse width, as discussed above. The recent ultralow loss  $\text{Si}_3\text{N}_4$  technology has successfully demonstrate soliton formation down to the 10 GHz range [186], which would enable RF filters of only tens of MHz bandwidth without additional pulse shaping. Since obtaining narrow RF photonic filter is not the primary interest in this study, we utilize a 103.9 GHz microresonator in the experiment. This allows simple RF upconversion and spur-free operation. While the working principle presented here remains compatible with other microcomb FSR.

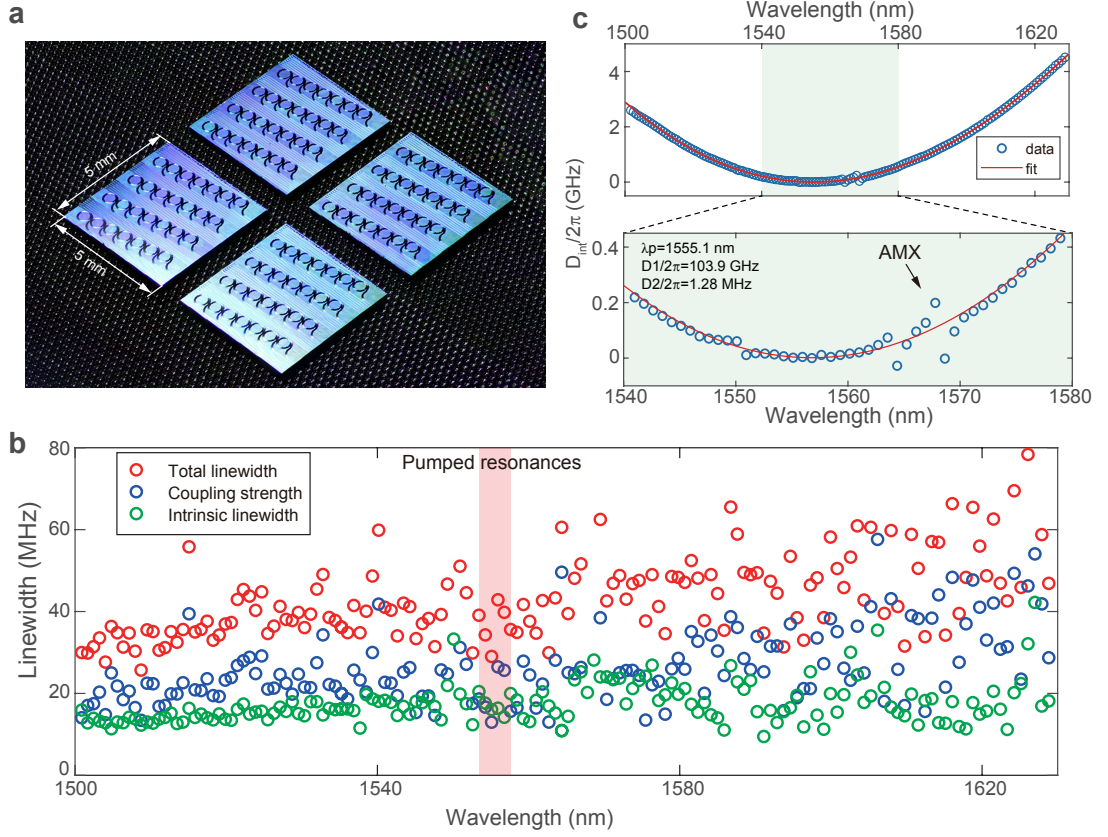


Figure 5.3 –  $\text{Si}_3\text{N}_4$  microresonator characterization. (a) Optical image of the  $\text{Si}_3\text{N}_4$  microresonator chips. (b) Total linewidth, coupling strength, and intrinsic linewidth of each resonance in the  $\text{TE}_{00}$  mode family. The shaded area corresponds to the resonances pumped in the experiment. (c) Top: measured integrated group velocity dispersion (GVD) ( $D_{int}/2\pi$ ) of the  $\text{TE}_{00}$  mode family with respect to the resonance of 1555.1 nm; Bottom: zoom-in of integrated GVD region between 1540 nm and 1580 nm. Dominant avoided mode crossing (AMX) is observed around wavelength region of 1565 nm.

### 5.3 Versatile soliton microcomb generation

The soliton microcombs used for RF filtering are generated from an 103.9 GHz ultra-low loss integrated  $\text{Si}_3\text{N}_4$  microresonator ( $Q \sim 1 \times 10^7$ ), fabricated by the photonic Damascene reflow process [17]. The microresonator is a ring structure with radius of  $217 \mu\text{m}$  (Figure 5.3 a). The waveguide cross sections (width  $\times$  height) of both the bus and ring waveguides are made to be  $1500 \text{ nm} \times 750 \text{ nm}$ . To achieve critical coupling for the resonances in the telecom-band around 1550 nm, the gap distance between the ring and bus waveguide is designed to be 690 nm.

**Microresonator characterization.** By employing frequency-comb-assisted diode laser spectroscopy [187], the detailed information of resonances and the integrated group velocity dispersion (GVD) of the microresonator are measured, covering the wavelength region from 1500 nm to 1630 nm. Figure 5.3 b illustrates the properties of the resonances, i.e. intrinsic linewidths



$\kappa_0/2\pi$ , coupling strengths  $\kappa_{ex}/2\pi$ , as well as the total linewidths  $\kappa/2\pi = (\kappa_0 + \kappa_{ex})/2\pi$  of the  $TE_{00}$  mode family, which are extracted from the fittings of calibrated transmission spectrum. The shaded area of Figure 5.3 b denotes the experimentally accessed resonances around 1556 nm for the RF filter demonstrations. All these resonances show intrinsic linewidths  $\kappa_0/2\pi \approx 20$  MHz, indicating the intrinsic Q factors to be around  $1 \times 10^7$ . Besides, the coupling strengths of the pumped resonances are similar to their intrinsic linewidths, implying these resonances are near critical coupling condition.

Then, the integrated GVD of the  $TE_{00}$  mode family can also be extracted by identifying the precise frequency of each resonance, as shown in Figure 5.3 c. The formula of integrated GVD is introduced in Section 2.4:

$$D_{int}(\mu) = \omega_\mu - (\omega_0 + D_1\mu) = D_2\mu^2/2 + D_3\mu^3/6 + \dots \quad (5.12)$$

where  $D_1/2\pi$  is the FSR of microresonator, and  $D_n (n \in \mathbb{N}_{\geq 2})$  correspond to the  $n$ -th order dispersion coefficients.  $D_{int}(\mu)$  is defined as the deviation of the  $\mu$ -th resonance frequency  $\omega_\mu/2\pi$  from the equidistant frequency grid, constructed from the FSR around the reference resonance frequency  $\omega_0/2\pi$ . Here, the reference resonance is chosen at  $\omega_0/2\pi = 192.8$  THz (i.e.  $\lambda_0 = 1555.1$  nm). The retrieved dispersion terms are  $D_1/2\pi \approx 103.9$  GHz,  $D_2/2\pi \approx 1.28$  MHz, and  $D_3/2\pi \sim \mathcal{O}(1)$  kHz. As described in Section 2.4, operating at anomalous dispersion ( $D_2 > 0$ ) is a prerequisite for soliton formation. The bottom part of Figure 5.3 c shows the zoom-in view of the integrated GVD. Several avoided mode crossings (AMX) are clearly observed in the measured GVD profile, and the most pronounced region is found around the wavelength of 1565 nm. As will be seen below, AMX is responsible for the modulation of intracavity CW background, thereby resulting in the ordering of the multi-solitons [188] and the evolution of soliton crystals [62, 189].

**Soliton microcomb generation.** Figure 5.4 a shows the simulated stability diagram, which consists of modulation instability (MI), breathers, chaos (spatio-temporal chaos and transient chaos), and stable dissipative Kerr soliton states. The stability diagram is obtained from the simulation of Lugiato–Lefever equation (LLE) incorporating the experimental AMX condition (perturbation is added to a specific frequency mode in Eq. (2.22)). Recently, it has been revealed that the pump power level is critical for whether the PSC or stochastic soliton states are formed [62]. In our case, the threshold pump power  $P_{th}$  is found to be around 20 mW in the bus waveguide. When the laser scanning route is operated below this threshold pump power, defect-free PSC states can be accessed without crossing the chaos region. Contrarily, soliton states with stochastic soliton number and relative distribution are accessed above the threshold power. Experimentally, the single soliton and TSM states are reached by either directly falling on such states or via backward tuning from the states with higher soliton number [190]. For example, Figure 5.4 b shows three optical microcombs obtained from the same resonance of 1555.1 nm: single-soliton, PSC ( $N = 4$ ), and TSM ( $\alpha = 132.7^\circ$ ), respectively.

Figure 5.4 c depicts distinct soliton step features by pumping the resonance of 1555.1 nm under

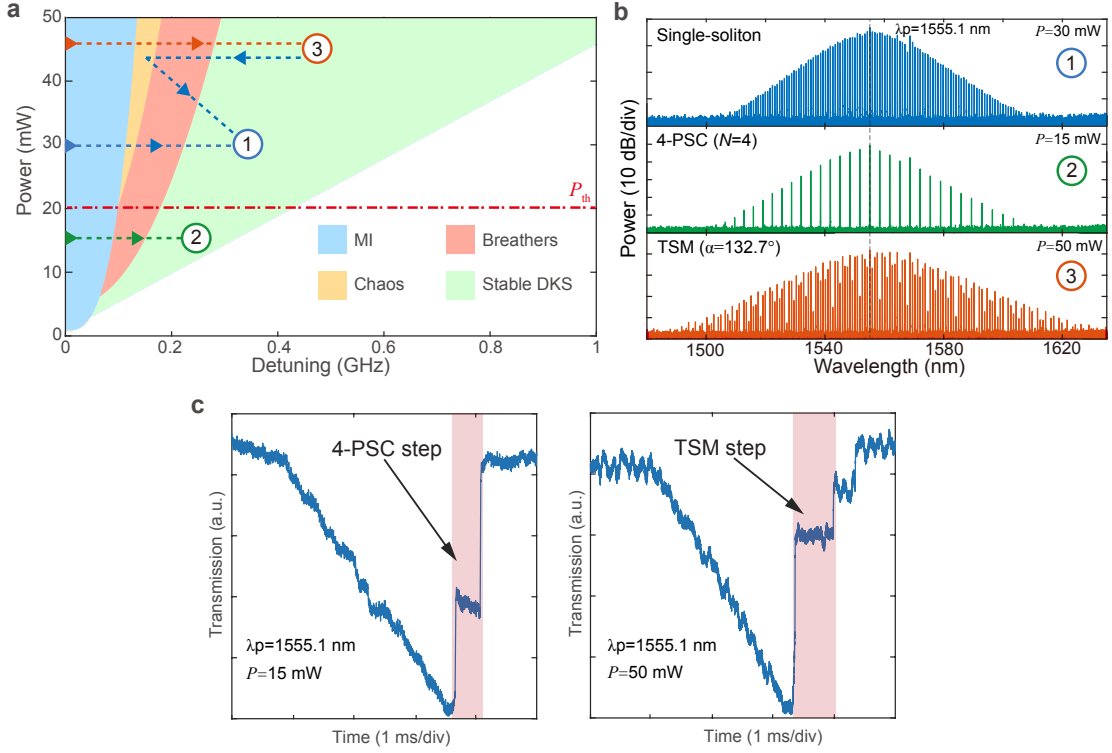


Figure 5.4 – Excitation of versatile soliton states. (a) Simulated stability diagram for versatile soliton microcomb generation. Four different stability regions are listed: modulation instability (MI, blue), breathers (red), spatio-temporal and transient chaos (chaos, yellow), and stable dissipative Kerr soliton (DKS, green). Excitation routes for (1) single-soliton, (2) PSC, and (3) TSM generation are depicted. (b) Examples of experimentally generated spectra at resonance of 1555.1 nm: (1) single-soliton, (2) PSC ( $N = 4$ ), and (3) TSM ( $\alpha = 132.7^\circ$ ). The pump power is also indicated for each microcomb generation. (c) Typical soliton steps for PSC and TSM formations, which are respectively denoted by the shaded areas. Transmission curves are obtained by scanning a laser across the resonance below (left) and above (right) the threshold pump power, at resonance of 1555.1 nm.

and above the threshold power  $P_{th}$ . The soliton step is manifested from the transmission of the microresonator by scanning the CW pump laser frequency over the resonance. When the pump power is around 15 mW, only a single PSC step is formed, and a soliton number of 4 is indicated by the depth of the step. However, if the power of pump laser is increased to around 50 mW, both two-soliton and single-soliton steps would appear. The distinct soliton steps clearly indicate two different soliton generation regimes, and are consistent with experimentally generated microcomb spectra. Thus, through controlling the pump power and resonance frequency, various soliton microcombs (single-soliton, PSC, and TSM) can be obtained on demand to produce the desired RF filter responses. It is also worthwhile to mention that although this type of RF filter does not require coherent comb states, the high intensity noise of MI combs is certainly undesirable [81]. Since the intensity noise will be

transferred to the synthesized RF filters, mode-locked comb states are preferred to minimize the noise at the RF output.

#### 5.4 Reconfigurable soliton-based RF filter

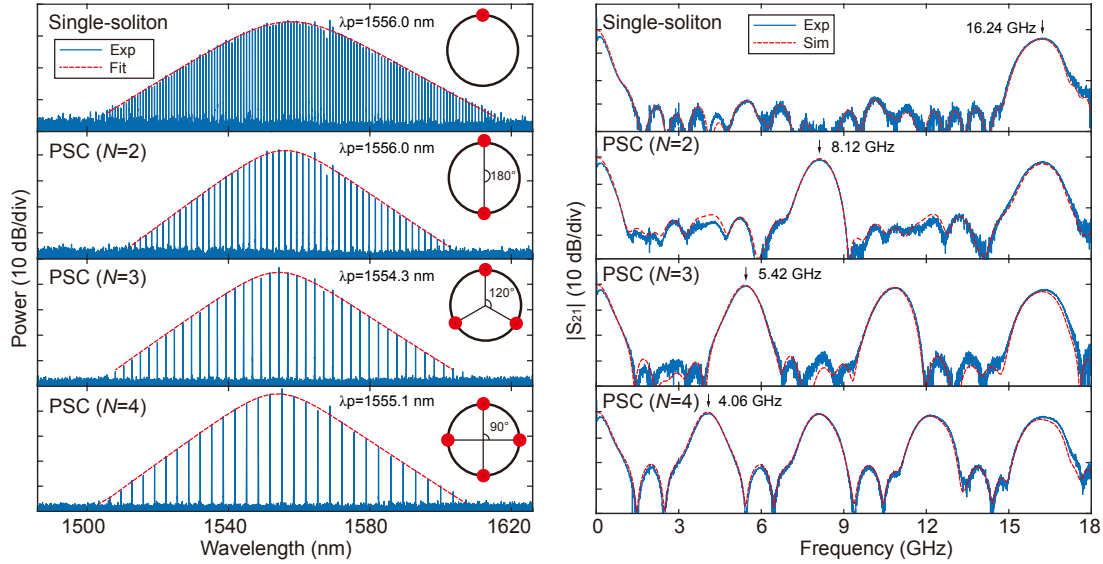


Figure 5.5 – Single-soliton/PSC spectra and their corresponding RF photonic filters. Through deterministic accessing PSC states of different resonances, the RF filter passbands can be divided correspondingly. Left column: microcomb spectra (blue: experiment, red:  $\text{sech}^2$  fitting). The insets of left column illustrate soliton distribution inside the microresonator: single-soliton and PSCs with adjacent soliton angles of  $180^\circ$ ,  $120^\circ$ , and  $90^\circ$ , respectively ( $360^\circ/N$ ,  $N = 2, 3, 4$ ). Right column: corresponding normalized RF filter responses (blue: experiment, red: simulation). From top to bottom: RF filters centered at 16.24 GHz, 8.12 GHz, 5.42 GHz, and 4.06 GHz based on single-soliton and  $N$ -PSC ( $N = 2, 3, 4$ ), generated at resonances of 1556.0 nm, 1556.0 nm, 1554.3 nm, 1555.1 nm, respectively.

The versatile soliton microcombs are then harnessed for RF photonic filters. First, we detail the experimental implementation. A C-band tunable CW laser is amplified by an EDFA with ASE filtered, polarization aligned at the TE mode, and then coupled to a 104 GHz  $\text{Si}_3\text{N}_4$  microresonator for soliton microcomb generation. Lensed fibers are used for the input and output coupling of the chip, with around 30% fiber-chip-fiber coupling efficiency. Soliton microcombs are initiated by scanning the pump over the resonances via the assistance of an arbitrary function generator [124]. The residual pump of the generated microcomb is then filtered by a tunable fiber Bragg grating (FBG), while a circulator is inserted in between to avoid back-reflection. 10% of light is tapped to an optical spectrum analyzer (OSA) to record the microcomb spectra. While the other 90% of the light is amplified, and polarization managed, before sending to a 30 GHz bandwidth MZM. RF signals from the VNA are applied to the MZM in DSB modulation format. The modulated spectra are then propagated through a spool

of 4583.8 m SMF to acquire dispersive delays, and finally beats at a 18 GHz PD to convert the signals back to the RF domain. The length of SMF is measured by a commercial optical time-domain reflectometer (OTDR).

**Single-soliton/PSC-based RF filters.** Figure 5.5 depicts the RF photonic filters using single-soliton and PSC states with various soliton number. The RF filter based on single-soliton is centered at 16.24 GHz with MSSR of 23.2 dB. Further, various PSC states are deterministically obtained at different resonances under the threshold power, thereby all-optically reconfiguring the corresponding RF filters. The comb spacing multiplication via PSC results in the division of the corresponding RF passbands. RF filters centered at 8.12 GHz, 5.42 GHz, and 4.06 GHz (Figure 5.5 b-d) are experimentally synthesized through 2, 3, and 4 equally spaced solitons, with MSSR of 22.6 dB, 25.6 dB, and 20.4 dB, respectively. All these RF filters achieve MSSR over 20 dB without additional programmable spectral shaping. The MSSR here are limited by the smoothness of the optical spectra [37], as several AMX can be seen in the microcombs. Nevertheless, all these microcombs preserve well the  $\text{sech}^2$  envelope, and remained smooth after amplification.

In addition, the measured RF filter responses are compared to simulation results. For more accurate fitting in the simulation, we also take into account the third-order dispersion  $\beta_3$  of SME. The RF filter response in the presence of  $\beta_3$  can be formulated as [155]:

$$H(f_{RF}) \sim \sum_k |a_k|^2 \cos(2\pi^2 \Theta_2 f_{RF}^2 + 4\pi^3 \Theta_3 k \Delta f^2 f_{RF}) \times \dots \exp(i4\pi^2 \Delta f (\Theta_2 k f_{RF} + \pi \Theta_3 k^2 \Delta f f_{RF} + \frac{\pi}{3} \Theta_3 \Delta f^2)) \quad (5.13)$$

where  $\Theta_3 = -\beta_3 L$ , and it is noted that Eq (5.13) converges to Eq. (5.1) when  $\Theta_3$  is negligible.  $|a_k|^2$  correspond to the comb line intensity. They are extracted from the measured optical spectra but after the EDFA, as the amplifying bandwidth of EDFA cuts part of the generated microcomb spectra. In accordance with typical values of SMF dispersion,  $\beta_2 = -20.2 \text{ ps}^2/\text{km}$  and  $\beta_3 = 0.117 \text{ ps}^3/\text{km}$  at 1550 nm are estimated in the fittings of RF filters. It can be seen in Figure 5.5 that the simulation results are in excellent agreement with experimental RF filter responses. Note that the bandwidths of experimentally synthesized RF filters broaden slightly with their center frequencies, also due to the third-order dispersion of SMF [81].

The number of various PSC states that are accessible for a microresonator is subject to a certain limit. In fact, the maximum soliton number that can be sustained in a microresonator is roughly estimated by  $\sqrt{\kappa/D_2}$  [62]. PSC with a higher number of pulses would lead to the interaction between them and destabilize the state. By substituting the total linewidths of the pumped resonances, the maximum PSC number in our chip is estimated around 5. This provides a good approximation as we can achieve PSC numbers from 2 to 4 experimentally. We also need to point out here that not every PSC state below this predicted value is easily generated, especially for a large maximum PSC number [62]. This eventually defines the possible number of RF filters that can be achieved by passband frequency division.

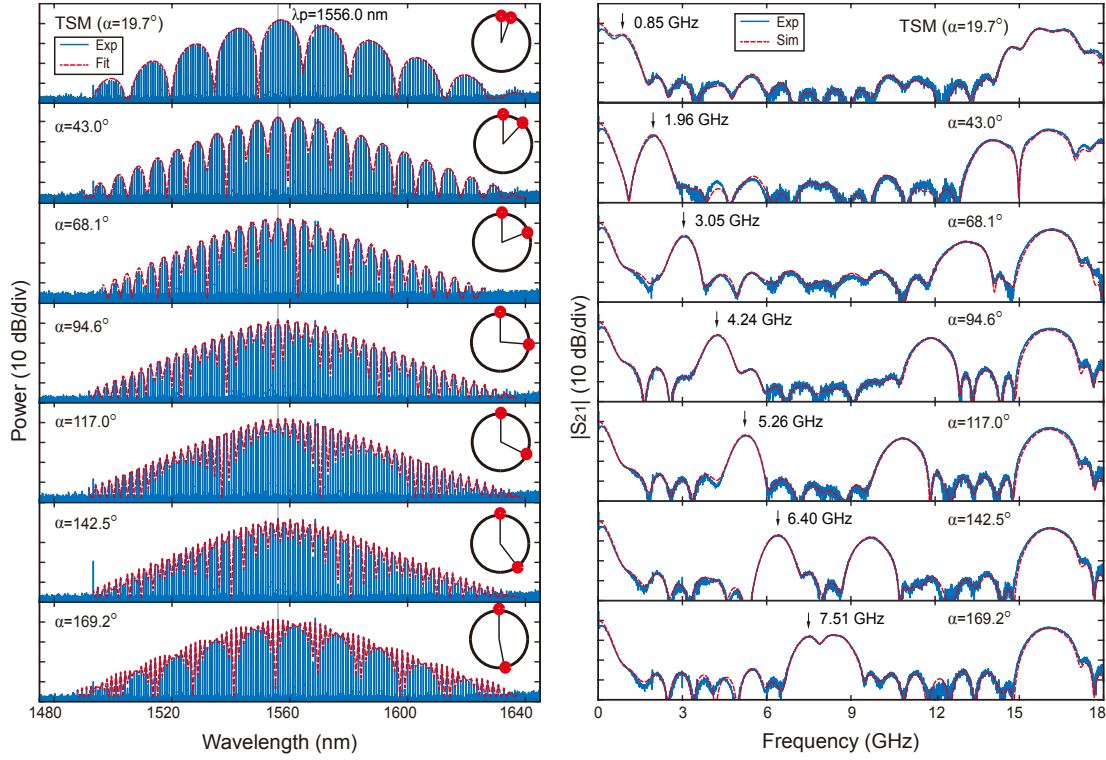


Figure 5.6 – TSM spectra and their corresponding RF photonic filters. By accessing different two-soliton states, the RF filters can be all-optically reconfigured. Left column: TSM spectra obtained from the resonance of 1556.0 nm (blue: experiment, red: envelope fitting). The insets illustrate two soliton distribution inside the microresonator: the angles between them are  $19.7^\circ$ ,  $43.0^\circ$ ,  $68.1^\circ$ ,  $94.6^\circ$ ,  $117.0^\circ$ ,  $142.5^\circ$ , and  $169.2^\circ$ , respectively. Right column: corresponding normalized RF filter responses (blue: experiment, red: simulation). From top to bottom: RF filters centered at 0.85 GHz, 1.96 GHz, 3.05 GHz, 4.24 GHz, 5.26 GHz, 6.40 GHz, and 7.51 GHz.

**TSM-based RF filters.** Figure 5.6 shows the TSM spectra and their corresponding RF filter responses, pumped at resonance of 1556.0 nm. According to Eq. (5.11), the first passband frequency of RF filter scales linearly with the relative angle between two solitons, so that the filter reconfiguration is achieved. In the experiment, TSM spectra with relative angles of  $19.7^\circ$ ,  $43.0^\circ$ ,  $68.1^\circ$ ,  $94.6^\circ$ ,  $117.0^\circ$ ,  $142.5^\circ$ , and  $169.2^\circ$  are generated, where the angles are retrieved from the fitting of the microcomb spectral envelopes. It is obtained first by extracting the power of each comb mode of experimental TSM spectra. And pump mode is rejected and amplitude rescaling is considered as a fitting parameter. Note that the amount of spectral red-shift due to Raman effect is also estimated in fitting, by displacing the center of  $\text{sech}^2$  soliton spectra from the pump comb mode. Then, the rescaling parameter and red-shift are estimated to best fit the experimental data with the TSM spectral envelope given by Eq. (5.10), thereby retrieving the azimuthal angle between two solitons. It is seen that excellent match between the experimental and fitting spectra are obtained.

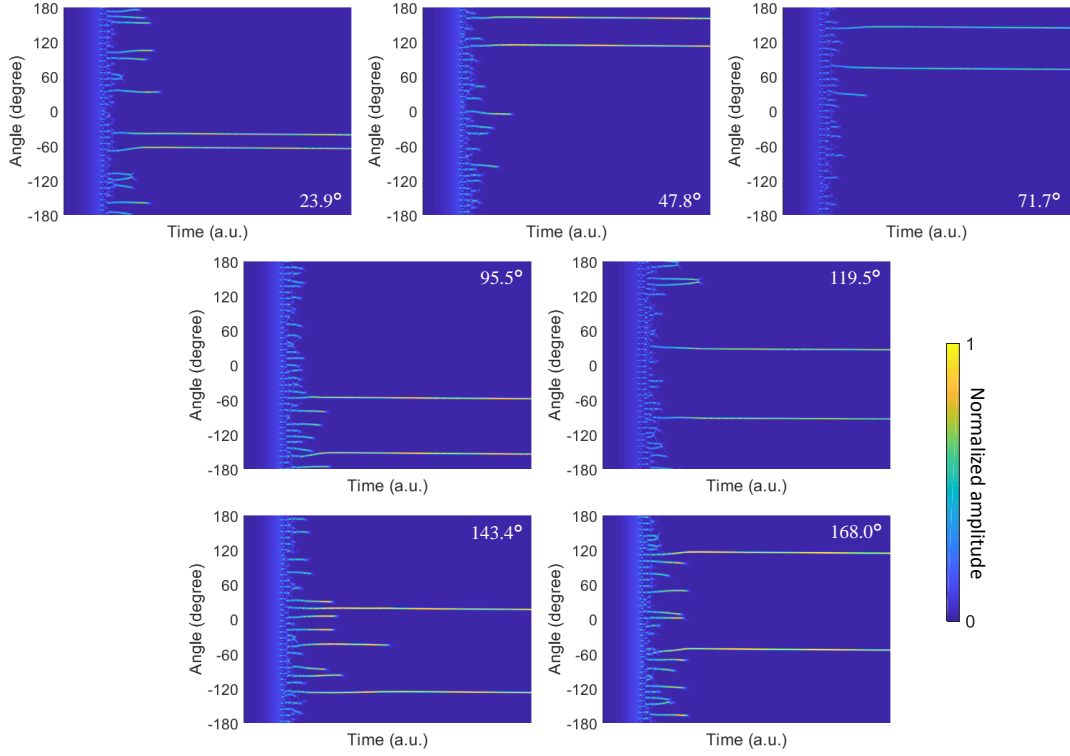


Figure 5.7 – Simulation of TSM states. The intracavity waveform evolutions of all the possible excitations of two-soliton states are shown. In total seven distinct steady states are observed, where the angle in each plot indicates the relative angle between the two solitons. The simulation is implemented based on the perturbed Lugiato–Lefever equation (LLE).

Importantly, the possible angles between two solitons are determined by the overall AMX profile, and are rather robust to both laser power and frequency detuning, thereby deterministically dictating the filter passband frequencies to be either one of those shown in Figure 5.6. To gain insights of the relative angles between two solitons, we also perform LLE simulation (Eq. (2.22)) to investigate the TSM formations. Here the LLE is perturbed by the AMX as observed in integrated GVD profile. To involve the AMX effect, an additional frequency detuning  $\Delta_k$  is introduced at the  $k$ -th mode, so that the frequency of the  $k$ -th mode becomes  $\omega_k = \omega_0 + D_1 k + D_2 k^2/2 + \Delta_k$ . Here in simulation, the dispersion is limited to  $D_2$ , and the Raman and thermal effects are not taken into account. According to the dispersion measurement and the generated microcomb spectra, the parameters for the AMX in the simulation are set as  $k = 15$  and  $\Delta_k/2\pi = 100$  MHz, enabling the modulation of the CW intracavity background for the trapping of soliton temporal positions. Note that the strength of the AMX here is estimated to introduce the regularizability of solitons, but without disturbing their formations [62]. Other parameters used in the simulation are retrieved from the characterization, that is,  $D_1/2\pi = 103.9$  GHz,  $D_2/2\pi = 1.28$  MHz,  $\kappa_{ex}/2\pi = \kappa_0/2\pi = \kappa/4\pi = 20$  MHz.

Figure 5.7 demonstrates all the possible intracavity waveform evolutions that lead to the

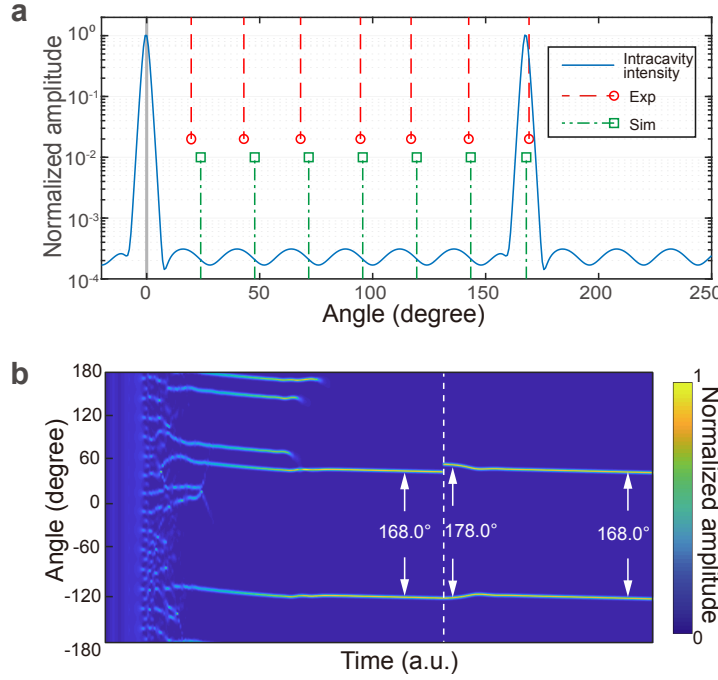


Figure 5.8 – Analysis of relative angles between two solitons. (a) One example of the simulated TSM intracavity intensity profile (blue), where AMX-induced background modulation is observed. The red and green lines respectively indicate the measured and simulated possible azimuthal angles between two solitons. (b) Simulation of the intracavity waveform evolution of TSM for robustness test. First, TSM state with relative angle of  $168.0^\circ$  is excited by scanning the pump over the resonance. Once the TSM becomes stable, a  $10.0^\circ$  perturbation is introduced to one of the solitons at white dashed line. The relative angle will re-stabilize to the original angle of  $168.0^\circ$  after a period of free running.

formation of two-soliton states. The simulation is executed by decreasing the pump frequency in the perturbed LLE described above. Versatile soliton generation occurs when the pump frequency approaches and scans over the resonance, where only the two-soliton states are recorded. In total seven distinct steady state two-soliton distributions are observed in simulation, which is in accordance with experimental results. The blue curve in Figure 5.8 a shows one of the two-soliton temporal intracavity profile. Due to the AMX effect, periodic intensity modulation is observed upon the CW background. It is clearly seen that the soliton can only be excited at specific parameter gradients [188], as manifested by the green dashed lines which correspond to the stationary solutions obtained in simulation. These possible soliton angles are in good agreement with experimental results, indicated as red dashed lines. To further test the robustness of the angle between two solitons, an external perturbation is deliberately introduced on their relative angle. Figure 5.8 b illustrates the dynamical evolution of the two-soliton state under the disturbance. As before, the simulation is initiated as a standard laser scanning scheme to kick out two solitons. Once the simulation reaches stable two-soliton solution (relative angle of  $168.0^\circ$ ), one of the solitons is dragged from its original position by

a  $10.0^\circ$  on purpose. After a period of free running, the two solitons converge back to their original relative positions, again at  $168.0^\circ$  apart. This confirms the regulation of two solitons under AMX background modulation.

Figure 5.6 also illustrates the measured RF filters of resonance  $1556.0\text{ nm}$  centered at  $0.85\text{ GHz}$ ,  $1.96\text{ GHz}$ ,  $3.05\text{ GHz}$ ,  $4.24\text{ GHz}$ ,  $5.26\text{ GHz}$ ,  $6.40\text{ GHz}$ , and  $7.51\text{ GHz}$ . Owing to the binding effect of two-soliton states, these RF filters are decisive for a certain optical resonance. As in the case of PSC, a slight broadening of the filter passband width from  $490\text{ MHz}$  to  $620\text{ MHz}$  is attributed to the third-order dispersion of SMF. Overall, the RF filters obtained at resonance  $1556.0\text{ nm}$  could vary from DC to  $8.1\text{ GHz}$  ( $f_{FSR}/2$ ) with maximum grid of  $1.2\text{ GHz}$ , while roughly preserving the filter bandwidth in the meantime. In addition, mirrored passband responses of the TSM-based RF filters coexist between  $8.1\text{ GHz}$  and  $16.2\text{ GHz}$ . The simulation of TSM-based RF filter responses is similar to the case of PSC. It is also based on Eq. (5.13) with the same SMF dispersion parameters, and the comb line power is extracted from the experimental TSM spectra.

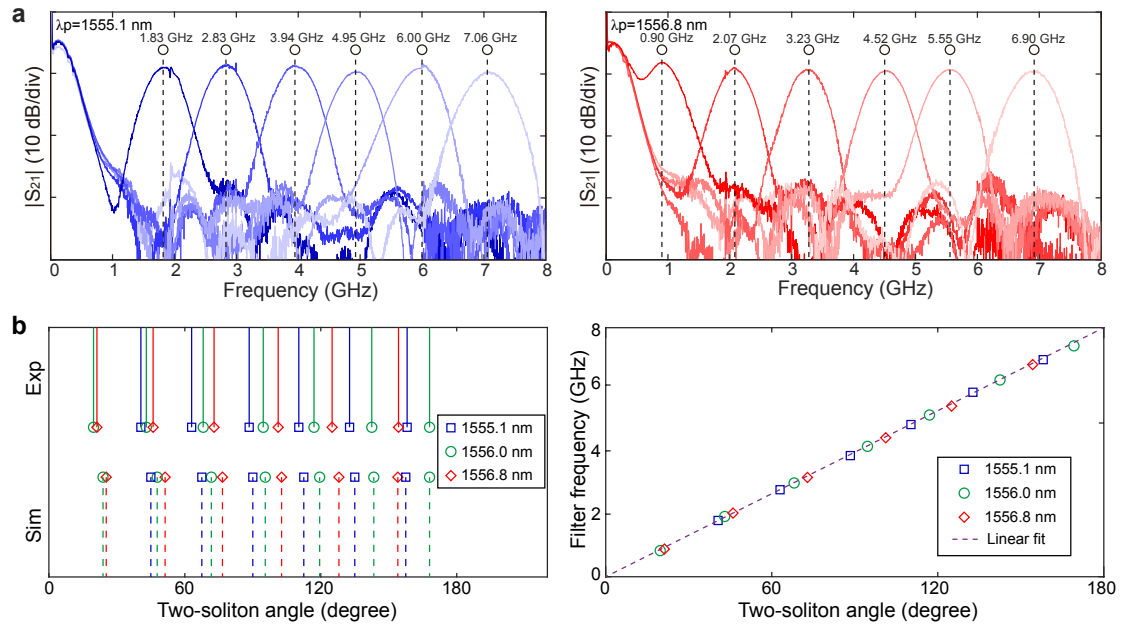


Figure 5.9 – TSM-based RF filters from multiple resonances. (a) Left: RF filters centered at  $1.83\text{ GHz}$ ,  $2.83\text{ GHz}$ ,  $3.94\text{ GHz}$ ,  $4.95\text{ GHz}$ ,  $6.00\text{ GHz}$ , and  $7.06\text{ GHz}$  are obtained at resonance of  $1555.1\text{ nm}$ . Right: RF filters centered at  $0.90\text{ GHz}$ ,  $2.07\text{ GHz}$ ,  $3.23\text{ GHz}$ ,  $4.52\text{ GHz}$ ,  $5.55\text{ GHz}$ , and  $6.90\text{ GHz}$  are obtained at resonance of  $1556.8\text{ nm}$ . (b) Left: experimentally retrieved (solid lines, top) and simulated (dashed lines, bottom) two-soliton angles at resonances of  $1555.1\text{ nm}$ ,  $1556.0\text{ nm}$ , and  $1556.8\text{ nm}$ . Right: the synthesized RF filter frequencies versus their underlying two-soliton angles retrieved from TSM spectra. The dashed line denotes the linear dependence between them.

More TSM-based RF filters can be achieved by exploiting adjacent resonances of  $1556.0\text{ nm}$ . Figure 5.9 a shows the RF filters obtained from resonances of  $1555.1\text{ nm}$  and  $1556.8\text{ nm}$ ,



together with the indicated filter passband frequencies. It is seen that the center frequencies of these filters are relocated for different resonances. Considering all the RF filters synthesized from these three resonances, the granularity of filter is further reduced to be less than 1 GHz. Such passband frequency shifts of RF filters arise from the variation of their underlying two-soliton azimuthal angles, which can be experimentally retrieved from their spectra and compared to numerical simulation shown in Figure 5.9 b (left). In the simulation, the AMX position is varied from 14-th to 16-th away from the pump of the same strength, to resemble the change of resonances in line with experimental condition. The background modulation period is then modified according to the relative distance between the pump mode and the AMX. Besides, towards large relative soliton angle, the modification of its value through pumped resonance also becomes more prominent. This effect is simply due to the accumulated periodicity difference, and is clearly observed in both measured and simulated results. Figure 5.9 b (right) illustrates the relation between the experimental RF passband frequencies and their corresponding TSM azimuthal angles. A good linear approximation confirms well the operation principle of TSM-based RF filters as formulated in 5.11.

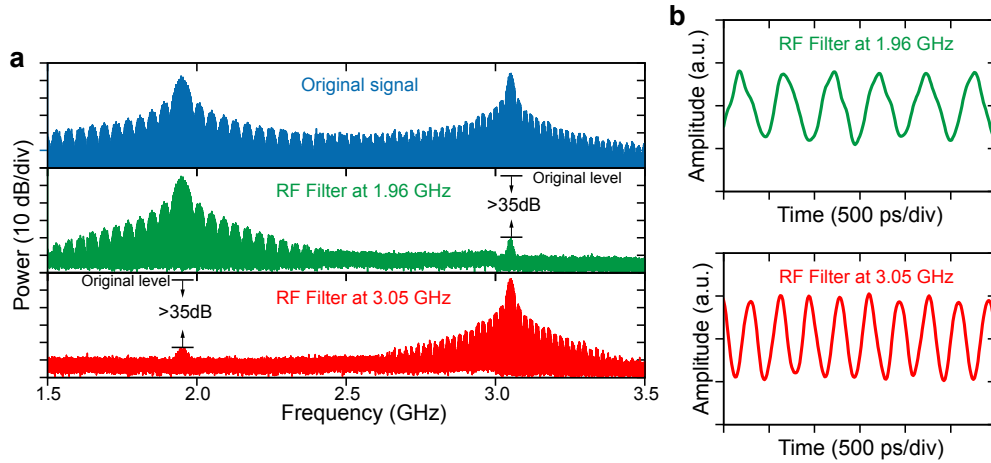


Figure 5.10 – Proof-of-concept filter reconfiguration experiment using TSM-based RF filters. Two phase-shift keying (PSK) signals with 40 Mb/s modulation at 1.96 GHz and 20 Mb/s modulation at 3.05 GHz, are filtered by the TSM-based RF filters configured at 1.96 GHz and 3.05 GHz, respectively. (a) From top to bottom: electrical spectra of original RF signal, signal after 1.96 GHz filter, and signal after 3.05 GHz filter. (b) Top: Waveform after 1.96 GHz filter; Bottom: waveform after 3.05 GHz filter.

**RF filter reconfiguration experiment.** A proof-of-concept RF filter reconfiguration experiment is also illustrated in Figure 5.10 based on TSM-enabled RF filters. Two phase-shift keying (PSK) signals in which a 40 Mb/s modulation at 1.96 GHz tone and a 20 Mb/s modulation at 3.05 GHz tone, are generated separately from the two channels of an arbitrary waveform generator (AWG). After superimposing the two streams of signals in a combiner, the composite signal is sent through the TSM-based RF filters. The RF filters are then respectively reconfigured at 1.96 GHz and 3.05 GHz to filter the input signals, by triggering the TSM spectra of corresponding soliton angles. At the output of the RF filters, nearly complete rejection of

either one of the PSK signals is observed on the electrical spectrum analyzer (ESA) (Figure 5.10 a), where the extinction ratios exceed 35 dB for both cases. Figure 5.10 b show the filtered output RF waveforms recorded by a high-speed real-time oscilloscope. The periodicity of the output temporal traces corroborate the filtering of the original RF signals.

## 5.5 Performance of soliton-based RF filter

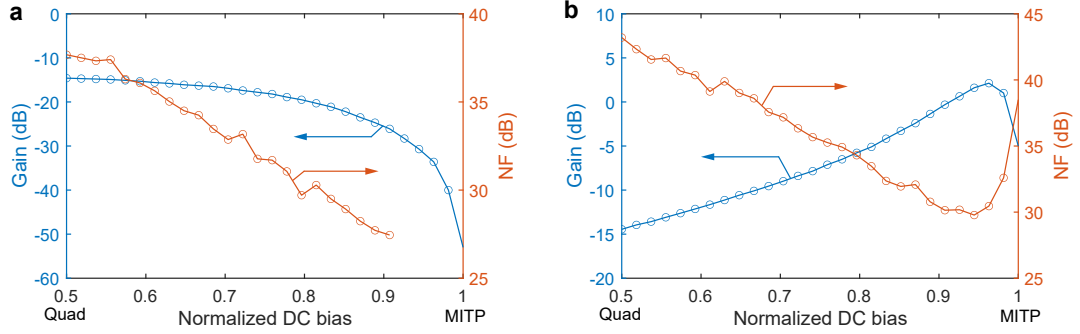


Figure 5.11 – Link performance optimization of the RF filter. Gain and noise figure (NF) of the RF filter based on 4-PSC versus the bias of MZM (a) without EDFA at the MZM output (b) with EDFA at the MZM output. Quad: quadrature; MITP: minimum transmission point.

**RF filter link optimization.** We also characterize and optimize the gain and noise figure of our microcomb-based RF filters. We measure in particular the RF filter centered around 4 GHz based on 4-PSC, while the performances as well as optimization technique are roughly similar for other cases. An RF amplifier is used to lift the noise floor of the ESA (set at 1 Hz resolution bandwidth) when measuring the filter noise figure. And the noise figure is assessed at the center frequency of the filter which is of the primary interest. Since the link gain depends quadratically on the optical power [174], we use a PD with high power handling capability (maximum input power  $\sim +16$  dBm, responsivity  $\sim 0.6$  A/W) in the link experiment.

It is well known that the DC bias point of the MZM plays an important role in determining the filter's gain and noise figure. The filter gain is maximized when the MZM is biased at quadrature. However, when the bias is gradually decreased to the MITP, although the gain drops, the noise actually reduces faster than the gain, which is known as the low-biasing technique [174]. Thus, we vary the MZM DC bias while keeping the same optical power at the MZM input around 150 mW (limited by its maximum input power), and we measure the gain and noise figure of the filter as shown in Figure 5.11 a. The DC bias is normalized here, where 0, 0.5, 1 correspond to bias points at MATP, quadrature, and MITP, respectively. Indeed, when we tune the bias from quadrature towards MITP, both the filter gain and noise figure are decreased. Note that we were not able to measure the noise figure values at very low bias point close to MITP, as the noise floor there becomes comparable with the displayed noise level [191]. In this configuration, we could obtain RF filter with loss of 24.7 dB and noise figure of 27.7 dB.

The loss of the RF filter due to the low-biasing technique can be simply compensated by another EDFA at the output of the MZM [191]. We carry out the filter gain and noise figure characterization in the same way, which is shown in Figure 5.11 b. In this scenario, the optical power is limited by the maximum input power to the PD, where we operated at around 25 mW. We can see that the filter gain increases first with the DC tuned from quadrature towards MITP, and suddenly decreases when it is very close to MITP. This is because the power of modulated sidebands (signals) are very small at the beginning, the filter gain increases when the power between the carriers and signals become more balanced, as the gain relates to the product of the signals and carriers power. And the gain reaches peak when the power of them become comparable. After that, the filter gain drops quickly due to the weak carriers as very close to the null point. In terms of noise figure, it reduces at the beginning due to the low-biasing, but increases dramatically afterwards when the input power to the EDFA is too low, which tends to amplify more noise instead of the carriers and signals. Overall, we could achieve positive RF filter gain (+1.6 dB) with noise figure of 29.8 dB.

The further optimization of the filter link performance relies on the improvement of the components used in the link, such as MZM with lower  $V_\pi$  and higher maximum input power, EDFA with lower noise figure, and PD with higher responsivity and higher power handling capability. We note that MZM with  $V_\pi$  as low as 1.4 V [86] is now feasible by integrated solution, which is much lower than the commercial MZM. The optimal setup will use the low-biasing technique and bypass the EDFA after the MZM, while still achieving relatively high RF gain.

**Comparison with RF photonic filters of the same type.** As summarized in Table 5.1, our soliton-based RF filters presented in this chapter are compared with other RF photonic filters based on various multi-wavelength sources. First, we see that the MSSR achieved by soliton microcomb is comparable or even better than other implementations that do not require pulse shapers, such as combs based on cascaded modulators [37], laser arrays [175] or mode-locked lasers [179, 180], while none of them are integrated solutions regarding the light sources. Second, all of the past microcomb-based RF filters require, to our knowledge, two high fidelity pulse shapers [81–83], in order to equalize the largely unbalanced comb line intensity in the complex microcomb states. The achievable MSSR is indeed higher as expected, due to the fine equalization of comb amplitudes. Without pulse shapers, however, these approaches are not able to achieve similar MSSR nor tunability. In our case, the MSSR is mainly limited by the spectral roughness induced by mode crossings. One could envision combining our current implementation with an integrated spectral shaper as previously demonstrated [46]. The integrated shaper can enhance our filters with improved MSSR and faster reconfiguration, while the soliton microcombs can greatly simplify the EO combs previously used [46]. It is worth noting that using integrated shaper for comb equalization in complex microcomb spectra would be inefficient, due to the shaper's limited extinction ratio. Thus, the ability to control the soliton states among microcombs is truly essential for practical implementation.

From the table, it is also evident that only few past works report the link performances of comb-based RF filters. The simple optimization of our soliton-based RF filter link is carried

Table 5.1 – Comparison of RF photonic filters based on multi-wavelength sources.

Reference	Light source	Pulse shaper	MSSR	Passband frequency	Gain	Noise figure	Photonic integration
ref [180]	MLL	N	20.4 dB	0.6 – 1.8 GHz	N/A	N/A	N
ref [179]	MLL	N	24 dB	8 – 16 GHz	N/A	N/A	N
ref [175]	Laser array	N	10 dB	0 – 50 GHz	N/A	N/A	delay line
ref [37]	EO comb (4 EOMs)	N	28.2 dB/61 dB w/wo nonlinear shaping	0.8 – 10.4 GHz	–40 dB	N/A	N
ref [155]	FP-EO comb (1 EOM)	Y, one	30 dB	2.6 – 13.9 GHz	N/A	N/A	N
ref [192]	EO comb (4 EOMs)	Y, one	32 dB	2 – 8 GHz	0 dB	24 dB	N
ref [46]	EO comb (7 EOMs)	Y, two	35 dB	0.6 – 4 GHz	–3 dB	N/A	spectral shaper
ref [81]	microcomb	Y, two	25 dB	2.5 – 17.5 GHz	N/A	N/A	microresonator
ref [82]	microcomb	Y, two	48.9 dB	1.4 – 11.5 GHz	N/A	N/A	microresonator
ref [83]	microcomb	Y, two	N/A	3.2 – 19.4 GHz	N/A	N/A	microresonator
This work	microcomb	N	25.6 dB	0.8 – 16.2 GHz	1.6 dB	29.8 dB	microresonator

Note: the best values of parameters extracted from the references are put in the table.

Y: Yes; N: no; N/A: not available. MLL: mode-locked laser; EO: electro-optic; EOM: electro-optic modulator; FP: Fabry-Perot.

out as detailed above, which is very close to the optimized performances of the state-of-the-art comb-based RF filters [192]. Nevertheless, the link performances of RF photonic filters in general are far from being comparable to that of pure microwave solutions. Additionally, we achieve here widely reconfigurable RF photonic filters from 0.8 GHz to 16.2 GHz covering the whole RF FSR, taking into account both passbands obtained from TSM spectra. This multi-octave filter operation is generally considered challenging by pure RF engineering, especially at higher carrier frequency towards millimeter wave or terahertz wave. Notably, unlike many other RF photonic filters equipped with the external shaping elements, the presented RF filters cannot be continuously tuned due to the inherent regulation of solitons. However, the exploration of multiple resonances could dramatically enrich the achievable RF filters, while the possible controlled mode interaction [123] or using dichromatic pumps [193] may empower the soliton-based RF filters with continuous tuning ability. Moreover, additional functionalities such as photonic down-conversion of microwave signals can be simultaneously realized while filtering, without involving electrical mixer and external local oscillators [194].

In fact, the microcomb FSR will act as the local oscillator that naturally provides the stable RF frequency. Thanks to the large microcomb FSR, this will be very promising for on-chip THz wave signal processing.

## 5.6 Conclusions

In summary, we demonstrate reconfigurable soliton-based RF photonic filters using simplified approaches. Contrary to previous demonstrations where pulse shapers are necessary to obtain decent passband responses [81–83], the proposed schemes are intrinsically well-shaped with the smooth spectral envelopes of solitons. More importantly, we harness various inherent soliton states of a microresonator, like PSC and TSM, for RF filter reconfiguration at no additional cost. The diversity and regularization of soliton formats in microresonator are investigated in the favor of RF photonic filters. To certain extent, these internal shaping of soliton states could be in place of substantial efforts made in the past for reconfiguring the comb-based RF filters, such as using interferometric architecture [37, 81], programmable pulse shaping [82, 155], or Talbot-based signal processor [180]. Admittedly, although our soliton-based RF filters are much simpler than the previous microcomb-based RF filters [81–83] as we eliminate the use of two bulky pulse shapers here, the form factor is not yet as compact as their electrical counterparts. Nevertheless, the basic components of soliton-based RF filters can be integrated [175]. The recent advancements on the integration between laser chip and microresonator [195, 196], as well as the possibility to replace the long fiber with an integrated photonic crystal delay line [175], can be further connected to the current work for miniaturization. To conclude, through internal shaping of the soliton states, the presented work significantly reduces the system complexity, size, and cost of the microcomb-based RF filters, while preserving wide reconfigurability. The proposed scheme serves as a stepping stone for chip-scale, cost-effective, and widely reconfigurable microcomb-based RF filters.

## 6 Conclusions and perspectives

The thesis has explored versatile shaping of optical frequency combs, specifically for the utilization in microwave photonics and optical telecommunications. Both EO combs and soliton microcombs are addressed, together with diverse internal and external shaping techniques of them for different application purposes. In this closing chapter, the conclusions of the presented research works are drawn. Further, some possible continuation and outlook of the thesis are also suggested.

**Chapter 3** is dedicated to optical sinc pulse shaping. A flexible optical sinc pulse generation is enabled by controlling the amplitude and phase of each pair of comb lines electronically. Such EO pulse synthesis is fully reconfigurable in terms of repetition-rate and pulse width, while only relies on a single MZM stage. The single MZM approach features some unique advantages compared to the operation based on cascaded MZMs [63]. For instance, the complementary nature of a single dual-output MZM would simultaneously create bright and dark sinc pulse pair, which can be employed in Nyquist OTDM system to attain add-drop functionalities. The performance and detailed implementation of such ADM scheme is also investigated by simulation. While from another point of view, the rectangular spectra of optical sinc pulses are adapted for RF photonics to synthesize RF filters of sinc shapes. The center frequencies and bandwidths of such filters are easily reconfigurable thanks to the full flexibility on the EO comb generator.

In terms of possible future research, one of the directions is to pursue optical sinc pulses with shorter pulse widths demanded in telecommunications. With the proposed sinc pulse generator, although being fully flexible, the achievable pulse width is fundamentally limited by the MZM bandwidth. One interesting approach is to migrate the acousto-optic frequency-shifting loop for the optical sinc pulse generator [197]. Instead of acousto-optic modulation, a DP-MZM performing equivalent SSB modulation may be used to achieve comb FSR compatible with optical communications. Besides, it is worthwhile to experimentally verify the proposed ADM scheme in Nyquist OTDM systems.

**Chapter 4** inspects the Talbot shaping of both optical frequency combs and OAM modes

of light. First, a novel implementation of temporal Talbot multiplier is proposed based on an optical TDL structure. While mostly being used for spectral amplitude filtering, such architecture is also found to implement the temporal Talbot operation, as well as versatile combinations of amplitude and phase filtering. The optical TDL structure is fully amenable to photonic integration [48], hence is promising for on-chip temporal Talbot shaping of optical combs. Similar Talbot shaping concept is then applied to the OAM modes of light. The azimuthal Talbot effect is then demonstrated when a number of OAM modes of light are superimposed with Talbot phases. It is manifested by the multiplication of petals in the azimuthal angle, without changing their underlying OAM components.

Since there is few integrated temporal Talbot multiplier to date [73], the on-chip realization of the proposed temporal Talbot scheme is worth demonstrating. While regarding the shaping of OAM modes, the current implementation of the azimuthal Talbot effect is made possible only at the generation stage. A logical next step is to realize such shaping externally on an existing OAM spectrum. This could possibly be implemented in an OAM shaper demonstrated recently [170], and would eventually trigger new interest in OAM-based classical and quantum information processing. Moreover, the Talbot shaping of OAM modes is just one specific case that exemplifies the duality between comb mode and OAM mode, while other techniques of shaping the OAM and comb may be borrowed interchangeably.

**Chapter 5** investigates the internal shaping of soliton states in microresonators for RF photonic filtering. By exploiting the rich soliton configurations, all-optical reconfiguration of the RF filters are demonstrated. Among others, perfect soliton crystals and two-soliton states are utilized, which respectively divide and translate the center frequencies of their corresponding RF filters. Notably, sufficient suppression ratios of such filters are automatically guaranteed by the smooth spectral envelopes of solitons. Leveraging the inherent soliton states bypasses external pulse shaping elements that are previously required. Also, the soliton-based RF filters are compared with other comb-based RF filters, and their advantages and limitations are discussed. Overall, it provides an elegant approach to reduce the cost, size, and complexity of reconfigurable microcomb-based RF filters.

As for possible extension of the current RF filter work, photonic down-conversion of the RF signals may be achieved simultaneously while filtering [194]. Indeed, the comb FSRs of mode-locked microcomb states naturally function as local oscillators. The optimization of link performance is another important metrics pursued in RF photonic filter community [191]. Except for RF filtering, the inherent versatility of soliton states may also facilitate other microwave photonic applications. For instance, in comb-based true-time delay phase array antennas [181], the FSR variations of perfect soliton crystals could empower such systems with beam-steering capability.

# Bibliography

1. Jones, D. J. *et al.* Carrier-envelope phase control of femtosecond mode-locked lasers and direct optical frequency synthesis. *Science* **288**, 635–639 (2000).
2. Udem, T., Holzwarth, R. & Hänsch, T. W. Optical frequency metrology. *Nature* **416**, 233–237 (2002).
3. Cundiff, S. T. & Ye, J. Colloquium: Femtosecond optical frequency combs. *Reviews of Modern Physics* **75**, 325 (2003).
4. Diddams, S. A. The evolving optical frequency comb. *JOSA B* **27**, B51–B62 (2010).
5. Newbury, N. R. Searching for applications with a fine-tooth comb. *Nature photonics* **5**, 186–188 (2011).
6. Picqué, N. & Hänsch, T. W. Frequency comb spectroscopy. *Nature Photonics* **13**, 146–157 (2019).
7. Fortier, T. & Baumann, E. 20 years of developments in optical frequency comb technology and applications. *Communications Physics* **2**, 1–16 (2019).
8. Weiner, A. *Ultrafast optics* (John Wiley & Sons, 2011).
9. Keller, U. Ultrafast solid-state laser oscillators: a success story for the last 20 years with no end in sight. *Applied Physics B* **100**, 15–28 (2010).
10. Fermand, M. E. & Hartl, I. Ultrafast fiber laser technology. *IEEE Journal of Selected Topics in Quantum Electronics* **15**, 191–206 (2009).
11. Keller, U. *et al.* Semiconductor saturable absorber mirrors (SESAM's) for femtosecond to nanosecond pulse generation in solid-state lasers. *IEEE Journal of selected topics in QUANTUM ELECTRONICS* **2**, 435–453 (1996).
12. Carlson, D. R. *et al.* Ultrafast electro-optic light with subcycle control. *Science* **361**, 1358–1363 (2018).
13. Parriaux, A., Hammani, K. & Millot, G. Electro-optic frequency combs. *Advances in Optics and Photonics* **12**, 223–287 (2020).
14. Kippenberg, T. J., Holzwarth, R. & Diddams, S. A. Microresonator-based optical frequency combs. *science* **332**, 555–559 (2011).



## Bibliography

---

15. Pasquazi, A. *et al.* Micro-combs: A novel generation of optical sources. *Physics Reports* **729**, 1–81 (2018).
16. Kippenberg, T. J., Gaeta, A. L., Lipson, M. & Gorodetsky, M. L. Dissipative Kerr solitons in optical microresonators. *Science* **361** (2018).
17. Liu, J. *et al.* Ultralow-power chip-based soliton microcombs for photonic integration. *Optica* **5**, 1347–1353 (2018).
18. Hugl, A., Villares, G., Blaser, S., Liu, H. & Faist, J. Mid-infrared frequency comb based on a quantum cascade laser. *Nature* **492**, 229–233 (2012).
19. Faist, J. *et al.* Quantum cascade laser frequency combs. *Nanophotonics* **5**, 272–291 (2016).
20. Ma, L.-S. *et al.* Optical frequency synthesis and comparison with uncertainty at the 10<sup>-19</sup> level. *Science* **303**, 1843–1845 (2004).
21. Coddington, I., Newbury, N. & Swann, W. Dual-comb spectroscopy. *Optica* **3**, 414–426 (2016).
22. Jang, Y.-S. & Kim, S.-W. Distance measurements using mode-locked lasers: a review. *Nanomanufacturing and Metrology* **1**, 131–147 (2018).
23. Coddington, I., Swann, W. C., Nenadovic, L. & Newbury, N. R. Rapid and precise absolute distance measurements at long range. *Nature photonics* **3**, 351–356 (2009).
24. Murphy, M. *et al.* High-precision wavelength calibration of astronomical spectrographs with laser frequency combs. *Monthly Notices of the Royal Astronomical Society* **380**, 839–847 (2007).
25. Metcalf, A. J. *et al.* Stellar spectroscopy in the near-infrared with a laser frequency comb. *Optica* **6**, 233–239 (2019).
26. Obrzud, E. *et al.* A microphotonic astrocomb. *Nature Photonics* **13**, 31–35 (2019).
27. Hillerkuss, D. *et al.* 26 Tbit s<sup>-1</sup> line-rate super-channel transmission utilizing all-optical fast Fourier transform processing. *Nature photonics* **5**, 364–371 (2011).
28. Marin-Palomo, P. *et al.* Microresonator-based solitons for massively parallel coherent optical communications. *Nature* **546**, 274–279 (2017).
29. Lundberg, L. *et al.* Phase-coherent lightwave communications with frequency combs. *Nature communications* **11** (2020).
30. Nakazawa, M., Yamamoto, T. & Tamura, K. 1.28 Tbit/s–70 km OTDM transmission using third-and fourth-order simultaneous dispersion compensation with a phase modulator. *Electronics letters* **36**, 2027–2029 (2000).
31. Mulvad, H. C. H. *et al.* Demonstration of 5.1 Tbit/s data capacity on a single-wavelength channel. *Optics Express* **18**, 1438–1443 (2010).
32. Capmany, J. & Novak, D. Microwave photonics combines two worlds. *Nature photonics* **1**, 319–330 (2007).

33. Yao, J. Microwave photonics. *Journal of lightwave technology* **27**, 314–335 (2009).
34. Fortier, T. M. *et al.* Generation of ultrastable microwaves via optical frequency division. *Nature Photonics* **5**, 425–429 (2011).
35. Xie, X. *et al.* Photonic microwave signals with zeptosecond-level absolute timing noise. *nature photonics* **11**, 44–47 (2017).
36. Huang, C.-B., Jiang, Z., Leaird, D., Caraquiten, J. & Weiner, A. Spectral line-by-line shaping for optical and microwave arbitrary waveform generations. *Laser & Photonics Reviews* **2**, 227–248 (2008).
37. Supradeepa, V. *et al.* Comb-based radiofrequency photonic filters with rapid tunability and high selectivity. *Nature Photonics* **6**, 186–194 (2012).
38. Xue, X., Zheng, X., Zhou, B. & Weiner, A. M. Microresonator frequency combs for integrated microwave photonics. *IEEE Photonics Technology Letters* **30**, 1814–1817 (2018).
39. Torres-Company, V. & Weiner, A. M. Optical frequency comb technology for ultra-broadband radio-frequency photonics. *Laser & Photonics Reviews* **8**, 368–393 (2014).
40. Weiner, A. M. Femtosecond pulse shaping using spatial light modulators. *Review of scientific instruments* **71**, 1929–1960 (2000).
41. Schröder, J. *et al.* An optical FPGA: Reconfigurable simultaneous multi-output spectral pulse-shaping for linear optical processing. *Optics express* **21**, 690–697 (2013).
42. Willits, J. T., Weiner, A. M. & Cundiff, S. T. Line-by-line pulse shaping with spectral resolution below 890 MHz. *Optics express* **20**, 3110–3117 (2012).
43. Jiang, Z., Huang, C.-B., Leaird, D. E. & Weiner, A. M. Optical arbitrary waveform processing of more than 100 spectral comb lines. *nature photonics* **1**, 463–467 (2007).
44. Ferdous, F. *et al.* Spectral line-by-line pulse shaping of on-chip microresonator frequency combs. *Nature Photonics* **5**, 770–776 (2011).
45. Fontaine, N. *et al.* 32 phase  $\times$  32 amplitude optical arbitrary waveform generation. *Optics Letters* **32**, 865–867 (2007).
46. Metcalf, A. J. *et al.* Integrated line-by-line optical pulse shaper for high-fidelity and rapidly reconfigurable RF-filtering. *Optics Express* **24**, 23925–23940 (2016).
47. Liao, S. *et al.* Arbitrary waveform generator and differentiator employing an integrated optical pulse shaper. *Optics express* **23**, 12161–12173 (2015).
48. Xie, Y., Zhuang, L. & Lowery, A. J. Picosecond optical pulse processing using a terahertz-bandwidth reconfigurable photonic integrated circuit. *Nanophotonics* **7**, 837–852 (2018).
49. Schnébelin, C., Azaña, J. & de Chatellus, H. G. Programmable broadband optical field spectral shaping with megahertz resolution using a simple frequency shifting loop. *Nature communications* **10**, 1–11 (2019).
50. Kuo, F.-M. *et al.* Remotely up-converted 20-Gbit/s error-free wireless on-off-keying data transmission at W-band using an ultra-wideband photonic transmitter-mixer. *IEEE Photonics Journal* **3**, 209–219 (2011).

## Bibliography

---

51. Cole, D. C., Papp, S. B. & Diddams, S. A. Downsampling of optical frequency combs. *JOSA B* **35**, 1666–1673 (2018).
52. Azaña, J. & Muriel, M. A. Temporal self-imaging effects: theory and application for multiplying pulse repetition rates. *IEEE Journal of selected topics in quantum electronics* **7**, 728–744 (2001).
53. Caraquitená, J., Beltrán, M., Llorente, R., Martí, J. & Muriel, M. A. Spectral self-imaging effect by time-domain multilevel phase modulation of a periodic pulse train. *Optics letters* **36**, 858–860 (2011).
54. Meloni, G. *et al.* 250-times repetition frequency multiplication for 2.5 THz clock signal generation. *Electronics Letters* **41**, 1294–1295 (2005).
55. Azana, J. & Muriel, M. A. Technique for multiplying the repetition rates of periodic trains of pulses by means of a temporal self-imaging effect in chirped fiber gratings. *Optics letters* **24**, 1672–1674 (1999).
56. Caraquitená, J., Jiang, Z., Leaird, D. E. & Weiner, A. M. Tunable pulse repetition-rate multiplication using phase-only line-by-line pulse shaping. *Optics letters* **32**, 716–718 (2007).
57. Malacarne, A. & Azaña, J. Discretely tunable comb spacing of a frequency comb by multilevel phase modulation of a periodic pulse train. *Optics Express* **21**, 4139–4144 (2013).
58. Romero Cortés, L., Maram, R., Guillet de Chatellus, H. & Azaña, J. Arbitrary Energy-Preserving Control of Optical Pulse Trains and Frequency Combs through Generalized Talbot Effects. *Laser & Photonics Reviews* **13**, 1900176 (2019).
59. Maram, R., Van Howe, J., Li, M. & Azaña, J. Noiseless intensity amplification of repetitive signals by coherent addition using the temporal Talbot effect. *Nature communications* **5**, 1–11 (2014).
60. Lancis, J., Andrés, P., *et al.* Lossless equalization of frequency combs. *Optics letters* **33**, 1822–1824 (2008).
61. Wu, R., Supradeepa, V., Long, C. M., Leaird, D. E. & Weiner, A. M. Generation of very flat optical frequency combs from continuous-wave lasers using cascaded intensity and phase modulators driven by tailored radio frequency waveforms. *Optics letters* **35**, 3234–3236 (2010).
62. Karpov, M. *et al.* Dynamics of soliton crystals in optical microresonators. *Nature Physics* **15**, 1071–1077 (2019).
63. Soto, M. A. *et al.* Optical sinc-shaped Nyquist pulses of exceptional quality. *Nature communications* **4**, 1–11 (2013).
64. Nakazawa, M., Hirooka, T., Ruan, P. & Guan, P. Ultrahigh-speed “orthogonal” TDM transmission with an optical Nyquist pulse train. *Optics express* **20**, 1129–1140 (2012).
65. Leuthold, J. & Brès, C.-S. in *All-Optical Signal Processing* 217–260 (Springer, 2015).

66. Wu, J. *et al.* Investigation on Nyquist pulse generation using a single dual-parallel Mach-Zehnder modulator. *Optics express* **22**, 20463–20472 (2014).
67. Yokota, N., Igarashi, R. & Yasaka, H. Optical Nyquist pulse generation by using a dual-electrode Mach-Zehnder modulator. *Optics Letters* **42**, 1856–1859 (2017).
68. Harako, K., Otuya, D. O., Kasai, K., Hirooka, T. & Nakazawa, M. High-performance TDM demultiplexing of coherent Nyquist pulses using time-domain orthogonality. *Optics express* **22**, 29456–29464 (2014).
69. Geng, Z., Kong, D., Rozental, V., Lowery, A. J. & Corcoran, B. Optical sampling to enhance Nyquist-shaped signal detection under limited receiver bandwidth. *Optics express* **27**, 24007–24017 (2019).
70. Fabbri, S. J. *et al.* Experimental implementation of an all-optical interferometric drop, add, and extract multiplexer for superchannels. *Journal of Lightwave Technology* **33**, 1351–1357 (2015).
71. Wun, J.-M. *et al.* Photonic high-power continuous wave THz-wave generation by using flip-chip packaged uni-traveling carrier photodiodes and a femtosecond optical pulse generator. *Journal of Lightwave Technology* **34**, 1387–1397 (2015).
72. Seghilani, M., Maram, R. & Azaña, J. Mitigating nonlinear propagation impairments of ultrashort pulses by fractional temporal self-imaging. *Optics Letters* **42**, 879–882 (2017).
73. Kaushal, S. & Azaña, J. On-chip dispersive phase filters for optical processing of periodic signals. *Optics Letters* **45**, 4603–4606 (2020).
74. Yao, A. M. & Padgett, M. J. Orbital angular momentum: origins, behavior and applications. *Advances in Optics and Photonics* **3**, 161–204 (2011).
75. Padgett, M. J. Orbital angular momentum 25 years on. *Optics express* **25**, 11265–11274 (2017).
76. Xie, G. *et al.* Using a complex optical orbital-angular-momentum spectrum to measure object parameters. *Optics Letters* **42**, 4482–4485 (2017).
77. Xie, G. *et al.* Spatial light structuring using a combination of multiple orthogonal orbital angular momentum beams with complex coefficients. *Optics Letters* **42**, 991–994 (2017).
78. Wu, J. *et al.* RF photonics: an optical microcombs' perspective. *IEEE Journal of Selected Topics in Quantum Electronics* **24**, 1–20 (2018).
79. Capmany, J., Ortega, B. & Pastor, D. A tutorial on microwave photonic filters. *Journal of Lightwave Technology* **24**, 201–229 (2006).
80. Hamidi, E., Leaird, D. E. & Weiner, A. M. Tunable programmable microwave photonic filters based on an optical frequency comb. *IEEE Transactions on Microwave Theory and Techniques* **58**, 3269–3278 (2010).
81. Xue, X. *et al.* Programmable single-bandpass photonic RF filter based on Kerr comb from a microring. *Journal of Lightwave Technology* **32**, 3557–3565 (2014).

## Bibliography

---

82. Xu, X. *et al.* Advanced adaptive photonic RF filters with 80 taps based on an integrated optical micro-comb source. *Journal of Lightwave Technology* **37**, 1288–1295 (2019).
83. Xu, X. *et al.* High performance RF filters via bandwidth scaling with Kerr micro-combs. *APL Photonics* **4**, 026102 (2019).
84. Soto, M. A., Bolognini, G., Di Pasquale, F. & Thévenaz, L. Simplex-coded BOTDA fiber sensor with 1 m spatial resolution over a 50 km range. *Optics letters* **35**, 259–261 (2010).
85. Lu, H.-H., Weiner, A. M., Lougovski, P. & Lukens, J. M. Quantum information processing with frequency-comb qudits. *IEEE Photonics Technology Letters* **31**, 1858–1861 (2019).
86. Wang, C. *et al.* Integrated lithium niobate electro-optic modulators operating at CMOS-compatible voltages. *Nature* **562**, 101–104 (2018).
87. Marpaung, D., Yao, J. & Capmany, J. Integrated microwave photonics. *Nature photonics* **13**, 80–90 (2019).
88. Boyd, R. W. *Nonlinear optics* (Academic press, 2020).
89. Wang, Q., Huo, L., Xing, Y. & Zhou, B. Ultra-flat optical frequency comb generator using a single-driven dual-parallel Mach–Zehnder modulator. *Optics Letters* **39**, 3050–3053 (2014).
90. Winzer, P. J., Neilson, D. T. & Chraplyvy, A. R. Fiber-optic transmission and networking: the previous 20 and the next 20 years. *Optics express* **26**, 24190–24239 (2018).
91. Liu, Y., Choudhary, A., Marpaung, D. & Eggleton, B. J. Integrated microwave photonic filters. *Advances in Optics and Photonics* **12**, 485–555 (2020).
92. Chen, X., Cho, J., Adamiecki, A. & Winzer, P. 16384-QAM transmission at 10 GBd over 25-km SSMF using polarization-multiplexed probabilistic constellation shaping in 45th European Conference on Optical Communication (ECOC 2019) (2019), 1–4.
93. Marpaung, D. *et al.* Si<sub>3</sub>N<sub>4</sub> ring resonator-based microwave photonic notch filter with an ultrahigh peak rejection. *Optics express* **21**, 23286–23294 (2013).
94. Shahnian, S., Pagani, M., Morrison, B., Eggleton, B. J. & Marpaung, D. Independent manipulation of the phase and amplitude of optical sidebands in a highly-stable RF photonic filter. *Optics express* **23**, 23278–23286 (2015).
95. Booth, M. J. Adaptive optical microscopy: the ongoing quest for a perfect image. *Light: Science & Applications* **3**, e165–e165 (2014).
96. Papadopoulos, I. N., Farahi, S., Moser, C. & Psaltis, D. High-resolution, lensless endoscope based on digital scanning through a multimode optical fiber. *Biomedical optics express* **4**, 260–270 (2013).
97. Eriksen, R. L., Daria, V. R. & Glückstad, J. Fully dynamic multiple-beam optical tweezers. *Optics Express* **10**, 597–602 (2002).
98. Forbes, A. Structured light from lasers. *Laser & Photonics Reviews* **13**, 1900140 (2019).
99. Carpenter, J., Thomsen, B. C. & Wilkinson, T. D. Degenerate mode-group division multiplexing. *Journal of Lightwave Technology* **30**, 3946–3952 (2012).

100. Dong, J., Rafayelyan, M., Krzakala, F. & Gigan, S. Optical reservoir computing using multiple light scattering for chaotic systems prediction. *IEEE Journal of Selected Topics in Quantum Electronics* **26**, 1–12 (2019).
101. Rosales-Guzmán, C. & Forbes, A. *How to shape light with spatial light modulators* (SPIE Press, 2017).
102. Arrizón, V., Ruiz, U., Carrada, R. & González, L. A. Pixelated phase computer holograms for the accurate encoding of scalar complex fields. *JOSA A* **24**, 3500–3507 (2007).
103. Forbes, A., Dudley, A. & McLaren, M. Creation and detection of optical modes with spatial light modulators. *Advances in Optics and Photonics* **8**, 200–227 (2016).
104. Mendoza-Yero, O., Mínguez-Vega, G. & Lancis, J. Encoding complex fields by using a phase-only optical element. *Optics letters* **39**, 1740–1743 (2014).
105. Goodman, J. W. *Introduction to Fourier optics* (Roberts and Company Publishers, 2005).
106. Cundiff, S. T. & Weiner, A. M. Optical arbitrary waveform generation. *Nature Photonics* **4**, 760–766 (2010).
107. Wen, J., Zhang, Y. & Xiao, M. The Talbot effect: recent advances in classical optics, nonlinear optics, and quantum optics. *Advances in optics and photonics* **5**, 83–130 (2013).
108. Talbot, H. F. LXXVI. Facts relating to optical science. No. IV. *The London, Edinburgh, and Dublin Philosophical Magazine and Journal of Science* **9**, 401–407 (1836).
109. Soldano, L. B. & Pennings, E. C. Optical multi-mode interference devices based on self-imaging: principles and applications. *Journal of lightwave technology* **13**, 615–627 (1995).
110. Bachmann, M., Besse, P. A. & Melchior, H. General self-imaging properties in  $N \times N$  multimode interference couplers including phase relations. *Applied optics* **33**, 3905–3911 (1994).
111. Cortés, L. R., de Chatellus, H. G. & Azaña, J. On the generality of the Talbot condition for inducing self-imaging effects on periodic objects. *Optics Letters* **41**, 340–343 (2016).
112. Azana, J. & Muriel, M. A. Temporal Talbot effect in fiber gratings and its applications. *Applied optics* **38**, 6700–6704 (1999).
113. Lei, L. *et al.* Observation of spectral self-imaging by nonlinear parabolic cross-phase modulation. *Optics letters* **40**, 5403–5406 (2015).
114. Fernández-Pousa, C. R. On the structure of quadratic Gauss sums in the Talbot effect. *JOSA A* **34**, 732–742 (2017).
115. Berndt, B. C. & Evans, R. J. The determination of Gauss sums. *Bulletin of the American Mathematical Society* **5**, 107–129 (1981).
116. Maram, R., Cortés, L. R., Van Howe, J. & Azaña, J. Energy-preserving arbitrary repetition-rate control of periodic pulse trains using temporal Talbot effects. *Journal of Lightwave Technology* **35**, 658–668 (2017).

## Bibliography

---

117. Fernández-Pousa, C. R., Maram, R. & Azaña, J. CW-to-pulse conversion using temporal Talbot array illuminators. *Optics Letters* **42**, 2427–2430 (2017).
118. Huang, C.-B. *et al.* Loss-less pulse intensity repetition-rate multiplication using optical all-pass filtering. *IEEE Photonics Technology Letters* **12**, 167–169 (2000).
119. Vahala, K. J. Optical microcavities. *nature* **424**, 839–846 (2003).
120. Kovach, A. *et al.* Emerging material systems for integrated optical Kerr frequency combs. *Advances in Optics and Photonics* **12**, 135–222 (2020).
121. Godey, C., Balakireva, I. V., Coillet, A. & Chembo, Y. K. Stability analysis of the spatiotemporal Lugiato-Lefever model for Kerr optical frequency combs in the anomalous and normal dispersion regimes. *Physical Review A* **89**, 063814 (2014).
122. Liu, Y. *et al.* Investigation of mode coupling in normal-dispersion silicon nitride microresonators for Kerr frequency comb generation. *optica* **1**, 137–144 (2014).
123. Xue, X. *et al.* Normal-dispersion microcombs enabled by controllable mode interactions. *Laser & Photonics Reviews* **9**, L23–L28 (2015).
124. Herr, T. *et al.* Temporal solitons in optical microresonators. *Nature Photonics* **8**, 145–152 (2014).
125. Brasch, V. *et al.* Photonic chip-based optical frequency comb using soliton Cherenkov radiation. *Science* **351**, 357–360 (2016).
126. Wang, C. *et al.* Monolithic lithium niobate photonic circuits for Kerr frequency comb generation and modulation. *Nature communications* **10**, 1–6 (2019).
127. Billat, A. *et al.* Large second harmonic generation enhancement in Si<sub>3</sub>N<sub>4</sub> waveguides by all-optically induced quasi-phase-matching. *Nature communications* **8**, 1–7 (2017).
128. Kippenberg, T., Spillane, S. & Vahala, K. Kerr-nonlinearity optical parametric oscillation in an ultrahigh-Q toroid microcavity. *Physical review letters* **93**, 083904 (2004).
129. Del’Haye, P. *et al.* Optical frequency comb generation from a monolithic microresonator. *Nature* **450**, 1214–1217 (2007).
130. Levy, J. S. *et al.* CMOS-compatible multiple-wavelength oscillator for on-chip optical interconnects. *Nature photonics* **4**, 37–40 (2010).
131. Herr, T. *et al.* Universal formation dynamics and noise of Kerr-frequency combs in microresonators. *Nature photonics* **6**, 480–487 (2012).
132. Leo, F. *et al.* Temporal cavity solitons in one-dimensional Kerr media as bits in an all-optical buffer. *Nature Photonics* **4**, 471–476 (2010).
133. Coillet, A. *et al.* Azimuthal Turing patterns, bright and dark cavity solitons in Kerr combs generated with whispering-gallery-mode resonators. *IEEE Photonics Journal* **5**, 6100409–6100409 (2013).
134. Xue, X., Wang, P.-H., Xuan, Y., Qi, M. & Weiner, A. M. Microresonator Kerr frequency combs with high conversion efficiency. *Laser & Photonics Reviews* **11**, 1600276 (2017).

135. Obrzud, E., Lecomte, S. & Herr, T. Temporal solitons in microresonators driven by optical pulses. *Nature Photonics* **11**, 600 (2017).
136. Xue, X. *et al.* Mode-locked dark pulse Kerr combs in normal-dispersion microresonators. *Nature Photonics* **9**, 594–600 (2015).
137. Parra-Rivas, P., Gomila, D., Knobloch, E., Coen, S. & Gelens, L. Origin and stability of dark pulse Kerr combs in normal dispersion resonators. *Optics Letters* **41**, 2402–2405 (2016).
138. Matsko, A. B., Savchenkov, A. A., Strekalov, D., Ilchenko, V. S. & Maleki, L. Optical hyperparametric oscillations in a whispering-gallery-mode resonator: Threshold and phase diffusion. *Physical Review A* **71**, 033804 (2005).
139. Ikeda, K. Multiple-valued stationary state and its instability of the transmitted light by a ring cavity system. *Optics communications* **30**, 257–261 (1979).
140. Haelterman, M., Trillo, S. & Wabnitz, S. Dissipative modulation instability in a nonlinear dispersive ring cavity. *Optics communications* **91**, 401–407 (1992).
141. Matsko, A. *et al.* Mode-locked Kerr frequency combs. *Optics letters* **36**, 2845–2847 (2011).
142. Agrawal, G. P. in *Nonlinear Science at the Dawn of the 21st Century* 195–211 (Springer, 2000).
143. Hu, J., Fabbri, S. J. & Brès, C.-S. *Flexible width nyquist pulse based on a single Mach-Zehnder modulator* in *2018 Conference on Lasers and Electro-Optics (CLEO)* (2018), 1–2.
144. Hu, J., Fabbri, S. J. & Brès, C.-S. *Reconfigurable filter-free sinc-shaped RF photonic filters based on rectangular optical frequency comb* in *2018 Conference on Lasers and Electro-Optics (CLEO)* (2018), 1–2.
145. Hu, J., Kharitonov, S., Fabbri, S. J. & Brès, C.-S. *Add-Drop Multiplexing Architecture for Nyquist OTDM Signals Based on a Single Mach-Zehnder Modulator* in *Asia Communications and Photonics Conference* (2019), M4A–38.
146. Wang, J., Xie, C. & Pan, Z. Generation of spectrally efficient Nyquist-WDM QPSK signals using digital FIR or FDE filters at transmitters. *Journal of lightwave technology* **30**, 3679–3686 (2012).
147. Tan, H. N., Inoue, T., Tanizawa, K., Kurosu, T. & Namiki, S. Optical Nyquist filtering for elastic OTDM signals: fundamentals and demonstrations. *Journal of Lightwave Technology* **33**, 1014–1026 (2015).
148. Corcoran, B. *et al.* Multipass performance of a chip-enhanced WSS for Nyquist-WDM sub-band switching. *Journal of Lightwave Technology* **34**, 1824–1830 (2016).
149. Nakazawa, M., Yoshida, M. & Hirooka, T. The nyquist laser. *Optica* **1**, 15–22 (2014).
150. Wang, D., Huo, L., Xing, Y., Jiang, X. & Lou, C. Optical Nyquist pulse generation using a time lens with spectral slicing. *Optics Express* **23**, 4329–4339 (2015).



## Bibliography

---

151. Tan, H. N., Inoue, T., Kurosu, T. & Namiki, S. Wavelength translation of dual-polarization phase-modulated Nyquist OTDM at terabit/s. *Journal of Lightwave Technology* **34**, 633–642 (2015).
152. Fabbri, S., Sygletos, S. & Ellis, A. *Multi-harmonic optical comb generation* in 2012 38th European Conference and Exhibition on Optical Communications (2012), 1–3.
153. Song, M. *et al.* Reconfigurable and tunable flat-top microwave photonic filters utilizing optical frequency combs. *IEEE Photonics Technology Letters* **23**, 1618–1620 (2011).
154. Zhu, Z. *et al.* All-positive-coefficient microwave photonic filter with rectangular response. *Optics Letters* **42**, 3012–3015 (2017).
155. Zhu, X., Chen, F., Peng, H. & Chen, Z. Novel programmable microwave photonic filter with arbitrary filtering shape and linear phase. *Optics Express* **25**, 9232–9243 (2017).
156. Shoaie, M. A., Vedadi, A. & Brès, C.-S. *A simple all-optical format transparent time and wavelength demultiplexing technique for WDM & orthogonal-TDM Nyquist channels* in 2015 European Conference on Optical Communication (ECOC) (2015), 1–3.
157. Moodie, D., Ellis, A. & Ford, C. Generation of 6.3 ps optical pulses at a 10 GHz repetition rate using a packaged electroabsorption modulator and dispersion compensating fibre. *Electronics Letters* **30**, 1700–1701 (1994).
158. Hu, J., Brès, C.-S. & Huang, C.-B. Talbot effect on orbital angular momentum beams: azimuthal intensity repetition-rate multiplication. *Optics Letters* **43**, 4033–4036 (2018).
159. Hu, J., Fabbri, S. J., Huang, C.-B. & Brès, C.-S. Investigation of temporal Talbot operation in a conventional optical tapped delay line structure. *Optics express* **27**, 7922–7934 (2019).
160. Maram, R., Cortés, L. R. & Azaña, J. Programmable fiber-optics pulse repetition-rate multiplier. *Journal of Lightwave Technology* **34**, 448–455 (2016).
161. Hillerkuss, D. *et al.* Simple all-optical FFT scheme enabling Tbit/s real-time signal processing. *Optics express* **18**, 9324–9340 (2010).
162. Chuang, H.-P. & Huang, C.-B. Generation and delivery of 1-ps optical pulses with ultrahigh repetition-rates over 25-km single mode fiber by a spectral line-by-line pulse shaper. *Optics express* **18**, 24003–24011 (2010).
163. Marhic, M. E. Discrete Fourier transforms by single-mode star networks. *Optics letters* **12**, 63–65 (1987).
164. Dai, Y. & Yao, J. Nonuniformly-spaced photonic microwave delay-line filter. *Optics express* **16**, 4713–4718 (2008).
165. Götte, J. B. *et al.* Light beams with fractional orbital angular momentum and their vortex structure. *Optics express* **16**, 993–1006 (2008).
166. Paterson, L. *et al.* Controlled rotation of optically trapped microscopic particles. *Science* **292**, 912–914 (2001).

167. Leach, J. *et al.* Quantum correlations in optical angle–orbital angular momentum variables. *Science* **329**, 662–665 (2010).
168. Wang, J. *et al.* Terabit free-space data transmission employing orbital angular momentum multiplexing. *Nature photonics* **6**, 488–496 (2012).
169. Yan, L. *et al.* Q-plate enabled spectrally diverse orbital-angular-momentum conversion for stimulated emission depletion microscopy. *Optica* **2**, 900–903 (2015).
170. Pinnell, J., Rodríguez-Fajardo, V. & Forbes, A. Single-step shaping of the orbital angular momentum spectrum of light. *Optics express* **27**, 28009–28021 (2019).
171. Vaity, P. & Rusch, L. Perfect vortex beam: Fourier transformation of a Bessel beam. *Optics letters* **40**, 597–600 (2015).
172. Berkhout, G. C., Lavery, M. P., Courtial, J., Beijersbergen, M. W. & Padgett, M. J. Efficient sorting of orbital angular momentum states of light. *Physical review letters* **105**, 153601 (2010).
173. Hu, J. *et al.* Reconfigurable radiofrequency filters based on versatile soliton microcombs. *Nature communications* **11**, 1–9 (2020).
174. Marpaung, D. *et al.* Integrated microwave photonics. *Laser & Photonics Reviews* **7**, 506–538 (2013).
175. Sancho, J. *et al.* Integrable microwave filter based on a photonic crystal delay line. *Nature communications* **3**, 1–9 (2012).
176. Zhuang, L., Roeloffzen, C. G., Hoekman, M., Boller, K.-J. & Lowery, A. J. Programmable photonic signal processor chip for radiofrequency applications. *Optica* **2**, 854–859 (2015).
177. Eggleton, B. J., Poulton, C. G., Rakich, P. T., Steel, M. J. & Bahl, G. Brillouin integrated photonics. *Nature Photonics* **13**, 664–677 (2019).
178. Fandiño, J. S., Muñoz, P., Doménech, D. & Capmany, J. A monolithic integrated photonic microwave filter. *Nature Photonics* **11**, 124–129 (2017).
179. Ortigosa-Blanch, A., Mora, J., Capmany, J., Ortega, B. & Pastor, D. Tunable radio-frequency photonic filter based on an actively mode-locked fiber laser. *Optics letters* **31**, 709–711 (2006).
180. Maram, R., Onori, D., Azaña, J. & Chen, L. R. Discretely programmable microwave photonic filter based on temporal Talbot effects. *Optics express* **27**, 14381–14391 (2019).
181. Xue, X. *et al.* Microcomb-based true-time-delay network for microwave beamforming with arbitrary beam pattern control. *Journal of Lightwave Technology* **36**, 2312–2321 (2018).
182. Xu, X. *et al.* Broadband Photonic RF Channelizer With 92 Channels Based on a Soliton Crystal Microcomb. *Journal of Lightwave Technology* **38**, 5116–5121 (2020).
183. Tan, M. *et al.* Microwave and RF photonic fractional Hilbert transformer based on a 50 GHz Kerr micro-comb. *Journal of Lightwave Technology* **37**, 6097–6104 (2019).

## Bibliography

---

184. He, Y., Ling, J., Li, M. & Lin, Q. Perfect soliton crystals on demand. *Laser & Photonics Reviews* **14**, 1900339 (2020).
185. Haus, H. A. *Electromagnetic noise and quantum optical measurements* (Springer Science & Business Media, 2012).
186. Liu, J. *et al.* Photonic microwave generation in the X-and K-band using integrated soliton microcombs. *Nature Photonics*, 1–6 (2020).
187. Del’Haye, P., Arcizet, O., Gorodetsky, M. L., Holzwarth, R. & Kippenberg, T. J. Frequency comb assisted diode laser spectroscopy for measurement of microcavity dispersion. *Nature Photonics* **3**, 529 (2009).
188. Wang, Y. *et al.* Universal mechanism for the binding of temporal cavity solitons. *Optica* **4**, 855–863 (2017).
189. Cole, D. C., Lamb, E. S., Del’Haye, P., Diddams, S. A. & Papp, S. B. Soliton crystals in Kerr resonators. *Nature Photonics* **11**, 671–676 (2017).
190. Guo, H. *et al.* Universal dynamics and deterministic switching of dissipative Kerr solitons in optical microresonators. *Nature Physics* **13**, 94–102 (2017).
191. Liu, Y., Marpaung, D., Choudhary, A., Hotten, J. & Eggleton, B. J. Link performance optimization of chip-based Si<sub>3</sub>N<sub>4</sub> microwave photonic filters. *Journal of lightwave technology* **36**, 4361–4370 (2018).
192. Kim, H.-J., Leaird, D. E., Metcalf, A. J. & Weiner, A. M. Comb-based RF photonic filters based on interferometric configuration and balanced detection. *Journal of Lightwave Technology* **32**, 3478–3488 (2014).
193. Taheri, H., Matsko, A. B. & Maleki, L. Optical lattice trap for Kerr solitons. *The European Physical Journal D* **71**, 1–13 (2017).
194. Torres-Company, V., Leaird, D. E. & Weiner, A. M. Simultaneous broadband microwave downconversion and programmable complex filtering by optical frequency comb shaping. *Optics letters* **37**, 3993–3995 (2012).
195. Stern, B., Ji, X., Okawachi, Y., Gaeta, A. L. & Lipson, M. Battery-operated integrated frequency comb generator. *Nature* **562**, 401–405 (2018).
196. Shen, B. *et al.* Integrated turnkey soliton microcombs. *Nature* **582**, 365–369 (2020).
197. De Chatellus, H. G., Lacot, E., Glastre, W., Jacquin, O. & Hugon, O. Theory of Talbot lasers. *Physical Review A* **88**, 033828 (2013).

# Jianqi Hu

Email: [jianqi.hu@epfl.ch](mailto:jianqi.hu@epfl.ch)

Phone: +41-78-6367902

Address: ELB 135, PHOSL, EPFL,  
CH-1015, Lausanne, Switzerland

## EDUCATION

07. 2016 - Present	<b>Doctoral School of Photonics</b> , Doctoral Assistant École Polytechnique Fédérale de Lausanne (EPFL), Switzerland
09. 2012 - 06. 2016	<b>School of Optoelectronic Information</b> , Bachelor, 3.92/4 University of Electronic Science and Technology of China, China
02. 2014 - 06. 2014	<b>Department of Photonics</b> , Exchange Student, 4.3/4.3 National Chiao Tung University, Taiwan

## RESEARCH EXPERIENCES

07. 2016 - Present	<b>Photonic Systems Laboratory (PHOSL)</b> , Research Assistant Supervisor: Prof. Camille-Sophie Brès, EPFL, Switzerland <ul style="list-style-type: none"> <li>◇ Demonstrated second-harmonic and sum-frequency generation in SiN microresonators.</li> <li>◇ Demonstrated reconfigurable RF photonic filters based on soliton microcombs.</li> <li>◇ Proposed RODAM architecture for Nyquist OTDM systems.</li> <li>◇ Demonstrated temporal Talbot effect in an optical tapped delay line structure.</li> <li>◇ Generated optical Nyquist pulse for communications and RF photonics.</li> </ul>
10. 2017 - 02. 2018	<b>Ultrafast Plasmonics Lab</b> , Research Intern Supervisor: Prof. Chen-Bin Huang, National Tsing Hua University, Taiwan <ul style="list-style-type: none"> <li>◇ Demonstrated azimuthal Talbot effect based on superposition of OAM beams.</li> </ul>
02. 2016 - 05. 2016	<b>Rho's Research Lab</b> , Research Intern Supervisor: Prof. Junsuk Rho, Pohang University of Science and Technology, Korea <ul style="list-style-type: none"> <li>◇ Simulated metamaterials of negative refractive indices and hyperlens.</li> </ul>
05. 2015 - 07. 2015	<b>Photonics Technology Laboratory</b> , Research Intern Supervisor: Prof. Trevor J. Hall, University of Ottawa, Canada <ul style="list-style-type: none"> <li>◇ Tested silicon-based <math>2 \times 2</math>, <math>4 \times 4</math> MMI couplers using transposer.</li> </ul>

## TEACHING EXPERIENCES

Spring 2017 - 2019	EE440 Photonic Systems and Technology, EPFL <ul style="list-style-type: none"> <li>◇ Tutor of VPI simulation, semester project, and homework.</li> </ul>
-----------------------	---

## SOFTWARE SKILLS

Programming Softwares	Matlab, Python, LaTeX, C, LabVIEW, VHDL VPItransmissionMaker, OptiSystem, Lumerical FDTD, COMSOL Multiphysics, ISE, Multisim, LTSpice
--------------------------	--

## HONORS AND AWARDS

2020	SNF early postdoc mobility fellowship
2016	Outstanding graduates of Sichuan province
2015	Mitacs Globalink (Canada) & CSC (China) research travel fund
2015	Tang Lixin Scholarship, 1%
2014	National Scholarship, 1%
2014	Honorable Mention in the Mathematical Contest in Modeling
2013	First Prize in the Mathematical Contest of Sichuan Province
2013	National Scholarship, 1%

## LANGUAGES

Chinese (native), English (full proficiency)

---

## JOURNAL PUBLICATIONS

- [1] J. Hu<sup>†</sup>, J. He<sup>†</sup>, J. Liu, A. S. Raja, M. Karpov, A. Lukashchuk, T. J. Kippenberg, and C.-S. Brès, “Reconfigurable radiofrequency filters based on versatile soliton microcombs,” *Nature Communications*, **11**, 4377 (2020).
- [2] J. Hu, S. J. Fabbri, C.-B. Huang, and C.-S. Brès, “Investigation of temporal Talbot effect in a conventional optical tapped delay line structure,” *Optics Express*, **27**, 7922-7934 (2019).
- [3] J. Hu, C.-S. Brès, and C.-B. Huang, “Talbot effect on orbital angular momentum beams: azimuthal intensity repetition-rate multiplication,” *Optics Letters*, **43**, 4033-4036 (2018). [Top downloads of August 2018]
- [4] S. Xing, S. Kharitonov, J. Hu, and C.-S. Brès, “Linearly chirped mid-infrared supercontinuum in all-normal-dispersion chalcogenide photonic crystal fibers,” *Optics Express*, **26**, 19627-19636 (2018).
- [5] S. Xing, S. Kharitonov, J. Hu, and C.-S. Brès, “Fiber fuse in Chalcogenide photonic crystal fiber,” *Optics Letters*, **43**, 1443-1446 (2018).
- [6] M. Hasan, J. Hu, H. Nikkhah, and T. Hall, “A photonic circuit for complementary frequency shifting, in-phase quadrature/single sideband modulation and frequency multiplication: analysis and integration feasibility,” *Journal of Modern Optics*, **64**, 1386-1397 (2017).

## CONFERENCE PROCEEDINGS

- [1] J. Hu and C.-S. Brès, “Soliton Microcombs for RF photonic filters,” **ACP** (2020). [Invited]
- [2] J. Hu, J. He, J. Liu, A. S. Raja, M. Karpov, A. Lukashchuk, T. J. Kippenberg, and C.-S. Brès, “Two-soliton Microcombs Enabled Reconfigurable Microwave Photonic Filters,” **CLEO**, JTh2B.18 (2020).
- [3] J. Hu, J. He, A. S. Raja, J. Liu, T. J. Kippenberg, and C.-S. Brès, “Reconfigurable radiofrequency Photonic filters based on soliton microcombs,” **OFC**, M3H.2 (2020). [Top-scored]
- [4] J. Hu, S. Kharitonov, S. J. Fabbri, and C.-S. Brès, “Add-drop multiplexing architecture for Nyquist OTDM signals based on a single Mach-Zehnder modulator,” **ACP**, M4A.38 (2019).
- [5] J. Hu, S. J. Fabbri, C.-B. Huang, and C.-S. Brès, “Versatile Amplitude and Phase Filtering in an Optical Tapped Delay Line Structure,” **CLEO/EU**, ci\_5\_3 (2019).
- [6] S. Xing, S. Kharitonov, J. Hu, and C.-S. Brès, “Study of fiber fuse induced damage in chalcogenide photonic crystal fibers,” **ASSL**, ATh1A.4 (2018).
- [7] J. Hu, C.-S. Brès, and C.-B. Huang “Self-imaging of Azimuthal Intensity Petal Based on Orbital Angular Momentum Beams,” **FIO**, FM3C.2 (2018).
- [8] J. Hu, S. J. Fabbri, and C.-S. Brès, “Reconfigurable Filter-free Sinc-shaped RF Photonic Filters Based on Rectangular Optical Frequency Comb,” **CLEO**, SM1C.1 (2018).
- [9] J. Hu, S. J. Fabbri, and C.-S. Brès, “Flexible Width Nyquist Pulse Based on a Single Mach-Zehnder Modulator,” **CLEO**, SF3N.6 (2018).
- [10] S. Xing, S. Kharitonov, J. Hu, and C.-S. Brès, “Fiber fuse in GeAsSe photonic crystal fiber and its impact on undamaged segment,” **CLEO**, JTh2A.93 (2018).
- [11] S. Xing, S. Kharitonov, J. Hu, D. Grassani, and C.-S. Brès, “MIR supercontinuum in all-normal dispersion Chalcogenide photonic crystal fibers pumped with 2  $\mu\text{m}$  femtosecond laser,” **ASSL**, ATu5A.3 (2017).
- [12] S. Xing, S. Kharitonov, J. Hu, D. Grassani and C.-S. Brès, “Stable 2.1  $\mu\text{m}$  near 100% polarized Ho-doped all-fiber laser based on a polarizer-free cavity scheme,” **ECOC**, M.2.B.3 (2017).
- [13] J. Hu, S. J. Fabbri, and C.-S. Brès, “Optical Sinc-shaped Nyquist pulse source based on a single Mach-Zehnder modulator,” **ICTON**, Tu.D5.5 (2017).